9

Interactions of Polarized Photons with Matter

9.1 Overview

This chapter discusses theoretical concepts underlying the description of the interactions of polarized photons with matter. Because of the long history of the subject in the optical wavelength regime we start with a brief summary of terminology associated with polarization dependent scattering and absorption effects of visible light in matter. This will allow us to clearly define a modern terminology that is most suitable for X-rays.

We start our theoretical treatment with *semiclassical concepts* (i.e., classical concepts with the addition of some quantum concepts) that conveniently build on those developed in Chap. 8. For example, the transmission of polarized photons through magnetic materials, the magneto-optical Faraday effect, can be understood semiclassically by assuming that polarized light is composed of right and left circular polarized components and that one circular component is preferentially phase shifted or absorbed upon transmission through a magnetic material. This explains the change in polarization state of the transmitted wave. Similarly, nonresonant scattering processes are readily understandable as a two step process where the EM wave jiggles the charge or the spin and the motion leads to re-radiation, i.e., scattering, of an EM wave.

Such semiclassical or phenomenological treatments, however, are unsatisfactory if one wants to understand the interaction of the EM wave with the material in detail or even quantitatively link measured intensities with magnetic parameters such as magnetic moments. A key problem with semiclassical treatments is that the processes with the largest cross-section, X-ray absorption or resonant scattering, are true quantum phenomena. This has historically been partially overcome by combining classical elements with the quantum mechanical concept of *oscillator strength* of an electronic transition. In analogy to the harmonic oscillator, a connection can then be established of *resonant scattering* and X-ray absorption intensities or cross-sections and such a treatment leads to the famous Kramers–Kronig relations [109,178,190,362].

However, the Kramers–Kronig relations only allow one to connect an experimental absorption spectrum with the scattered intensity or vice versa but it does not provide a means to calculate either the absorption or scattered intensity from first principles. Such a *quantitative* treatment requires the operator and matrix element approach of modern quantum mechanics in conjunction with time-dependent perturbation theory. Only this approach allows the quantitative analysis of resonant X-ray scattering and X-ray absorption intensities in terms of atomic quantities such as magnetic moments and their anisotropies. For this reason we shall present the basic concepts of this approach.

In comparison to optical dichroism measurements, X-rays offer significant advantages. Because excitations are localized on atoms, X-rays offer specificity to individual elements and their chemical state. In contrast to the optical range, X-ray transition intensities represent an average over all valence states in the Brillouin zone, the same average that determines physical quantities like the valence shell occupation number and the spin and orbital magnetic moments. By use of powerful sum rules the spin and orbital moments can be separated and can be quantitatively determined from integrated peak intensities. Also, because of the short wavelength of X-rays, they offer higher spatial resolution, down to the size of the X-ray wavelength. In the era of nanoscience this provides another significant advantage over optical methods which are typically limited to a spatial resolution above 200 nm.

9.2 Terminology of Polarization Dependent Effects

In the past, optical effects were mainly described phenomenologically by means of a *refractive index*. In general, this index is dependent on the frequency and the polarization of the EM wave. For a given sample, the frequency dependence is particularly important around specific resonant frequencies and near such resonances the refractive index needs to be described as a complex dimensionless quantity according to [109, 149][1]

$$n(\omega) = 1 - \delta(\omega) + \mathrm{i}\,\beta(\omega)\ . \tag{9.1}$$

The real part $\delta(\omega)$ is associated with refraction and the imaginary part $\beta(\omega)$ with absorption of the EM wave in the medium.

The polarization dependence of the refractive index is called "birefringence" and one distinguishes linear and circular birefringence, depending on the polarization of the incident light. The term *refringence* was originally used instead of the term *refraction*, both deriving from the Latin word *frangere*, meaning to break. The polarization dependence of the absorptive part $\beta(\omega)$ is referred to as "dichroism." The term has its origin in the fact that certain crystals may appear dichroic or in two different colors when white light is

[1] For isotropic media we have the general relationship $n \equiv \sqrt{\epsilon\mu/\epsilon_0\mu_0}$, where ϵ/ϵ_0 is the dielectric constant and μ/μ_0 the relative permeability.

incident along two different directions. This is due to the preferential absorption of polarization components and frequencies along different directions. We may summarize these and other optical effects as follows.

- *Birefringence*. The existence of two different indices of refraction for polarized incident light. One distinguishes linear birefringence and circular birefringence.
- *Dichroism*. The dependence of photon absorption on polarization. There are four main types. Linear dichroism and (natural) circular dichroism depend on the charge distribution. Magnetic linear dichroism and magnetic circular dichroism depend on the spin and charge distribution.
- *Optical activity or rotation*. The rotation of the linear polarization direction by a nonmagnetic sample. Optical activity is typically associated with a handedness of the charge distribution in space, i.e., chirality.
- *Magneto-optical rotation*. The rotation of the linear polarization direction by a magnetic sample. It arises from the presence of aligned magnetic moments, which give the sample a handedness in time through breaking of time-reversal symmetry.

In modern theory, based on time-dependent perturbation theory and the quantum mechanical operator and matrix element method, all interaction effects of polarized photons with matter listed earlier can be cast in terms of a scattering problem. The final formalism has a close resemblance with the classical approach based on the refractive index in that the scattering is expressed in terms of a *complex atomic scattering factor*

$$F(\boldsymbol{Q},\omega) = F^0(\boldsymbol{Q}) + F'(\omega) - \mathrm{i}\,F''(\omega). \tag{9.2}$$

Here $\boldsymbol{Q}$ is the momentum transfer in the scattering process and $F^0(\boldsymbol{Q})$ is the *atomic form factor*. All factors $F^0(\boldsymbol{Q})$, $F'(\omega)$, and $F''(\omega)$, are real numbers in units of number of electrons per atom. In the soft X-ray range or for scattering in the forward direction, where the momentum transfer $\boldsymbol{Q}$ is small, we obtain an expression similar to (9.1),

$$F(\omega) = Z + F'(\omega) - \mathrm{i}\,F''(\omega) = f_1(\omega) - \mathrm{i}f_2(\omega). \tag{9.3}$$

Here Z is the number of electrons per atom and the anomalous scattering factors $F'(\omega)$ and $F''(\omega)$ can be calculated from first principles and represent the refractive and absorptive contributions to scattering. In practice, in the soft X-ray region one can conveniently use the web-tabulated *Henke–Gullikson factors* [362,363].

The *Henke–Gullikson* atomic factors are defined as

$$f_1(\omega) = Z + F'(\omega), \qquad f_2(\omega) = F''(\omega)\ . \tag{9.4}$$

They have units of [number of electrons per atom].

It is important to realize that f_1 and f_2 are *atomic* factors that do not include bonding effects associated with atoms in different environments. Fortunately, bonding effects only change the X-ray interactions near absorption edges. In the near edge region the X-ray excitations are associated with specific transitions from core states to empty valence states of the material and the fine structure of the resonances is therefore characteristic of the local bonding environment of the absorbing atom. Outside the near-edge resonance region, the photoelectron is directly excited into free-electron-like continuum states and the excitation cross-section is atom specific and varies smoothly with energy. The X-ray response of the material in this region is therefore simply a superposition of all the individual atomic responses given by the Henke–Gullikson factors. In practice, one rarely measures X-ray absorption or scattering spectra on an absolute intensity or cross-section scale. If needed one converts the measured spectra, including the near-edge resonance region, to an absolute scale by fitting them *outside the resonance region* to the cross-sections calculated by means of the Henke–Gullikson factors, as discussed in Sect. 10.3.3.

The real *atomic scattering factors* $F^0(\boldsymbol{Q})$, $F'(\omega)$, $F''(\omega)$, $f_1(\omega)$, and $f_2(\omega)$ have units of [number of electrons/atom].

The relationship between $n(\omega)$ in (9.1) and $F(\omega)$ in (9.3) is given by [364]

$$1 - n(\omega) = \frac{r_0 \lambda^2}{2\pi} \sum_j \rho_j \, F_j(\omega), \tag{9.5}$$

where $r_0 = e^2/4\pi\epsilon_0 m_e c^2 = 2.818 \times 10^{-15}$ m/electron is the classical electron radius, λ is the wavelength, and ρ_j is the number density of atomic species j (atoms/length^3), so that the right hand side of (9.5) is dimensionless, as required. Restricting ourselves to a sample with only one atomic species with density ρ_a we obtain the simple relations

$$\delta(\omega) = \frac{r_0 \lambda^2}{2\pi} \rho_\mathrm{a} \, f_1(\omega), \tag{9.6}$$

$$\beta(\omega) = \frac{r_0 \lambda^2}{2\pi} \rho_\mathrm{a} \, f_2(\omega). \tag{9.7}$$

$\delta(\omega)$ and $\beta(\omega)$ are dimensionless.

Scattering and reflectivity experiments depend on both the real, $f_1(\omega) = Z + F'(\omega)$, and imaginary, $f_2(\omega) = F''(\omega)$, parts. In practice, the two scattering factors $F'(\omega)$ and $F''(\omega)$ are rarely determined independently but one is obtained from the other by a Kramers–Kronig transformation, discussed

in Sect. 9.4.4. In particular, $F''(\omega)$ is typically obtained by an *X-ray absorption* measurement since it is directly proportional to the X-ray absorption cross-section. Experimentally, the real part $F'(\omega)$, is best determined from a measurement of the *polarization rotation* using linearly polarized incident radiation.[2]

All polarization dependent effects caused by the interaction of an EM wave with matter discussed earlier can therefore be completely described in terms of the scattering factors. The task then boils down to determining the scattering factors in the resonance region where they contain information on the electronic and magnetic structure of the material. There are two important types of measurements to determine them.

- Polarization dependent *X-ray absorption* measurements completely determine $F''(\omega)$. This is an absolute intensity measurement[3] only the incident polarization needs to be known.
- *Polarization rotation* measurements completely determine $F'(\omega)$. This is an intensity difference measurement involving the polarizations of the incident and transmitted radiation.

9.3 SemiClassical Treatment of X-ray Scattering by Charges and Spins

9.3.1 Scattering by a Single Electron

The semiclassical treatment of magnetic dichroism starts with *nonresonant X-ray scattering* by the charge and spin of a *single electron* and it provides an intuitive understanding of the processes involved. Below we will review the processes of charge and spin scattering by an electromagnetic wave. While we will give the complete equations for charge scattering, we shall only discuss the spin scattering channel that is of pure spin origin. Other channels arising from the spin–orbit coupling or from the fact that charge and spin are both tied to an electron and that charge motion naturally leads to spin motion will not be considered here [190].

We assume an EM wave with unit polarization vector $\boldsymbol{\epsilon}$ and fields

$$\boldsymbol{E}(\boldsymbol{r},t) = \boldsymbol{\epsilon}\, E_0\, \mathrm{e}^{-\mathrm{i}(\omega t - \boldsymbol{k}\cdot\boldsymbol{r})}, \tag{9.8}$$

[2]The rotation angle which is related to $F'(\omega)$ and δ is determined from a relative transmission measurement as a function of polarizer orientation. The ellipticity of the transmitted polarization, which is related to $F''(\omega)$ and β can also be determined by means of polarimetry, yet absorption measurements are easier and more accurate.

[3]In practice, one often normalizes measured data to the Henke–Gullikson data [362, 363] outside the resonance regions and therefore one performs only a relative intensity measurement.

$$\boldsymbol{B}(\boldsymbol{r},t)=\frac{1}{c}(\boldsymbol{k}_0\times\boldsymbol{\epsilon})E_0\,\mathrm{e}^{-\mathrm{i}(\omega t-\boldsymbol{k}\cdot\boldsymbol{r})}. \tag{9.9}$$

Following convention we have chosen $\boldsymbol{\epsilon}$ to be along the $\boldsymbol{E}$-vector and we shall for simplicity assume linear polarization. When this wave is incident on a free electron of charge $-e$ and spin $\boldsymbol{s}$, both the charge and the spin are set in motion. The electron motion follows the oscillating electric field, creating an electric dipole moment directed along the $\boldsymbol{E}$-vector

$$\boldsymbol{p}(t)=-\frac{e^2}{m_\mathrm{e}\omega^2}\;\boldsymbol{E}_0\;\mathrm{e}^{-\mathrm{i}\omega t}. \tag{9.10}$$

For spin scattering we consider how the magnetic field acts on the spin. We know from Chapt. 3 that the spin precesses around a constant magnetic field according to the torque equation $\boldsymbol{T}=\hbar\mathrm{d}\boldsymbol{s}(t)/\mathrm{d}t$,

$$\frac{\mathrm{d}\boldsymbol{s}(t)}{\mathrm{d}t}=-\frac{e}{m_\mathrm{e}}\;\boldsymbol{s}(t)\times\boldsymbol{B}\;, \tag{9.11}$$

For a linearly polarized EM wave the magnetic field $\boldsymbol{B}(t)=\boldsymbol{B}_0\mathrm{e}^{-\mathrm{i}\omega t}$ oscillates along an axis in space and changes sign periodically. According to (9.11) a sign change in $\boldsymbol{B}(t)$ leads to a sign change of the torque $\boldsymbol{T}=\hbar\mathrm{d}\boldsymbol{s}(t)/\mathrm{d}t$ direction and thus the vector $\boldsymbol{s}$ rapidly precesses back-and-forth on a cone around the axis of $\boldsymbol{B}(t)$, as shown in Fig. 9.1. The component $\boldsymbol{s}_0$ is approximately constant while the small perpendicular component $\boldsymbol{s}_\mathrm{d}$ oscillates with the frequency of the EM wave and represents a magnetic dipole. With $\boldsymbol{m}=-2\mu_\mathrm{B}\boldsymbol{s}_\mathrm{d}$ and $\mu_\mathrm{B}=e\hbar\mu_0/2m_\mathrm{e}$ we obtain for the oscillating magnetic dipole moment

$$\boldsymbol{m}(t)=\mathrm{i}\;\frac{e^2\hbar\mu_0}{\omega m_\mathrm{e}^2}\boldsymbol{s}\times\boldsymbol{B}_0\;\mathrm{e}^{-\mathrm{i}\omega t}, \tag{9.12}$$

where $\boldsymbol{s}\sim\boldsymbol{s}_0$ is the initial spin direction. Whereas the electric dipole oscillates in the direction of $\boldsymbol{E}$, the magnetic dipole oscillates in a direction that is perpendicular to $\boldsymbol{B}$ and $\boldsymbol{s}$. This leads to different polarization effects in the scattering as discussed later.

We have now derived the electric and magnetic dipole moments induced by interaction of a polarized EM wave with the charge and spin of an electron. This is the first step in the X-ray scattering process. The second step is simply re-radiation of EM waves by the oscillating electric and magnetic dipoles. The scattered radiation is determined by the dipolar fields in the spatial region far from the dipole which have a rather simple spherical wave form $\mathrm{e}^{\mathrm{i}k'r}/r$ given by Jackson [149]. For convenience we only list the scattered electric fields denoted $\boldsymbol{E}'(t)$ since the magnetic field can be simply obtained from (5.9). The fields radiated by an electric dipole $\boldsymbol{p}(t)$ are

$$\boldsymbol{E}'(t)=\frac{\omega^2}{4\pi\epsilon_0c^2}\;\frac{\mathrm{e}^{\mathrm{i}k'r}}{r}\;[\boldsymbol{k}'_0\times\boldsymbol{p}(t)]\times\boldsymbol{k}'_0 \tag{9.13}$$

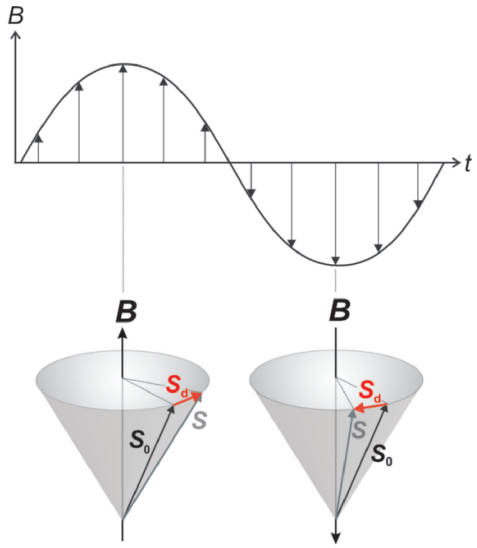

Fig. 9.1. Precessional motion of a spin in the magnetic field $\boldsymbol{B}(t)$ of a linearly polarized EM wave. When the oscillating field changes direction so does the precession direction of $\boldsymbol{s}$. If we write $\boldsymbol{s} = \boldsymbol{s}_0 + \boldsymbol{s}_\mathrm{d}$ the perpendicular component $\boldsymbol{s}_\mathrm{d}$ changes sign periodically and therefore represents an oscillating magnetic dipole

and those radiated by a magnetic dipole $\boldsymbol{m}(t)$ are

$$\boldsymbol{E}'(t) = -\frac{\omega^2}{4\pi c}\,\frac{\mathrm{e}^{\mathrm{i}k'r}}{r}\,[\boldsymbol{k}'_0 \times \boldsymbol{m}(t)]. \tag{9.14}$$

It is now simple to derive the scattered field for charge scattering by combining (9.10) and (9.13) and we obtain

$$\boldsymbol{E}'(t) = -\frac{1}{4\pi\epsilon_0}\,\frac{e^2}{m_\mathrm{e}c^2}\,\frac{\mathrm{e}^{\mathrm{i}k'r}}{r}\,[\boldsymbol{k}'_0 \times \boldsymbol{E}(t)] \times \boldsymbol{k}'_0. \tag{9.15}$$

Similarly we can combine (9.12) and (9.14) to obtain the spin scattering amplitude, remembering that $c^2 = 1/\epsilon_0\mu_0$,

$$\boldsymbol{E}'(t) = \mathrm{i}\frac{1}{4\pi\epsilon_0}\,\frac{e^2}{m_\mathrm{e}c^2}\,\frac{\hbar\omega}{m_\mathrm{e}c^2}\,\frac{\mathrm{e}^{\mathrm{i}k'r}}{r}\,[\boldsymbol{s} \times (\boldsymbol{k}_0 \times \boldsymbol{E}(t))] \times \boldsymbol{k}'_0. \tag{9.16}$$

The two scattering processes are illustrated in Fig. 9.2. Together with the above equations it clearly shows the dipolar nature of the electric and magnetic scattering processes.

There are important differences in the polarization, phase, and amplitude of charge and spin scattering. We note the following important points:

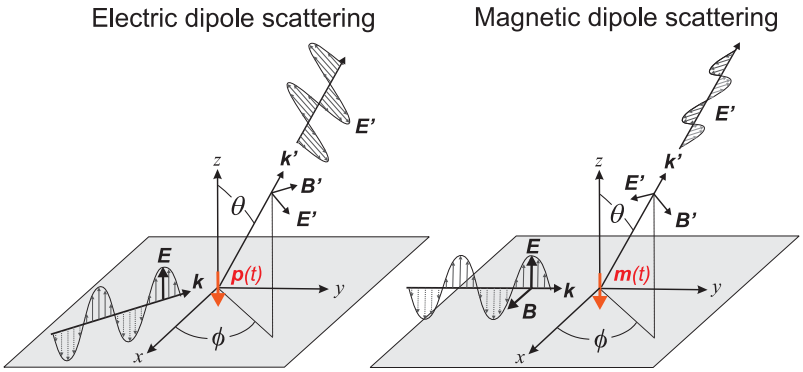

Fig. 9.2. Mechanisms of X-ray dipole scattering from a charge and a spin. Note that charge scattering preserves the polarization direction while spin scattering rotates it

- Charge scattering causes a phase shift of π (minus sign in (9.15)) between the incident and scattered fields.
- Spin scattering introduces a phase shift of $\pi/2$ (factor i in (9.16)) between the incident and scattered fields.
- The spin scattering amplitude is reduced by a factor of $\hbar\omega/m_\mathrm{e}c^2$ relative to the charge scattering amplitude, where $m_\mathrm{e}c^2 = 511\,\mathrm{keV}$.
- Charge scattering conserves the polarization while spin scattering causes a rotation of the polarization.

We now touch base with conventional scattering theory by defining the scattering factor of a *single electron*. We assume that by a suitable analyzer we can determine the scattered amplitude and polarization direction $\boldsymbol{\epsilon}'$, which by geometry is perpendicular to the scattered wave vector $\boldsymbol{k}'_0$. This allows us to define the polarization dependent *scattering length*

$$f(\boldsymbol{\epsilon}, \boldsymbol{\epsilon}') = -\frac{r\mathrm{e}^{-\mathrm{i}k'r}}{E}\ \boldsymbol{E}' \cdot \boldsymbol{\epsilon}' \tag{9.17}$$

It is in general a complex quantity with the dimension of [length].[4]

By use of (9.15) we obtain the electric dipole scattering length for a single electron,

$$f_\mathrm{e}(\boldsymbol{\epsilon}, \boldsymbol{\epsilon}') = \frac{1}{4\pi\epsilon_0}\ \frac{e^2}{m_\mathrm{e}c^2}\ \boldsymbol{\epsilon} \cdot \boldsymbol{\epsilon}' = r_0\ \boldsymbol{\epsilon} \cdot \boldsymbol{\epsilon}'. \tag{9.18}$$

[4] In general, (9.17) should be written using the complex conjugate vector $\boldsymbol{\epsilon}'^*$ to account for imaginary polarization vectors as are used for circularly polarized X-rays.

where $r_0 = e^2/4\pi\epsilon_0 m_e c^2 = 2.82 \times 10^{-6}\,\mathrm{nm}$ is called the *classical electron radius* or the *Thomson scattering length*. We shall see later that the area r_0^2, apart from a geometrical factor, gives the X-ray scattering cross-section of a single electron. It is therefore a very important reference number for describing the scattering amplitude of all multielectron systems. For magnetic dipole scattering we obtain from (9.16)

$$f_s(\boldsymbol{\epsilon}, \boldsymbol{\epsilon}') = -\mathrm{i}\; r_0\; \frac{\hbar\omega}{m_e c^2}\; \boldsymbol{s} \cdot (\boldsymbol{k}_0 \times \boldsymbol{\epsilon}) \times (\boldsymbol{k}_0' \times \boldsymbol{\epsilon}'). \tag{9.19}$$

We have conveniently defined the scattering length so that its square is proportional to the intensity scattered into a solid angle Ω, i.e., the *differential scattering cross-section* with dimension [length^2/solid angle], given by

$$\boxed{\frac{\mathrm{d}\sigma}{\mathrm{d}\Omega} = |f(\boldsymbol{\epsilon}, \boldsymbol{\epsilon}')|^2}\,. \tag{9.20}$$

Note that by squaring the scattering factor the important phase information that was contained in the complex form of $\boldsymbol{E}'$ is lost. This gives rise to the famous phase problem in X-ray crystallography.

The total scattering cross-section for a single electron is then simply obtained by angular integration of the polarization dependent squared scattering factor. The integration of the polarization factor $\boldsymbol{\epsilon} \cdot \boldsymbol{\epsilon}'$ gives a factor of $8\pi/3$ and we obtain for the charge

$$\sigma_e = \int |f(\boldsymbol{\epsilon}, \boldsymbol{\epsilon}')|^2 \mathrm{d}\Omega = r_0^2 \int_0^{2\pi} \int_0^{\pi} \sin^2\theta\; \sin\theta\; \mathrm{d}\theta\; \mathrm{d}\phi = \frac{8\pi}{3}\; r_0^2, \tag{9.21}$$

which is called the *Thomson cross-section* and has the dimension [length^2].

The Thomson cross-section

$$\sigma_e = \frac{8\pi}{3}\; r_0^2 = 0.665 \times 10^{-28}\,\mathrm{m}^2 = 0.665\,\mathrm{barn} \tag{9.22}$$

is the total scattering cross-section from the charge of a single electron. Cross-sections are typically listed in units of barn, where $1\,\mathrm{b} = 10^{-28}\,\mathrm{m}^2$. Hence one can conveniently remember that the X-ray scattering cross-section for a single electron is about 1 b.

The spin cross-section is obtained by angular integration of (9.19) as

$$\sigma_s = \frac{8\pi}{3}\; \frac{1}{4} \left(\frac{\hbar\omega}{m_e c^2}\right)^2\; r_0^2 = \frac{\sigma_e}{4} \left(\frac{\hbar\omega}{m_e c^2}\right)^2. \tag{9.23}$$

Equations (9.21) and (9.23) clearly show that for typical X-ray energies charge scattering is stronger by orders of magnitude than spin scattering. For example, assuming a photon energy of 10 keV, the factor $(\hbar\omega/m_e c^2)^2 = (10/511)^2$

is about 4×10^{-4} and the weak spin scattering signal will only be observable in very special circumstances. An example is an antiferromagnetic lattice where the spin structure has a different periodicity than the charge structure and weak magnetic scattering peaks exist at locations in reciprocal space where charge scattering peaks are absent [365]. When the photon energy $\hbar\omega$ is equal to twice the rest energy of the electron, i.e., $\hbar\omega = 2m_\mathrm{e}c^2 = 1.022\,\mathrm{MeV}$, we see that magnetic and charge scattering have the same cross-section.

9.3.2 Scattering by an Atom

It is straightforward to extend the scattering formalism for a single electron to that for a multielectron atom. We simply assume that the total scattered amplitude is the sum of the amplitudes of the individual electrons. However, depending on which electron in the atom the X-ray wave scatters, there will be a tiny length difference in the path of the incident X-ray wave to the detector. Although the path length differences will be of the order of the size of the atom, so is the wavelength of the X-rays. Therefore the small path lengths differences can affect the scattered amplitude through interference effects. This effect is taken into account by the so-called *atomic form factor*

$$\boxed{F^0(\boldsymbol{Q}) = -\frac{1}{e}\int \rho(r)\,\mathrm{e}^{\mathrm{i}\boldsymbol{Q}\cdot\boldsymbol{r}}\mathrm{d}r} \tag{9.24}$$

which makes the scattering process angle dependent, expressed by a wavevector or momentum transfer $\boldsymbol{Q} = \boldsymbol{k} - \boldsymbol{k}'$ in the scattering process. The atomic form factor $F^0(\boldsymbol{Q})$ is the Fourier transform of the number density of electrons in the atomic volume, and it is a real number.

The total charge scattering amplitude or scattering length of the atom is then given by the Thomson scattering length r_0 times the atom-specific form factor times the polarization factor of (9.18), and we obtain for the nonresonant *atomic scattering length*

$$f_\mathrm{atom} = f^0(\boldsymbol{Q}) = r_0\,(\boldsymbol{\epsilon}\cdot\boldsymbol{\epsilon}')\,F^0(\boldsymbol{Q})\ . \tag{9.25}$$

By use of (9.20) this can be written as a differential scattering cross-section and we have our final result.

The *nonresonant differential atomic scattering cross-section* can be expressed by means of the *real atomic form factor* $F^0(\boldsymbol{Q})$ with units of number of electrons per atom and a polarization dependent term as a multiple of the scattering cross-section of a single electron $\sigma_\mathrm{e} = 8\pi r_0^2/3$ according to

$$\left(\frac{\mathrm{d}\sigma}{\mathrm{d}\Omega}\right)_\mathrm{atom} = r_0^2\,|\boldsymbol{\epsilon}\cdot\boldsymbol{\epsilon}'|^2\,|F^0(\boldsymbol{Q})|^2 = \frac{3}{8\pi}\,\sigma_\mathrm{e}\,|\boldsymbol{\epsilon}\cdot\boldsymbol{\epsilon}'|^2\,|F^0(\boldsymbol{Q})|^2. \tag{9.26}$$

For $Q \to \infty$, i.e., when the wavelength λ becomes small relative to the atomic size or when the path difference L becomes large, the waves scattered from different parts of the atom interfere destructively and cause the form factor to vanish, $F^0(\boldsymbol{Q}) = 0$. In the opposite limit, $Q = 0$, i.e., forward scattering or when the wavelength λ becomes large relative to the atomic size, there is no path length difference and different volume elements scatter in phase. Thus in the soft X-ray region where λ is of the order of 1 nm, the form factor becomes equal to the number of electrons, $f^0(\boldsymbol{Q}) = Z$.

9.4 SemiClassical Treatment of Resonant Interactions

So far we have not considered the different binding energies of the atomic electrons, i.e., the shell structure of the atom. In a simple model the massive positively charged nucleus $(+Ze)$ is surrounded by core and valence electrons that have distinct binding energies. It is clear that some kind of "resonance effects" will arise when the X-ray energy is close or equal to these characteristic energies. A proper description of these effects requires quantum theory. In a quantum mechanical one-electron picture the incident photon excites a core electron in an atom to a higher lying empty state. This is the X-ray absorption step. When the electron decays back into the core shell by emission of a photon of the same energy we speak of resonant X-ray scattering, more precisely *elastic* resonant X-ray scattering. This simple picture shows that X-ray absorption and resonant X-ray scattering have a lot of physics in common and we shall connect the two now.

While the proper description and link of these processes indeed requires a quantum theoretical treatment, historically, it was first treated semiclassically. The semiclassical formalism cannot be used to calculate X-ray absorption or resonant scattering cross-sections, but it clearly reveals the link of absorption and scattering. The most important link comes from the so-called Kramers–Kronig formalism. It allows measured absorption cross-sections to be converted to scattering cross-sections and vice versa. Let us take a look at how this comes about.

9.4.1 X-ray Absorption

The importance of X-ray absorption is evident from Röntgen's first experiments, as revealed by the image in Fig. 1.14, showing the preferential absorption in bone over that in tissue. Empirically it was soon found that when X-rays traverse matter the X-ray intensity, given by (5.17) as $I = \epsilon_0 c|\boldsymbol{E}|^2$, decays exponentially. This fact is easily derived if we assume that each substance has a characteristic length λ_x which leads to an intensity attenuation by a factor $1/e$. The quantity $\mu_x = 1/\lambda_x$ with the dimension of [length^{-1}] is called the *linear X-ray absorption coefficient*. Using the geometry of Fig. 9.3 we see that the beam is attenuated by the amount $\mu_x \mathrm{d}z$ as it traverses the thin

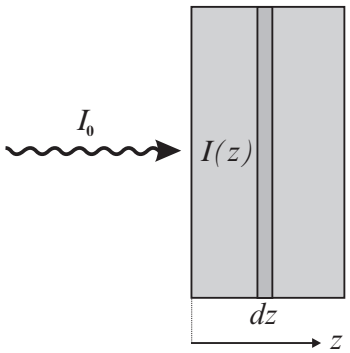

Fig. 9.3. Schematic for the derivation of the absorption law given by (9.28)

sheet of thickness $\mathrm{d}z$ at a depth z from the surface. This gives the following condition for the intensity

$$-\mathrm{d}I(z) = I(z)\,\mu_x\,\mathrm{d}z\ . \tag{9.27}$$

The differential equation $\mathrm{d}I(z)/\mathrm{d}z = -\mu_x\,I(z)$ has the solution $I(z) = A\,\mathrm{e}^{-\mu_x z}$ and by choosing $A = I_0$ as the incident intensity at the point $z = 0$ we have our final result.

The *X-ray absorption intensity* is attenuated upon transmission through a sample with linear absorption coefficient μ_x, according to

$$I(z) = I_0\,\mathrm{e}^{-\mu_x z}. \tag{9.28}$$

The *X-ray absorption cross-section* σ^{abs} is defined as the number of photons absorbed per atom divided by the number of incident photons per unit area and hence has the dimension [length^2/atom]. The number of photons absorbed in the thin sheet $\mathrm{d}z$ is $I(z)\mu_x\mathrm{d}z$ according to (9.27) and the number incident on the thin sheet per unit area is $I(z)\rho_{\mathrm{a}}\mathrm{d}z$, where ρ_{a} [atoms/volume] is the atomic number density. We have

$$\boxed{\mu_x = \rho_{\mathrm{a}}\,\sigma^{\mathrm{abs}} = \frac{N_{\mathrm{A}}}{A}\,\rho_{\mathrm{m}}\,\sigma^{\mathrm{abs}}} \tag{9.29}$$

where ρ_{m} [mass/volume] is the atomic mass density, $N_{\mathrm{A}} = 6.02214 \times 10^{23}$ [atoms/mol] is Avogadro's number, and A [mass/mol] is the atomic mass number. The quantities ρ_{m}, A, and ρ_{a} for the $3d$ transition metals Fe, Co, Ni are given in Table 10.1.

The *linear X-ray absorption coefficient* $\mu_x = 1/\lambda_x$ has the dimension [length^{-1}], while the *X-ray absorption cross-section* σ^{abs} has the dimension [length^2/atom].

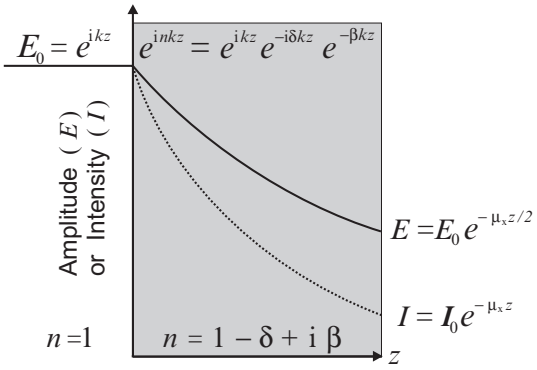

Fig. 9.4. Decay of the amplitude E and intensity $I \propto |E|^2$ of an incident wave $E_0 = \mathrm{e}^{\mathrm{i}kz}$ during transmission through a homogeneous sample with refractive index $n = 1 - \delta + \mathrm{i}\beta$ and linear X-ray absorption coefficient μ_x. In the text we show that $\beta = \mu_x/2k$

Let us now take a look what happens as an EM wave enters into a medium described by a refractive index $n = 1-\delta+\mathrm{i}\beta$ and a linear absorption coefficient μ_x. We assume that the wave is normally incident from vacuum ($n = 1$) onto the sample along the z direction as shown in Fig. 9.4. For convenience we normalize the amplitude of the incident wave to 1 and ignore the temporal dependence, so that $E_0 = \mathrm{e}^{\mathrm{i}kz}$.

Inside the sample the electric field is then given by

$$E = \mathrm{e}^{\mathrm{i}nkz} = \underbrace{\mathrm{e}^{\mathrm{i}kz}}_{E_0} \underbrace{\mathrm{e}^{-\mathrm{i}\delta kz}}_{\text{phase shift}} \underbrace{\mathrm{e}^{-\beta kz}}_{\text{absorption}} \tag{9.30}$$

and we clearly see the complex refractive contribution $\mathrm{e}^{-\mathrm{i}\delta kz}$ leading to a phase shift δkz and the real absorptive contribution which reduces the incident amplitude E_0 by a factor $\mathrm{e}^{-\beta kz}$. By comparing the intensity attenuation law (9.28) with the attenuation law that follows from squaring (9.30), i.e.,

$$|E|^2 = |E_0|^2 \, \mathrm{e}^{-2\beta kz} \ , \tag{9.31}$$

we obtain

$$\beta = \frac{\mu_x}{2k} = \frac{\rho_\mathrm{a}}{2k} \, \sigma^\mathrm{abs}. \tag{9.32}$$

This shows the direct relationship between the X-ray absorption cross-section and β. By use of (9.7) and $k = 2\pi/\lambda$, where λ is the X-ray wavelength, we can state as follows.

The *X-ray absorption cross-section* is related to the imaginary part of the refractive index β and the Henke – Gullikson scattering factor f_2 according to

$$\sigma^{\mathrm{abs}} = \frac{4\pi}{\lambda\rho_{\mathrm{a}}}\,\beta = 2r_0\lambda\, f_2\ . \tag{9.33}$$

It is important to state the implicit assumption that went into deriving (9.33). In general, the scattering factor given by (9.2) depends on the scattering direction or $\boldsymbol{Q}$. In (9.33) we implicitly assume that $F'' = f_2$ is independent of $\boldsymbol{Q}$. This is usually a good assumption in the X-ray region where absorption and resonant scattering are due to electronic excitations of core electrons. Because of the small core shell radius the path length difference experienced by a wave that is scattered anywhere within the core volume, will be small. Therefore the angular or $\boldsymbol{Q}$ dependence will be weak for core shell scattering. More generally, the $\boldsymbol{Q}$ dependence can be neglected when the wavelength is large relative to the atomic size since then $|\boldsymbol{Q}| \sim 2\pi/\lambda \to 0$. The latter condition is well satisfied in the soft X-ray region with wavelengths in excess of 1 nm.

9.4.2 Resonant Scattering

In the introduction to this section we have given the quantum mechanical picture of resonant scattering, consisting of resonant absorption and emission of a photon. Such a resonant process is semiclassically treated by representing a multielectron atom as a collection of harmonic oscillators. Each oscillator corresponds to a particular quantum mechanical resonant excitation–deexcitation process of a core shell with binding energy E_n. Each atom has then a set of resonance frequencies or energies $E_n = \hbar\omega_n$ and also characteristic damping constants Γ_n. The damping constants describe the dissipation of energy from the applied field and they have the dimension of frequency with $\Gamma_n \ll \omega_n$. The presence of the damping term indicates that the resonating atom can absorb energy from the EM wave and we shall see below that the imaginary term of the scattering cross-section is indeed related to the X-ray absorption cross-section. For a bound electron with coordinates $\boldsymbol{x}$ the equation of motion is that of a forced harmonic oscillator,

$$\frac{\mathrm{d}^2\boldsymbol{x}}{\mathrm{d}t^2} + \Gamma_n\frac{\mathrm{d}\boldsymbol{x}}{\mathrm{d}t} + \omega_n^2\boldsymbol{x} = -\frac{e\boldsymbol{E}_0}{m_{\mathrm{e}}}\,\mathrm{e}^{-\mathrm{i}\omega t}, \tag{9.34}$$

where we have neglected the much smaller Lorentz term $-(e/m_{\mathrm{e}})(\boldsymbol{v}\times\boldsymbol{B})$ which is of the order v/c. Since the incident EM field $\boldsymbol{E} = \boldsymbol{E}_0\mathrm{e}^{-\mathrm{i}\omega t}$ impresses its frequency onto the charge, the displacement $\boldsymbol{x}$ and its time derivatives will all have the same $\mathrm{e}^{-\mathrm{i}\omega t}$ time dependence and the time derivative simply gives $-\mathrm{i}\omega$. This yields

$$\boldsymbol{x} = \frac{1}{\omega^2 - \omega_n^2 + \mathrm{i}\omega\Gamma_n} \frac{e\boldsymbol{E}_0}{m_\mathrm{e}} \tag{9.35}$$

and with $\boldsymbol{p} = -e\,\boldsymbol{x}$ and use of (9.13) and (9.17) we obtain for the frequency dependent scattering length of a bound electron n with resonance frequency ω_n

$$f_n(\omega) = r_0\, F_n(\omega)\, \boldsymbol{\epsilon} \cdot \boldsymbol{\epsilon}' \ . \tag{9.36}$$

The resonance factor $F_n(\omega)$ for a core electron n, given by

$$F_n(\omega) = \frac{\omega^2}{\omega^2 - \omega_n^2 + \mathrm{i}\omega\Gamma_n} \ , \tag{9.37}$$

is a dimensionless quantity that contains the frequency dependence of the scattering factor. With the definition $\sigma_\mathrm{e} = \int |f_\mathrm{e}(\omega)|^2 \mathrm{d}\Omega$ according to (9.21) we obtain for the angle integrated cross-section

$$\sigma_n^\mathrm{scat} = \frac{8\pi}{3} \frac{\omega^4}{(\omega^2 - \omega_n^2)^2 + (\omega\Gamma_n)^2}\ r_0^2 \ . \tag{9.38}$$

At resonance we have $\omega = \omega_n$ and we obtain

$$\sigma_n^\mathrm{scat} = \frac{8\pi}{3} \left(\frac{\omega_n}{\Gamma_n}\right)^2 r_0^2 \ = \left(\frac{\omega_n}{\Gamma_n}\right)^2 \sigma_\mathrm{e} \ . \tag{9.39}$$

The resonant scattering cross-section is enhanced by a factor $\omega_n^2/\Gamma_n^2 \approx 10^4$ over the nonresonant Thomson cross-section σ_e.[5]

For convenience let us rewrite $F_n(\omega)$ in terms of energy variables, the photon energy $E = \hbar\omega$, the resonance width $\Delta_n = \hbar\Gamma_n$ and the resonance position E_n. We then obtain for the resonance factor in (9.37)

$$F_n(E) = \frac{E^2}{E^2 - E_n^2 + \mathrm{i}E\Delta_n} \ . \tag{9.40}$$

Since $\Delta_n \ll E_n$ we can rewrite (9.40) as

$$F_n(E) \simeq 1 \ + \ F_n'(E) - \mathrm{i}F_n''(E) \tag{9.41}$$

with

$$F_n'(E) = \frac{E_n^2(E^2 - E_n^2)}{(E^2 - E_n^2)^2 + (E\Delta_n)^2} \ . \tag{9.42}$$

$F_n''(E)$ can be written as a Lorentzian[6] and is given by,

[5] In the limit $\omega \gg \omega_n \gg \Gamma_n$ we obtain Thomson's result for the scattering factor given by (9.18) and the scattering cross-section is independent of frequency. In the opposite limit $\omega, \Gamma_n \ll \omega_n$ we obtain the famous Rayleigh law, where the cross-section varies with ω^4.

[6] This is derived by using the approximation $(E^2 - E_n^2) = (E + E_n)(E - E_n) \simeq 2E(E - E_n)$ which follows from the fact that resonance effects are pronounced only over a small energy range where $E \sim E_n$ [362]. As shown in Appendix A.9, the Lorentzian given by 9.43 is characterized by a position E_n, full width at half maximum (FWHM) Δ_n, height E_n/Δ_n and area $\pi E_n/2$.

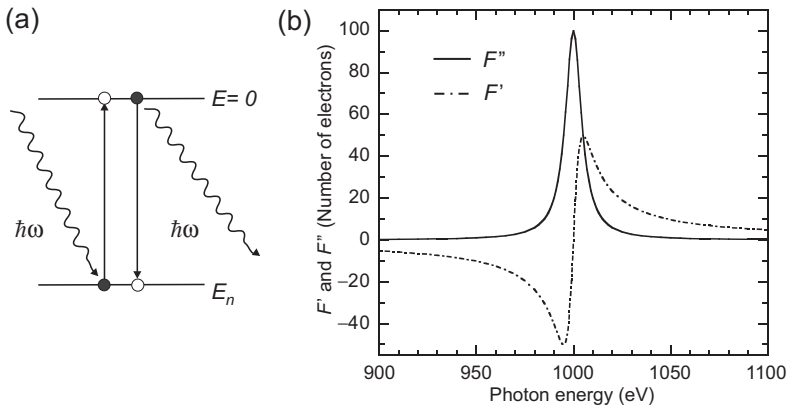

Fig. 9.5. (**a**) Resonant process in a simple one-electron picture. It consists of absorption of a photon through excitation of a core electron (*filled circle*) to an empty excited state (*open circle*), followed by a de-excitation process with photon emission. The process involves an energy difference E_n, yielding a single resonance. (**b**) Energy dependent resonance factors $F'(E)$ and $F''(E)$ corresponding to an excitation of a core electron of binding energy $E_n = 1,000\,\mathrm{eV}$ and resonance width $\Delta_n = 10\,\mathrm{eV}$, according to (9.42) and (9.43)

$$F''_n(E) = \frac{E_n}{\Delta_n}\,\frac{(\Delta_n/2)^2}{(E-E_n)^2+(\Delta_n/2)^2}\ . \tag{9.43}$$

The functions $F'_n(E)$ and $F''_n(E)$ are plotted in Fig. 9.5b for typical soft X-ray parameters $E_n = 1,000\,\mathrm{eV}$ and $\Delta_n = 10\,\mathrm{eV}$. Because of its lineshape, $F'_n(E)$ is often called the *dispersion term*.

Let us briefly estimate the relative size of the X-ray absorption and resonant X-ray scattering cross-sections. Using the relationship between $\sigma^{\mathrm{abs}}(E)$ and the scattering factor $F''(E) = f_2(E)$ given by (9.33) we can write for the case that the photon energy $E = \hbar\omega$ is near an atomic resonance energy E_n

$$\sigma^{\mathrm{abs}}_n(E) = 2r_0\lambda F''_n(E) = \frac{C^*}{E}F''_n(E) = \frac{C^*}{E}\frac{E_n}{\Delta_n}\,\frac{(\Delta_n/2)^2}{(E-E_n)^2+(\Delta_n/2)^2}\ . \tag{9.44}$$

Here $C^* = 2\,h\,c\,r_0 = 0.70\times10^8\,\mathrm{b\,eV}$. The absorption cross-section for a core electron in (9.44) has a peak value C^*/Δ_n. In the soft X-ray region $\Delta_n \simeq 10\,\mathrm{eV}$ so that the resonant X-ray absorption cross-section is about 10^7 b. This is to be compared to the scattering cross-section which according to (9.21) is obtained as

$$\sigma^{\mathrm{scat}}_n(E) = \sigma_{\mathrm{e}}\left\{[1\ +\ F'_n(E)]^2 + [F''_n(E)]^2\right\} = \sigma_{\mathrm{e}}\frac{E^4}{(E^2-E_n^2)^2+(E\Delta_n)^2}\ . \tag{9.45}$$

with a peak value of $\sigma_{\mathrm{e}}(E_n/\Delta_n)^2 \sim 10^4\,\mathrm{b}$. The resonant X-ray absorption cross-section is seen to be a factor of $\sim 10^3$ larger that the resonant X-ray scattering cross-section.

In our discussion above we have only considered a resonant process associated with one particular core shell of binding energy E_n. When the incident photon energy is near E_n the atomic response will be dominated by the shell n which "resonates." The other shells will not resonate and simply produce a constant "background" contribution due to nonresonant scattering. This background contribution is given by the atomic form factor $F^0(\boldsymbol{Q})$, defined in (9.24), which is the first term in the general expression of the scattering factor given by (9.2). The $\boldsymbol{Q}$-dependent general formulation of resonant scattering can be written in analogy to the nonresonant case given by (9.26). In particular, the differential atomic resonant scattering cross-section is given by

$$\begin{aligned}\left(\frac{\mathrm{d}\sigma}{\mathrm{d}\Omega}\right)^{\mathrm{scat}} &= |f(\boldsymbol{Q},E)|^2 = |f^0(\boldsymbol{Q}) + f'(E) - \mathrm{i}\,f''(E)|^2 \\ &= r_0^2\,|\boldsymbol{\epsilon}\cdot\boldsymbol{\epsilon}'|^2\,|F^0(\boldsymbol{Q}) + F'(E) - \mathrm{i}\,F''(E)|^2\ . \end{aligned} \tag{9.46}$$

In the limit of forward scattering we have $\boldsymbol{Q}=0$ and $\epsilon=\epsilon'$ and the form factor is simply given by the number of atomic electrons Z, i.e., $F^0(\boldsymbol{Q}=0)=F^0=Z$. This is reflected by replacing the factor 1 for one electron in (9.41) and (9.45) by the factor Z for all electrons in an atom, as assumed in (9.3). This yields the following expression for the *resonant forward scattering cross-section*

$$\left(\frac{\mathrm{d}\sigma}{\mathrm{d}\Omega}\right)^{\mathrm{scat}}_{\boldsymbol{Q}=0} = r_0^2\left\{[Z\,+\,F'(E)]^2 + [F''(E)]^2\right\} = r_0^2\left\{[f_1(E)]^2 + [f_2(E)]^2\right\}. \tag{9.47}$$

At the end of this section let us summarize the meaning of the different quantities used to describe the resonant scattering amplitude.

- The *resonant scattering factor* $F(\boldsymbol{Q},E) = F^0(\boldsymbol{Q}) + F'(E) - \mathrm{i}\,F''(E)$ has the dimension [number of electrons per atom].
- The *resonant scattering length* $f(\boldsymbol{Q},E) = r_0\,\boldsymbol{\epsilon}\cdot\boldsymbol{\epsilon}'F(\boldsymbol{Q},E)$ depends on polarization and has the dimension [length × number of electrons per atom].
- The *Henke–Gullikson factors* $f_1(E) = Z + F'(E)$ and $f_2(E) = F''(E)$ describe the case of small $|\boldsymbol{Q}|$ and have the dimension [number of electrons per atom].

9.4.3 Correspondence between Resonant Scattering and Absorption

Expression (9.47) gives the resonant forward scattering cross-section in terms of the real and imaginary parts of the resonant X-ray scattering factor $F(E) = f_1(E) - \mathrm{i} f_2(E)$. This link is particularly useful at long wavelengths where $|\boldsymbol{Q}|$ is small and the $\boldsymbol{Q}$-dependence may be neglected, in general. This case applies for photon energies below a few keV where the wavelength is much larger than the atomic size and in this "small atom" or "long-wavelength" limit one may conveniently define an *angle-integrated atomic scattering cross-section* similar to that for the single electron case (see (9.21) and (9.22)) by integration of (9.46) with $|\boldsymbol{Q}| = 0$ over the polarization factor. In the long-wavelength limit the *total atomic scattering cross-section* is given by

$$\sigma^{\mathrm{scat}}(E) = \int \left(\frac{\mathrm{d}\sigma}{\mathrm{d}\Omega}\right)_{|\boldsymbol{Q}|=0}^{\mathrm{scat}} \mathrm{d}\Omega = \sigma_{\mathrm{e}} \left\{ [f_1(E)]^2 + [f_2(E)]^2 \right\} . \tag{9.48}$$

We have also seen above in (9.33) that the X-ray absorption cross-section $\sigma^{\mathrm{abs}}(E)$ is directly linked to the imaginary part of the X-ray scattering factor $F''(E) = f_2(E)$. This important result is usually referred to as the *optical theorem*.

The *optical theorem* states that at long wavelengths (small $|\boldsymbol{Q}|$) the imaginary part of the scattering factor is directly related to the absorption cross-section according to

$$\sigma^{\mathrm{abs}}(E) = 2\, r_0\, \lambda\, \mathrm{Im}[F(\boldsymbol{Q}, E)]_{\boldsymbol{Q}\to 0} = \frac{C^*}{E} f_2(E) \ , \tag{9.49}$$

where $C^* = 2\, h\, c\, r_0 = 0.70 \times 10^8\, \mathrm{b\,eV}$.

The scattering factors and cross-sections for Fe metal, taken from the work of Kortright and Kim [353], are plotted in Fig. 9.6 in the vicinity of the L_3 and L_2 edges. Note the strong similarity of the lineshape of the scattering factors with those in Fig. 9.5.

9.4.4 The Kramers–Kronig Relations

The idea is to have a formalism that links both $F_n'(E)$ and $F_n''(E)$ to the X-ray absorption cross-section σ_n^{abs} which is easily measured. While this formalism naturally emerges from quantum mechanics, which allows transitions to both bound and continuum states, we shall nevertheless continue with our semi-classical model. It will yield the same results and lead us to the famous and important Kramers–Kronig relations.

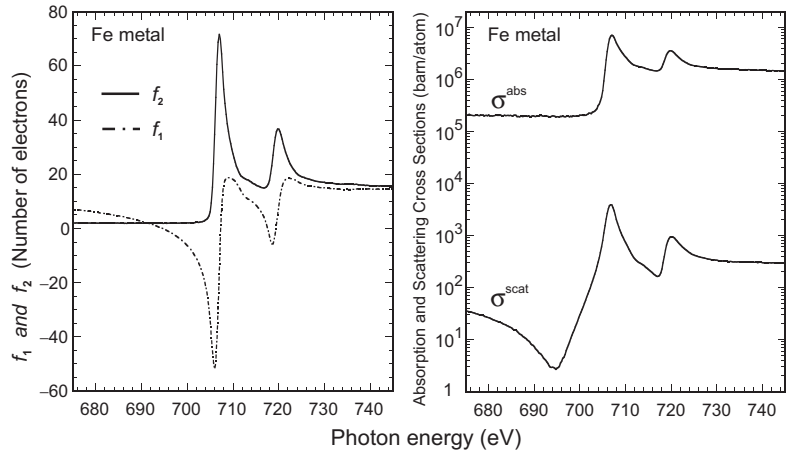

Fig. 9.6. *Left*: Measured energy dependent resonance factors f_1 and f_2 for the $L_{3,2}$-edges of Fe metal ($2p_{3/2}, 2p_{1/2} \rightarrow 3d$ transitions) [353]. *Right*: Energy dependent cross-sections for X-ray absorption (*top*) and scattering (*bottom*) calculated from the scattering factors according to (9.49) and (9.48), respectively

The *Kramers–Kronig relation* allows the determination of $F_n'(E)$ from the measured absorption cross-section $\sigma_n^{\rm abs}(\epsilon)$ according to

$$F_n'(E) = \frac{1}{C}\, P\!\int_0^\infty \frac{\epsilon^2\, \sigma_n^{\rm abs}(\epsilon)}{(E^2-\epsilon^2)}\, {\rm d}\epsilon\ . \tag{9.50}$$

Here $C = C^*\pi/2 = \pi\, h\, c\, r_0 = 1.098 \times 10^8\,{\rm b\,eV}$. In (9.50) we have replaced the lower integration limit by zero because the cross-section $\sigma_n^{\rm abs}(\epsilon)$ and hence the integral is zero for $\epsilon < E_n$. In practice, the integration is tricky because of the singularity for $\epsilon = E$ and at a given photon energy E the integral has to be evaluated by integrating from 0 to $E-\delta$ and from $E+\delta$ to ∞ and then taking the limit $\delta \rightarrow 0$. This is indicated by the "$P\!\int$" symbol, meaning "principal value" integral. Today this task is readily accomplished with modern mathematical software packages. In text books two Kramers–Kronig relations are typically found that relate the two resonance factors. The first one is obtained from (9.50) by use of the relation $\sigma_n^{\rm abs}(\epsilon) = C^* F_n''(\epsilon)/\epsilon$ in (9.49)

$$F_n'(E) = \frac{2}{\pi}\, P\!\int_0^\infty \frac{\epsilon\, F_n''(\epsilon)}{(E^2-\epsilon^2)}\, {\rm d}\epsilon\ , \tag{9.51}$$

and the second one allows the opposite transformation

$$F_n''(E) = \frac{2\,E}{\pi}\; P\!\int_0^\infty \frac{F_n'(\epsilon)}{(E^2-\epsilon^2)}\,\mathrm{d}\epsilon\ . \tag{9.52}$$

Again, the "$P\!\int$" symbol means principal value integral.

9.5 Quantum-Theoretical Concepts

9.5.1 One-Electron and Configuration Pictures of X-ray Absorption

In the simplest picture of resonant X-ray absorption a photon transfers its energy to a core electron and the electron is excited into an unoccupied electronic state. In this so-called *one-electron picture* we simply follow what happens to the photoelectron. This is also referred to as the *active electron approximation* [189] since we ignore what happens to all other "passive" electrons in the atom during the excitation process. Although this picture is not entirely correct since the "passive" electrons are not passive, it is quite intuitive, and because of its simplicity the picture is often used in the X-ray absorption literature.

Let us illustrate the one-electron picture for the L-edge X-ray absorption spectrum of a $3d$ transition metal atom, as shown in Fig. 9.7a. In the "initial

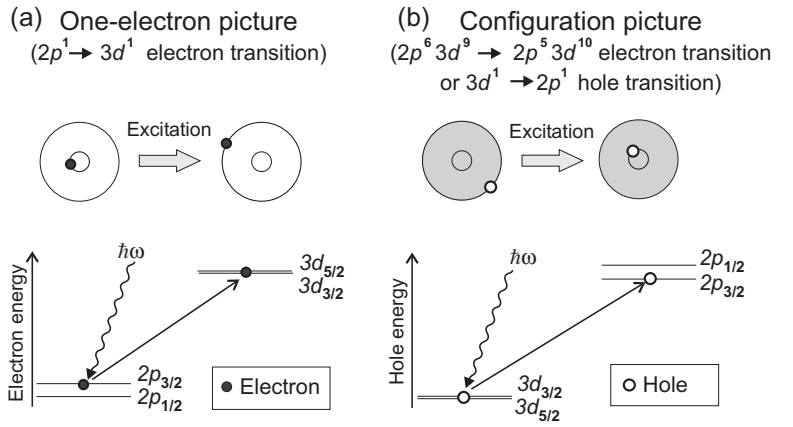

Fig. 9.7. Description of resonant L-edge X-ray absorption in two pictures, **(a)** one electron picture and **(b)** d^9 configuration picture. Each energy level is labeled by its quantum numbers $n, l, j = l \pm s$. In **(a)** the quantum numbers label one-electron states, in **(b)** they label hole states for the special case of a $3d^9$ electronic ground state, containing nine electrons or equivalently one hole. The two pictures are equivalent for the description of the electronic transitions

state" or $2p$ core state, the active electron has an angular momentum $l = 1$ and spin $s = 1/2$, so that the spin–orbit coupling, discussed in Sect. 6.4, produces two energy states with $j = l \pm s$. The four substates of $2p_{3/2}$ with $j_+ = 3/2$ experience an energy shift $E_{j_+} = \zeta_l/2$ and the two substates of $2p_{1/2}$ with $j_- = 1/2$ are shifted by $E_{j_-} = -\zeta_l$, with the separation given by the *Landé interval rule* $E_{j_+} - E_{j_-} = \zeta_l\, j_+$. In the "final state" the active electron is located in the $3d$ shell with angular momentum $l = 2$ and spin $s = 1/2$. The spin–orbit coupling again produces two energy states with $j = l \pm s$, i.e., the states $3d_{5/2}$ with $j = 5/2$ and $3d_{3/2}$ with $j = 3/2$, as shown in Fig. 9.7a. Because the core shell is more compact its spin–orbit coupling constant ζ_{2p} is considerably larger (of order 15 eV) than that of the valence shell ζ_{3d} (of order 50 meV), and the $2p_{3/2} - 2p_{1/2}(\mathrm{L_3} - \mathrm{L_2})$ splitting dominates, as seen in the experimental spectrum of Fe metal in Fig. 9.6.

The one-electron picture of Fig. 9.7a is misleading, however, especially to the photoemission community, in that it depicts the spin–orbit splitting of the p core shell as an "initial state" effect. It is clear that in reality the p shell is filled in the ground state and there is therefore no observable effect of the spin–orbit interaction. In the proper description of the X-ray absorption process, based on a *configuration picture*, an atom is excited from a ground or initial state configuration to an excited or final state configuration. In discussing transitions between configurations one typically omits all closed subshells since they are spherically symmetrical and their net angular momentum is zero [182]. Listing only the active shells, resonant L-edge absorption is described by an initial state electron configuration $2p^6 d^n$ and a final state configuration $2p^5 d^{n+1}$.

For transition metal atoms with configurations $1 \le n \le 9$ it is particularly easy to deal with the configuration d^9 in X-ray absorption, which is the configuration for Cu^{2+} (see Fig. 10.1a). In this case the initial state contains a filled p^6 shell and nine electrons in the d shell. A d^9 electron configuration is equivalent to a d^1 hole configuration and by taking proper care of signs it is often more convenient to carry out calculations in the corresponding hole rather than the electron picture. We shall do so in the following. Because of the cancellation of angular momenta in a filled shell we can simply describe the initial state as a d^1 hole configuration. The final state $p^5 d^{10}$ has a closed d-shell and a p^5 electron or p^1 hole configuration. Hence for a d^9 ground state, L-edge spectra in a configuration hole picture are described by a transition from the configuration d^1 to p^1. The spin–orbit splitting of the p shell is therefore properly described as a final state effect, as shown in Fig. 9.7b. We see that the two pictures in Fig. 9.7 are completely equivalent in describing the electronic transitions. Note that the energy order of the j states is inverted in the two schemes because electrons and holes have opposite spin.[7]

[7] This is expressed by Hund's third rule stating that the electronic ground state has the minimum possible j value for a less than half filled shell and the maximum possible j value for a more than half full shell.

In general, the one electron and configuration pictures are not equivalent. Differences arise when open shells with two or more holes or electrons need to be considered. In such cases *exchange and correlation effects* between the particles may be large as discussed in Chap. 7. Such effects lead to *multiplet structure* in the ground state, i.e., between the d electrons, as well as in the excited state, between the core p and valence d electrons. The simplest two-particle case is that of a p^6d^8 ground state configuration leading to a p^5d^9 excited state. This situation, which is encountered in NiO, can also be described (taking proper care of signs) by the equivalent case of a ground state d^2 hole configuration and an excited state pd hole configuration. Hence in both the ground state and excited states we have to consider the exchange and correlation between two holes. We shall discuss multiplet effects in more detail in Sect. 9.7.8.

Next we shall discuss how to calculate transition probabilities associated with X-ray excitation and de-excitation processes.

9.5.2 Fermi's Golden Rule and Kramers–Heisenberg Relation

The X-ray absorption and X-ray scattering cross-sections are both calculated by consideration of the time-dependent perturbation of the sample by the EM field. The time-dependent EM field induces transitions between an initial state $|i\rangle$ and final state $|f\rangle$, where both states contain an electronic and a photon part. If the system evolves directly from state $|i\rangle$ to $|f\rangle$ we speak of a first-order process, if some intermediate states $|n\rangle$ are involved we call it a second-order process. As illustrated schematically in Fig. 9.8, X-ray absorption is a first order and resonant X-ray scattering a second-order process.

The associated formalism was derived by Kramers and Heisenberg [366] and by Dirac [367]and the transition probability up to second order can be written as follows.

The *transition probability per unit time*, T_{if}, from a state i to a state f is given up to second order by,

$$T_{if} = \frac{2\pi}{\hbar}\left|\langle f|\mathcal{H}_{\rm int}|i\rangle + \sum_n \frac{\langle f|\mathcal{H}_{\rm int}|n\rangle\langle n|\mathcal{H}_{\rm int}|i\rangle}{\varepsilon_i - \varepsilon_n}\right|^2 \delta(\varepsilon_i - \varepsilon_f)\rho(\varepsilon_f). \quad (9.53)$$

The sum is over all possible states of energy ε_n. The dimension of T_{if} is [time^{-1}].

For X-ray absorption and resonant elastic scattering (including magnetic resonant scattering) the interaction Hamiltonian consists of the product of the momentum operator $\boldsymbol{p}$ and the vector potential $\boldsymbol{A}$ according to [147, 178, 368, 369]

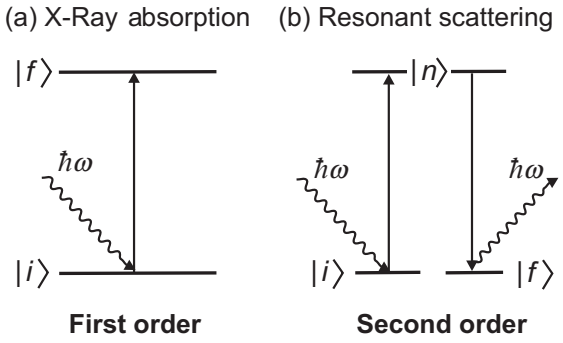

Fig. 9.8. Description of X-ray absorption and resonant elastic X-ray scattering as transitions between quantum mechanical states which are products of electronic and photon states. The X-ray absorption process corresponds to a *first-order* transition process between an initial state $|i\rangle$ and an excited state $|f\rangle$. The resonant scattering process is a *second-order* process that involves intermediate states $|n\rangle$. The system can pass through the intermediate states in a virtual sense that does not require energy conservation until the final state $|f\rangle$ is reached

$$\mathcal{H}_{\mathrm{e}}^{\mathrm{int}} = \frac{e}{m_{\mathrm{e}}} \boldsymbol{p} \cdot \boldsymbol{A} \ . \tag{9.54}$$

Since in free space $\boldsymbol{E} = -\partial \boldsymbol{A}/\partial t$ this expression means that the electronic transition is driven by the electric field $\boldsymbol{E}$ of the EM wave. The states and energies in (9.53) reflect those of the combined photon plus atom system. The wave functions $|i\rangle$ and $|f\rangle$ are products of electronic and photon states and the energies are sums of electronic and photon energies. The quantity $\rho(\varepsilon_f)$ is the density of final states per unit energy.

The *first-order term* in (9.53) was originally derived by Dirac [367] and called by Fermi the "Golden Rule No. 2" [370]. It is therefore often called by the somewhat misleading name *Fermi's golden rule*. The *second-order term*, referred to by Fermi as "Golden Rule No. 1" [370], was originally derived by Kramers and Heisenberg [366] and today is usually called the *Kramers–Heisenberg relation*. It gives the transition probability from $|i\rangle$ to $|f\rangle$ via a range of *virtual intermediate states* $|n\rangle$. The system can pass through the intermediate states in a virtual sense that does not require energy conservation until the final state is reached. This energy conservation is reflected by the delta function that involves only the initial and final states. With the dimensions of $\hbar$ [energy $\times$ time], $\rho(\varepsilon_f)$ [1/energy] and $|\mathcal{H}_{\mathrm{int}}|^2$ [energy^2], we obtain the dimension of T_{if} as [1/time].

The total cross-section is obtained from the transition probability per unit time T_{if} by normalization to the incident photon flux Φ_0.

$$\sigma = \frac{T_{if}}{\Phi_0} \ . \tag{9.55}$$

The numerator has the dimension [1/time] and the incident photon flux Φ_0, given by (5.18), has the dimension [1/(time × area)], so that σ has the dimension [area].

The differential cross-section $\mathrm{d}\sigma/\mathrm{d}\Omega$ reflects the number of transitions per unit time into the solid angle $\mathrm{d}\Omega$ and is given by

$$\frac{\mathrm{d}\sigma}{\mathrm{d}\Omega} = \frac{T_{if}}{\Phi_0 \, \mathrm{d}\Omega} \; . \tag{9.56}$$

9.5.3 Resonant Processes in the Electric Dipole Approximation

We now want to give the basic quantum mechanical expressions used for the calculation of polarization dependent X-ray absorption and resonant scattering processes. We would like to calculate the intensities of strong resonances like those associated with $2p_{3/2}, 2p_{1/2} \rightarrow 3d$ transitions in Fig. 9.6, commonly called "white lines" for historical reasons. In the early days, when photographic plates were used as detectors, the strong absorption resonances appeared etched into the black detector emulsion as white lines. In the following we shall adopt this terminology and often speak of the "white line intensity."

By quantizing the electromagnetic field [371] one can separate the matrix elements in (9.53) into electronic and photon parts, evaluate the photon part, and obtain the matrix elements in terms of transitions between two electronic states $|a\rangle$ and $|b\rangle$. The relevant matrix elements have the general form

$$\mathcal{M} = \langle \, b| \, \boldsymbol{p} \cdot \boldsymbol{\epsilon} \; \mathrm{e}^{\mathrm{i}\boldsymbol{k}\cdot\boldsymbol{r}}|a\rangle \; , \tag{9.57}$$

where $\boldsymbol{p}$ is the electron momentum vector, $\boldsymbol{\epsilon}$ the unit photon polarization vector, and $\boldsymbol{k}$ the photon wave vector. For the purpose of the present book it is sufficient to stay within the *dipole approximation*. Within this approximation one eliminates the $\boldsymbol{k}$-dependence of the matrix element and rewrites the electron momentum operator $\boldsymbol{p}$ in terms of the *length operator* $\boldsymbol{r}$ according to

$$\mathcal{M} = \langle \, b| \, \boldsymbol{p} \cdot \boldsymbol{\epsilon} \; (1 + \mathrm{i}\boldsymbol{k} \cdot \boldsymbol{r} + ...)|a\rangle \simeq \langle \, b| \, \boldsymbol{p} \cdot \boldsymbol{\epsilon}|a\rangle = \mathrm{i}m_\mathrm{e}\omega \langle \, b| \, \boldsymbol{r} \cdot \boldsymbol{\epsilon}|a\rangle \tag{9.58}$$

As before, m_e is the electron rest mass and $\omega = \omega_b - \omega_a$ the photon frequency associated with the transition from state $|a\rangle$ to state $|b\rangle$. The dipole approximation assumes that the size of the absorbing atomic shell is small relative to the X-ray wavelength, i.e., $|\boldsymbol{r}| \ll 1/|\boldsymbol{k}| = \lambda/2\pi$, so that the electric field which drives the electronic transition is constant over the atomic volume. In our case we are interested mostly in the photon energy range $\hbar\omega \leq 1,000\,\mathrm{eV}$ corresponding to a wavelength $\lambda \geq 1.2\,\mathrm{nm}$ and transitions from the $2p$ core shell of radius $|\boldsymbol{r}| \simeq 0.01\,\mathrm{nm}$ so that we have $|\boldsymbol{r}| \simeq 0.01\,\mathrm{nm} \ll \lambda/2\pi \simeq 0.2\,\mathrm{nm}$, and it is reasonable to use the dipole approximation.

In the dipole approximation the X-ray absorption cross-section is given by

$$\sigma^\mathrm{abs} = 4\pi^2 \, \frac{e^2}{4\pi\epsilon_0\hbar c} \, \hbar\omega \; |\langle b| \, \boldsymbol{\epsilon} \cdot \boldsymbol{r}|a\rangle|^2 \; \delta[\hbar\omega - (E_b - E_a)] \; \rho(E_b) \; , \tag{9.59}$$

where the density of final states per unit energy, $\rho(E_b)$, depends on the normalization of the electronic wavefunctions $|a\rangle$ and $|b\rangle$. The X-ray absorption resonance intensity, $I_{\rm res}$, is the energy integral over the cross-section and if we assume that the functions $|a\rangle$ and $|b\rangle$ have been volume normalized to unity one obtains the following expression that will be used throughout this chapter [190, 372].

The polarization dependent *X-ray absorption resonance intensity* in the *dipole approximation* is given by

$$I_{\rm res} = \mathcal{A}\ |\langle b|\,\boldsymbol{\epsilon}\cdot\boldsymbol{r}|a\rangle|^2\ . \tag{9.60}$$

The proportionality factor, given by

$$\mathcal{A} = 4\pi^2\frac{e^2}{4\pi\epsilon_0\hbar c}\,\hbar\omega \tag{9.61}$$

contains the dimensionless *fine structure constant* $\alpha_{\rm f}$

$$\alpha_{\rm f} = \frac{e^2}{4\pi\epsilon_0\hbar c} = \frac{1}{137.04}. \tag{9.62}$$

The intensity $I_{\rm res}$ has the dimension [length$^2\times$ energy] and is usually expressed in units of [Mb eV], where $1\,{\rm Mb} = 10^{-22}\,{\rm m}^2$.

If there are more than one discrete final state we need to sum the intensities associated with different final states. This is often expressed as a separate density of final state factor in the equation for the transition intensity, but we have included it in (9.60) into our final state description.

We see that the calculation of $I_{\rm res}$ boils down to the evaluation of the polarization dependent transition matrix element $\langle b|\,\boldsymbol{\epsilon}\cdot\boldsymbol{r}|a\rangle$. In the following we may therefore loosely refer to the squared matrix element with dimension [length^2] as the "transition intensity." The true intensity given by (9.60) has the dimension [energy $\times$ length^2].

Similarly, one can also evaluate the second-order term in (9.53) to obtain an expression for the resonantly scattered X-ray intensity. In the dipole approximation one again neglects the $\boldsymbol{k}$ dependence in the transition matrix elements.[8] By using the short hand notation for the resonant energies $E_{\rm R}^n = E_n - E_a$ and denoting the finite full width at half maximum (FWHM) of the intermediate state energy distributions as Δ_n one obtains the following differential resonant scattering cross-section.

[8] The same result is also obtained by assuming forward scattering, i.e., $\boldsymbol{k}_1 = \boldsymbol{k}_2$.

The polarization dependent *differential resonant X-ray scattering cross-section* in the *dipole approximation* is given by

$$\left(\frac{\mathrm{d}\,\sigma}{\mathrm{d}\Omega}\right)^{\mathrm{scat}} = |f(\hbar\omega)|^2 = \frac{\hbar^2\omega^4}{c^2}\ \alpha_{\mathrm{f}}^2 \left|\sum_n \frac{\langle a|\boldsymbol{r}\cdot\boldsymbol{\epsilon}_2^*|n\rangle\langle n|\boldsymbol{r}\cdot\boldsymbol{\epsilon}_1|a\rangle}{(\hbar\omega - E_{\mathrm{R}}^n) + \mathrm{i}(\Delta_n/2)}\right|^2 . \quad (9.63)$$

Here α_{f} is the dimensionless fine structure constant and $\boldsymbol{\epsilon}_1$ and $\boldsymbol{\epsilon}_2$ are the unit polarization vectors of the incident and scattered radiation.

In the following we shall establish the form of the polarization dependent dipole operator $\boldsymbol{\epsilon}\cdot\boldsymbol{r}$ and the form of the wavefunctions $|a\rangle$ and $|b\rangle$.

9.5.4 The Polarization Dependent Dipole Operator

According to (9.60) the *polarization dependent dipole operator* is given by the dot product $\boldsymbol{\epsilon}\cdot\boldsymbol{r}$. Here $\boldsymbol{r}$ is the electron position vector, given in Cartesian coordinates by

$$\mathbf{r} = x\mathbf{e}_x + y\mathbf{e}_y + z\mathbf{e}_z\ . \quad (9.64)$$

We are particularly interested in the X-ray absorption intensity for pure linear or circular polarization since we have seen in Sect. 4.4.1 that such pure polarization states can be produced today by suitable undulators. We have also discussed their mathematical description in Sect. 5.4. Here we want to distinguish cases of different polarization and different X-ray incidence directions in the (x, y, z) coordinate system of the sample. We express the angular momentum as $q\hbar$ so that $q = 0$ refers to linearly polarized light and $q = \pm 1$, or $q = \pm$ for short, to circularly polarized light.

For *linearly polarized X-rays*, the direction of the $\boldsymbol{E}$ vector determines the X-ray absorption intensity, and for the three extreme cases where $\boldsymbol{E}$ is aligned along x, y, and z we have the corresponding real unit polarization vectors

$$\boldsymbol{\epsilon}_x^0 = \boldsymbol{\epsilon}_x = \boldsymbol{e}_x \qquad \boldsymbol{\epsilon}_y^0 = \boldsymbol{\epsilon}_y = \boldsymbol{e}_y \qquad \boldsymbol{\epsilon}_z^0 = \boldsymbol{\epsilon}_z = \boldsymbol{e}_z\ . \quad (9.65)$$

For *circularly polarized* X-rays we consider the cases where the angular momenta, which are parallel to the X-ray wavevector $\boldsymbol{k}$, are aligned along x, y, and z. For circularly polarized X-rays with $\boldsymbol{k} \parallel z$ we write the unit polarization vector in accordance with (5.35) and (5.36) as

$$\boldsymbol{\epsilon}_z^{\pm} = \mp\frac{1}{\sqrt{2}}(\boldsymbol{\epsilon}_x \pm \mathrm{i}\,\boldsymbol{\epsilon}_y), \quad (9.66)$$

and for propagation along x or y we use a similar notation according to a right handed coordinate system, e.g., for $\boldsymbol{k} \parallel x$

$$\boldsymbol{\epsilon}_x^{\pm} = \mp\frac{1}{\sqrt{2}}(\boldsymbol{\epsilon}_y \pm \mathrm{i}\,\boldsymbol{\epsilon}_z). \quad (9.67)$$

The dipole operators $P^q_\alpha = \boldsymbol{\epsilon}\cdot\mathbf{r} = \boldsymbol{\epsilon}^q_\alpha\cdot\mathbf{r}$ in (9.60) can then be rewritten in terms of the familiar spherical harmonics $Y_{l,m}(\theta,\phi)$ [181, 182], and for $\alpha = z$ we have

$$P^\pm_z = \boldsymbol{\epsilon}^\pm_z\cdot\mathbf{r} = \mp\frac{1}{\sqrt{2}}\,(x \pm \mathrm{i}y) = r\sqrt{\frac{4\pi}{3}}\,Y_{1,\pm1}, \tag{9.68}$$

$$P^0_z = \boldsymbol{\epsilon}_z\cdot\mathbf{r} = \qquad z \qquad = r\sqrt{\frac{4\pi}{3}}\,Y_{1,0}. \tag{9.69}$$

Because of the prefactors of the spherical harmonics, it is more convenient to express the dipole operators in terms of *Racah's spherical tensor operators*.

Racah's spherical tensor operators are defined as [181],

$$C^{(l)}_m = \sqrt{\frac{4\pi}{2l+1}}\;Y_{l,m}(\theta,\phi)\;, \qquad \left(C^{(l)}_m\right)^* = (-1)^m C^{(l)}_{-m}\;. \tag{9.70}$$

We have listed these spherical tensors for $0 \le l \le 4$ in Table A.3. The polarization dependent electric dipole operators are related to Racah's tensor operators of rank $l = 1$, and we have for example

$$P^0_z = r\,C^{(1)}_0 = r\,\cos\theta = z, \tag{9.71}$$

$$P^\pm_z = r\,C^{(1)}_{\pm1} = \mp\,r\frac{1}{\sqrt{2}}\,\sin\theta\,\mathrm{e}^{\pm\mathrm{i}\phi} = \mp\frac{1}{\sqrt{2}}\,(x \pm \mathrm{i}y). \tag{9.72}$$

The dipole operators for all polarization cases ($q = 0, \pm1$) and orientations of the principal axes $\alpha = x, y, z$ of our sample coordinate system are listed in Table A.4. They can be written in the general form

$$P^q_\alpha/r = \sum_{p=0,\pm1} e^q_{\alpha,p}C^{(1)}_p = e^q_{\alpha,1}C^{(1)}_1 + e^q_{\alpha,0}C^{(1)}_0 + e^q_{\alpha,-1}C^{(1)}_{-1}\;, \tag{9.73}$$

where the coefficients $a^q_{\alpha,p}$ may be imaginary with $\sum_p |e^q_{\alpha,p}|^2 = 1$. The above discussion leads to the following form of the matrix element in (9.60) in terms of the polarization dependent dipole operators P^q_α,

$$\langle\, b|\boldsymbol{\epsilon}\cdot\boldsymbol{r}|a\rangle = \langle b|\,P^q_\alpha|a\rangle. \tag{9.74}$$

We can then rewrite (9.60) in its final form, to be used from now on.

The *X-ray absorption resonance intensity* for different X-ray propagation directions α and polarization states q can be written as

$$I_{\mathrm{res}} = \mathcal{A}\;|\langle b|\,P^q_\alpha|a\rangle|^2, \tag{9.75}$$

where $\mathcal{A}$ is given by (9.61) and the polarization dependent dipole operators P^q_α with $\alpha = x, y,$ or z and $q = +1, 0,$ or -1 are listed in Table A.4.

9.5.5 The Atomic Transition Matrix Element

The calculation of the transition matrix element depends on the wavefunctions $|a\rangle$ and $|b\rangle$. In a one-electron picture, the "initial state" $|a\rangle$ is given by the core electron wavefunction. The "final state" $|b\rangle$ consists of the valence electron wavefunctions.

The simplest wave functions are the atomic spin orbitals of the central field form given by (6.12) or

$$R_{n,l}(r)\, Y_{l,m_l}\, \chi_{s,m_s} = |R_{n,l}(r); l, m_l, s, m_s\rangle, \tag{9.76}$$

where the Dirac bra–ket notation is given on the right. $R_{n,l}(r)$ is the radial component of a shell n with angular momentum l, the spherical harmonics Y_{l,m_l} characterize the angular part and χ_{s,m_s} is the spin part. We shall see below that a general wavefunction appropriate for an atom in a solid, i.e., a ligand field or band state that includes bonding, exchange and spin–orbit effects, can in fact be written as a linear combination of atomic basis functions of the form (9.76). The atomic functions (9.76) are therefore of paramount importance and we shall first take a look at the calculation of transition matrix elements with such functions.

In a one-electron picture a "initial" state wavefunction for a core shell n with angular momentum c is given by

$$|a\rangle = |R_{n,c}(r); c, m_c, s, m_s\rangle \ , \tag{9.77}$$

where $R_{n,c}(r)$ is the radial component of the core shell with principal quantum numbers n and orbital quantum number c, and $|s = 1/2, m_s\rangle$ describes the spin state of the electron.

The "final" state will be of the form

$$|b\rangle = |R_{n',l}(r); l, m_l, s, m'_s\rangle \ , \tag{9.78}$$

where $R_{n',l}$ is the radial component of the valence state of shell n' with angular momentum l. The exclusion principle does not allow electrons to be excited into occupied states, and hence the final states are determined by the empty states in the l subshell. The task before us is then to calculate the transition matrix element

$$\langle b|\, P^q_\alpha\, |a\rangle = \langle R_{n',l}(r); l, m_l, s, m'_s|\, P^q_\alpha\, |R_{n,c}(r); c, m_c, s, m_s\rangle, \tag{9.79}$$

with the direction and polarization dependent dipole operators P^q_α given in Table A.4. We see from (9.73) that the matrix element in (9.79), in general, involves a sum over matrix elements of the Racah operators $C^{(1)}_q$. For a transition from a core shell with angular momentum c to an unfilled valence shell with angular momentum l we obtain

$$\langle b|\, P_\alpha^q\, |a\rangle = \underbrace{\delta(m_s', m_s)}_{\text{spin}}\ \underbrace{\langle R_{n',l}(r)|r|R_{n,c}(r)\rangle}_{\text{radial}}\ \underbrace{\sum_{m_c,m_l,p} e_{\alpha,p}^q\, \langle\, l, m_l|\, C_p^{(1)}\, |c, m_c\rangle,}_{\text{angular}} \tag{9.80}$$

where the coefficients $e_{\alpha,p}^q$ are those in Table A.4. The matrix elements factors into spin, radial, and angular parts. We see that the dipole operator does not act on the spin and only transitions are allowed that preserve the spin. The polarization dependence is entirely contained in the angular part of the wavefunctions. The radial part determines the angle integrated transition strength.

The Radial Part of the Atomic Transition Matrix Element

The radial dipole matrix element is given by

$$\mathcal{R} = \langle R_{n',l}(r)|r|R_{n,c}(r)\rangle = \int_0^\infty R_{n',l}^*(r)\, R_{n,c}(r)\, r^3 \mathrm{d}r\ , \tag{9.81}$$

where $\{n, c\}$ and $\{n', l\}$ describe the shell and subshell quantum numbers of the initial and final states, respectively.

The radial parts of the wavefunctions $R_{nl}(r)$ obey the normalization condition

$$\int_0^\infty |R_{nl}(r)|^2\, r^2\, \mathrm{d}r = 1\ . \tag{9.82}$$

In order to picture the radial extent of the transition matrix element $\mathcal{R}$ given by (9.81) we compare in Fig. 9.9 the function $r^3 R_{2p}(r) R_{3d}(r)$ for a $2p \rightarrow 3d$ transition to the functions $r^2 R_{nl}^2(r)$ for $nl = 1s$, $2p$, $3d$, using parameterized radial functions given by Griffith [228] for the Mn^{2+} ion.

The localization of $\mathcal{R}$ in the core region of the atom leads to some fundamental differences between X-ray absorption spectroscopy (XAS) and optical spectroscopy. Because of the small energy (of order of 1 eV) of optical transitions, electronic excitations occur only between filled and empty *valence* states. In many systems the probed valence states are extended states which are not localized on a specific atom and the intensity of optical transitions is determined by the group theoretical symmetry of the valence states, dictated by the molecule or crystal. In contrast, XAS is based on transitions involving core electrons which are localized on specific atoms. The function $R_{\text{core}}\, R_{\text{valence}}\, r^3$ which determines the integral $\mathcal{R}$ has its major contribution close to the atomic core, as shown in Fig. 9.9. It gives X-ray absorption spectroscopy its elemental specificity and local character. XAS may be viewed as an inverted linear combination of atomic orbitals (LCAO) scheme. The

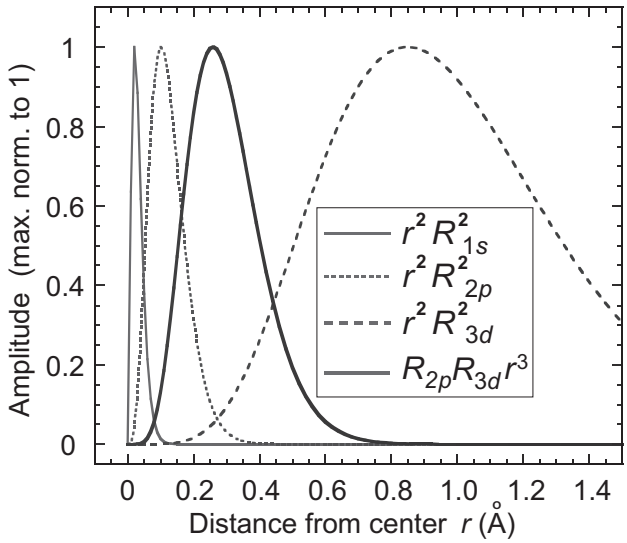

Fig. 9.9. *Top*: Radial functions $r^2\,R^2(r)$ for the $1s$, $2p$, and $3d$ orbitals of the Mn^{2+} ion, representing the probability of finding the electron at a distance r from the nucleus. Their maxima are often associated with the Bohr radii. Also plotted is the function $R_{2p}(r)\,R_{3d}(r)\,r^3$ (*thick solid line*), describing the localization of the $2p \rightarrow 3d$ transition matrix element, according to (9.81). All functions are plotted for the distance r from the atomic center and the amplitudes have been normalized to 1. The plotted Slater type functions are taken from Griffith [228]

LCAO scheme composes molecular functions from atomic functions, XAS decomposes the molecular functions into its atomic constituents. This is often referred to as the *one center approximation*.

> The strong localization of the core shell makes X-ray absorption spectroscopy element-specific and sensitive to the valence shell properties within the atomic volume.

The Angular Part of the Atomic Transition Matrix Element

The angular part of the transition matrix element (9.80) is determined by matrix elements of the form $\langle l, m_l |\, C_q^{(1)} \,| c, m_c \rangle$. For convenience, we have tabulated the nonzero matrix elements in Table 9.1.

By inspection of the nonvanishing matrix elements we can read off the *dipole selection rules*.

Table 9.1. Nonvanishing angular momentum dipole matrix elements $\langle L, M|C_q^{(1)}|l, m\rangle$. The matrix elements are real, so that $\langle L, M|C_q^{(1)}|l, m\rangle^* = \langle L, M|C_q^{(1)}|l, m\rangle = (-1)^q\langle l, m|C_{-q}^{(1)}|L, M\rangle$. Nonlisted matrix elements are zero.[a]

$\langle\, l+1, m|\, C_0^{(1)}\, |l, m\rangle$	$=$	$\sqrt{\dfrac{(l+1)^2-m^2}{(2l+3)(2l+1)}}$
$\langle\, l-1, m|\, C_0^{(1)}\, |l, m\rangle$	$=$	$\sqrt{\dfrac{l^2-m^2}{(2l-1)(2l+1)}}$
$\langle\, l+1, m+1|\, C_1^{(1)}\, |l, m\rangle$	$=$	$\sqrt{\dfrac{(l+m+2)(l+m+1)}{2(2l+3)(2l+1)}}$
$\langle\, l-1, m+1|\, C_1^{(1)}\, |l, m\rangle$	$=$	$-\sqrt{\dfrac{(l-m)(l-m-1)}{2(2l-1)(2l+1)}}$
$\langle\, l+1, m-1|\, C_{-1}^{(1)}\, |l, m\rangle$	$=$	$\sqrt{\dfrac{(l-m+2)(l-m+1)}{2(2l+3)(2l+1)}}$
$\langle\, l-1, m-1|\, C_{-1}^{(1)}\, |l, m\rangle$	$=$	$-\sqrt{\dfrac{(l+m)(l+m-1)}{2(2l-1)(2l+1)}}$

[a]The matrix elements $\langle\, l', m'|\, C_q^{(1)}\, |l, m\rangle = c^{k=1}(l'm'; lm)$ are tabulated by Condon and Shortley and by Slater [373]. Care has to be taken with the direction of the transition because it affects the sign according to $c^k(l'm'; lm) = (-1)^{m-m'}c^k(lm; l'm')$.

The *dipole selection rules* for transitions between states of the form $|n, l, m_l, s, m_s\rangle$ are:
$\Delta l = l' - l = \pm 1$,
$\Delta m_l = m_l' - m_l = q = 0, \pm 1$,
$\Delta s = s' - s = 0$,
$\Delta m_s = m_s' - m_s = 0$.
where $q\hbar$ is the X-ray angular momentum.

9.5.6 Transition Matrix Element for Atoms in Solids

Since solids, not atomic systems, are of main interest in magnetism research we need to discuss the calculation of the transition matrix element with more realistic initial and final state wavefunctions. Fortunately, within reasonable approximations, the wavefunctions of bonded atoms can be linked to the form of the atomic matrix element (9.80) because all wavefunctions can be written as linear combinations of the atomic functions, as seen from the form of the LF wavefunctions (7.30) and the $\boldsymbol{k}$-dependent band functions (7.22) or (7.23). If we use a tight binding band function written as

$$|\psi_i(\mathbf{k},r)\rangle = |R_{n,L}(r)\rangle\,|\phi_i(\mathbf{k})\rangle$$
$$= |R_{n,L}(r)\rangle \sum_{M=-L}^{+L} a_{i,M}(\mathbf{k})\,|L\,M\,\chi^+\rangle + b_{i,M}(\mathbf{k})\,|L\,M\,\chi^-\rangle, \quad (9.83)$$

with energy $E_i(\boldsymbol{k})$, the X-ray absorption transition intensity is given by

$$I_\alpha^q = \mathcal{A} \sum_{\substack{E_i>E_\mathrm{F}\\ i,\mathbf{k},m,j}} |\langle\psi_i(\mathbf{k},r)|\,P_\alpha^q\,|\varphi_m^j(r)\rangle|^2$$
$$= \mathcal{A}\,\mathcal{R}^2 \sum_{\substack{E_i>E_\mathrm{F}\\ i,\mathbf{k},m,j}} \left|\left\langle \phi_i(\mathbf{k}) \left| \sum_{p=0,\pm1} e_{\alpha,p}^q C_p^{(1)} \right| c\,m\,\chi^j \right\rangle\right|^2 . \quad (9.84)$$

By making use of the fact that the dipole operator does not act on spin we can separately sum over the orthogonal spin states χ^+ and χ^- and the resonance intensity takes the form

$$I_\alpha^q = \mathcal{A}\,\mathcal{R}^2 \sum_{\substack{E_i>E_\mathrm{F}\\ i,\mathbf{k},m}} \left| \sum_{p,M} a_{i,M}(\mathbf{k})\; e_{\alpha,p}^q\,\langle L\,M|C_p^{(1)}|c\,m\rangle \right|^2$$
$$+ \left| \sum_{p,M} b_{i,M}(\mathbf{k})\; e_{\alpha,p}^q\,\langle L\,M|C_p^{(1)}|c\,m\rangle \right|^2 . \quad (9.85)$$

Although the band states contain wavevector-dependent expansion coefficients, the matrix elements involve only atomic orbitals. We shall see later that the summation over $\boldsymbol{k}$, which in general is done by computer, can be done analytically for the case that one averages over all polarization states q or over three X-ray incidence angles $\alpha = x, y, z$. This yields an important sum rule that allows the determination of the number of unoccupied states.

Another important form of the wavefunctions are the spin–orbit basis functions $|R_{n,l}(r); l, s, j, m_j\rangle$. For example, as shown in Fig. 9.6, the L-edge spectra of the transition metals have $2p$ core spin–orbit splitting of about 15 eV, and one therefore needs to carry out the evaluation of the transition matrix element with the $2p_{3/2}$ and $2p_{1/2}$ eigenfunctions of the spin–orbit Hamiltonian (see Sect. 6.4.3 and 6.6.1). The angular parts of the spin–orbit coupled functions $|l, s, j, m_j\rangle$ can be expressed as a linear combination of the uncoupled functions $|l, s, m_l, m_s\rangle$ according to

$$|l, s, j, m_j\rangle = \sum_{m_l,m_s} C_{m_l,m_s;j,m_j}\,|l, s, m_l, m_s\rangle, \quad (9.86)$$

where the $C_{m_l,m_s;j,m_j}$ are the famous *Clebsch–Gordon* coefficients,[9] written in Slater's notation [225]. The radial parts are the same as before. For

[9] They are readily calculated by computer programs, e.g., *Mathematica*.

convenience, we given the s, p, and d functions in the bases $|l, s, j, m_j\rangle$ and $|l, s, m_l, m_s\rangle$ in Table A.5. We see that the calculation of the transition matrix element with spin–orbit coupled functions is just a little more complicated but follows the form (9.80).

Some Important General Rules

The X-ray absorption process for an atom in different environments and the states involved are illustrated Fig. 9.10. We have the following important rules:

- The sum over all basis states of a shell with angular momentum ℓ is spherically symmetric. Examples of basis states are the spherical harmonics, valence orbitals or spin–orbit states shown in Fig. 9.10.
- The one-electron $j = \ell \pm s$ manifolds created by the spin–orbit interaction are each spherically symmetric.
- The t_{2g} and e_g manifolds (see Fig. 9.10) of the d orbitals are each spherically symmetric.
- For a spherically symmetric shell the associated transition intensity does not depend on the choice of the basis states.
- If at least two of the three parts of the dipole matrix element $\langle\, b \,|\, P^q_\alpha \,|\, a \,\rangle$ are spherically symmetric, the squared matrix element or intensity becomes independent of the direction α and polarization q.

In general, the measured X-ray absorption spectra of atoms in magnetic solids depend on three key parameters:

- The sample orientation
- The X-ray polarization
- The external magnetic field

From a pedagogical point of view it is best to distinguish and consecutively discuss two general cases. The first case corresponds to measurements that *average over all sample orientations* relative to the X-ray beam. In practice, this is simply accomplished by averaging over three orthogonal measurements. The significance of this procedure, discussed later, is that the so-determined spectral intensities are directly related by simple sum rules to important physical quantities per atom, like the number of empty valence states, the spin magnetic moment and the orbital magnetic moment.

The second case is more complicated and corresponds to a single measurement that *depends on the orientation of the sample*. Now the measured spectral intensities no longer correspond to quantities that are integrated over the atomic volume but they may also contain anisotropic, i.e., direction dependent, contributions. For example, if the spin density in the atomic volume is not spherical, the XMCD intensity measured for different sample orientations will not simply determine the (isotropic) spin moment but rather the anisotropic spin density.

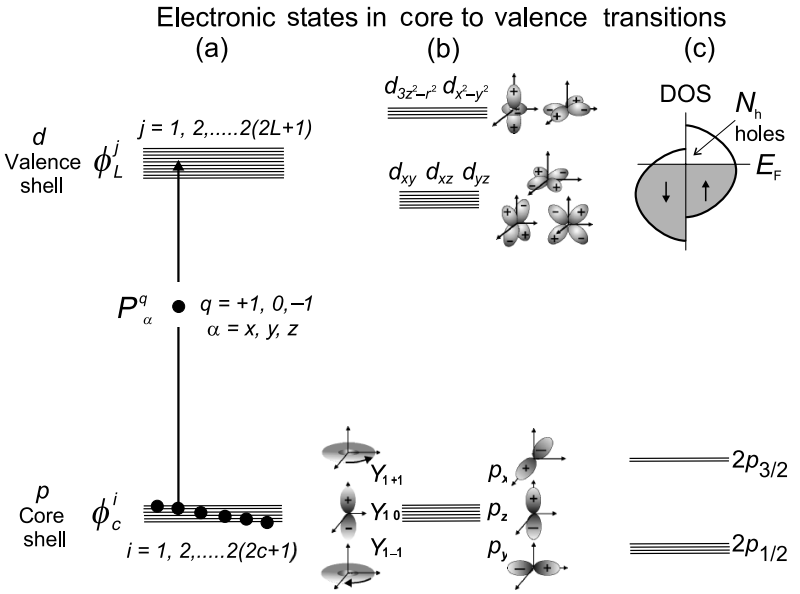

Fig. 9.10. Schematic of electronic core and valence states, and dipole transitions between them in a one-electron model. (**a**) Atomic case, illustrating a transition from a filled core state $|\phi_c^i\rangle$ in shell n, given by (9.77), to an empty valence state $|\phi_L^j\rangle$ in shell n', described by (9.78). Both states are labeled by their angular momenta $l = c$ and $l = L$ and there are $2(2l + 1)$ substates or spin orbitals within each manifold l. The electric dipole operator P_α^q is one of the operators given in Table A.4, where $q = +1, 0, -1$ labels the possible angular momentum transfer and $\alpha = x, y, z$ the direction. (**b**) Ligand field case for the case of $p \rightarrow d$ transitions (L-edge). The filled core shell is spherically symmetric and can be described either in a basis of spherical harmonics or p orbitals given in Table A.2. The valence states are linear combinations of the atomic states (9.77) and (9.78) and correspond to the d orbitals in Table A.2. The upper two d orbitals are the e_g, while the lower three are the t_{2g} orbitals. Each set is spherically symmetric. (**c**) States for a transition metal. The valence shell is represented by spin-up and spin-down d states with a total number of empty d states above the Fermi energy E_F, called the number of valence holes, N_h, ("up" plus "down" spins). The core state is assumed to be spin–orbit split into $2p_{3/2}$ and $2p_{1/2}$ states, giving rise to the L_3 and L_2 edges in experimental spectra, respectively. Note that each core manifold $j = 3/2$ and $j = 1/2$ is spherically symmetric

For these reasons we shall separately discuss the two cases later. We will apply the theoretical concepts developed above for the calculation of angle integrated and polarization dependent transition intensities. In the process the link between the transition intensities and physical parameters will emerge.

9.6 The Orientation-Averaged Intensity: Charge and Magnetic Moment Sum Rules

In understanding the significance of the resonance intensity in X-ray absorption spectra it is best to first discuss measurements that eliminate magnetic effects, if present, and give charge-related information only. In the following we shall specifically discuss the important case of the L-edge spectra of transition metals. We will show that such spectra, properly averaged over all sample orientations yield the total number of unoccupied valence states or holes.

9.6.1 The Orientation-Averaged Resonance Intensity

For our discussion it is useful to start by defining an X-ray absorption resonance or white-line intensity that is independent of sample orientation. We shall assume that our sample has higher than monoclinic symmetry so that the unit cell axes are orthogonal. One can then define an orientation averaged absorption intensity as the average over three orthogonal measurements. If we use the notation (9.73) (also see Table A.4) for our polarization (q) and X-ray propagation (α) dependent dipole operator P^q_α, one can show as done in Sect. 9.6.2, that the average may involve either a sum over q or α according to

$$\langle I \rangle = \frac{1}{3}\left(I^q_x + I^q_y + I^q_z\right) = \frac{1}{3}\left(I^{-1}_\alpha + I^0_\alpha + I^{+1}_\alpha\right) \ . \tag{9.87}$$

Let us illustrate this average for different cases. The simplest case is a *nonmagnetic polycrystalline* sample. In this case the polarization of the incident X-rays does not matter since the electric field vector $\boldsymbol{E}$ that drives the electronic transition is oriented at random relative to the crystallographic directions of the sample. The recorded spectrum therefore corresponds to a true angular average.

For *nonmagnetic single crystals* with higher than monoclinic symmetry the same angle-averaged intensity can be obtained by averaging over three orthogonal measurements according to (9.87). For the special case of cubic symmetry the measured spectral intensity is isotropic and a single measurement suffices. For lower symmetry, the required *average over* α depends on the polarization labelled by q. For linear polarized X-rays ($q = 0$) one averages over spectra for $\boldsymbol{E}$ along the x, y, and z axes of the crystal. For natural light or circularly polarized light ($q = \pm 1$)[10] one averages over three measurements with $\boldsymbol{k}$ along x, y, and z. For a fixed crystalline direction α *the average over* q $(0, \pm 1)$ ensures that the $\boldsymbol{E}$-vector can equally drive the transition along the x, y, and z axes of the crystal (see Table A.4), and therefore an effective average is performed.

[10] For circularly polarized X-rays the photon spin does not matter for nonmagnetic samples. To the absorbing charge the light looks naturally polarized with $\boldsymbol{E}$ lying somewhere in the plane perpendicular to $\boldsymbol{k}$.

For *magnetic single crystals* one can use the same method as for nonmagnetic single crystals if one uses linearly polarized light. For circularly polarized X-rays one must eliminate magnetic effects by saturating the sample with the field parallel and antiparallel to the direction α and summing over the two intensities. The angle-averaged resonance intensity obeys an important intensity sum rule that can be stated as follows.

> The *angle-averaged intensity* of the combined L_3 and L_2 resonances is directly proportional to the total number of d states above the Fermi level, i.e., the number of holes in the d band.

This is demonstrated in Fig. 9.11a for the $L_{3,2}$ white-line intensity of the absorption spectra of the pure metals Fe, Co, Ni, and Cu. The shown spectra were recorded for polycrystalline and magnetically not aligned samples so that polarization dependent effects are automatically averaged out. Of interest is the white-line resonant intensity associated with $2p \rightarrow 3d$ transitions, shown shaded in the inset of Fig. 9.11a, which sits on a step-like background due to nonresonant excitation channels. The nonresonant channels produce steps at the L_3 and L_2 positions with a step ratio of 2 to 1 reflecting the number of core electrons in the $p_{3/2}$ and $p_{1/2}$ core states.

The white line intensity near threshold dramatically decreases along the series. This is due to filling of the $3d$ band with increasing number of electrons or atomic number Z, in accordance with the densities of states shown in Fig. 12.1. In total, the d shell can hold 10 electrons and by going from Fe to Cu one adds approximately one electron per atom. By summing for each energy the number of d states over the Brillouin zone one obtains the d band density of states, $\rho(E_{3d})$, as schematically shown in Fig. 9.11b. By energy integration $N_\mathrm{h} = \int_{E_\mathrm{F}}^{\infty} \rho(E)\mathrm{d}E$ from the Fermi level up one obtains the total number of empty d band states or d holes. When the resonance intensity is plotted against the theoretically obtained number of $3d$ holes one obtains a linear relationship as shown in Fig. 9.11c. The resonance intensity of the spectrum, defined as the shaded peak area in the inset of Fig. 9.11a, is the energy integral over the cross-section and has the dimension [area $\times$ energy], and in Fig. 9.11 is given in units of Mb eV.

9.6.2 Derivation of the Intensity Sum Rule for the Charge

Figure 9.11b shows the electronic states appropriate for a transition metal. The total number of empty d states above the Fermi energy E_F, called the number of valence holes, N_h, is simply the number of spin up plus down states. In the one-electron model the core state is assumed to be spin–orbit split into $2p_{3/2}$ and $2p_{1/2}$ states, giving rise to the L_3 and L_2 edges in experimental spectra, respectively. The sum rule states that the transition intensity is proportional to the total number of empty d states N_h when we sum over the $2p_{3/2}$ and $2p_{1/2}$ contributions. This is intuitively correct since the intensity should increase if we make more empty final states available for the transition.

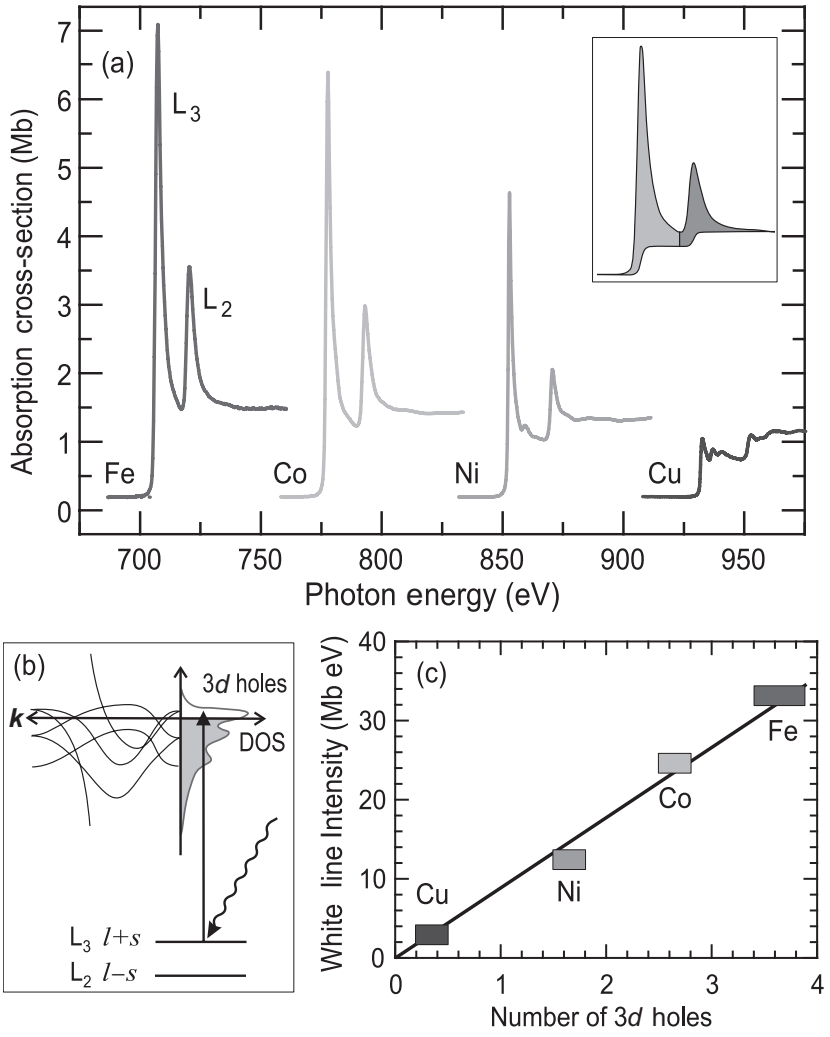

Fig. 9.11. (**a**) L-edge X-ray absorption spectra, plotted on an absolute cross-section scale, for the 3*d* transition metals Fe, Co, Ni, and Cu. When the sum of the L_3 and L_2 intensities, defined as the area shown *shaded* in the inset, is plotted against the calculated number of 3*d* holes a linear relationship is obtained within experimental error as shown in (**c**). We have used the following values for the number of holes: 1.5–1.78 for Ni, 2.5–2.80 for Co and 3.4–3.93 for Fe (also see Sect. 12.2.2 and Fig. 12.16). The correlation follows from a sum rule, discussed in the text, that links the integrated resonance cross-section or resonance intensity to the number of empty valence states in the electronic ground state. The number of empty states is obtained from the integrated density of states (DOS), as shown in (**b**)

Let us derive the sum rule using a tight binding band picture for the $3d$ valence states of the transition metals. The intensity of an electronic transition between core states of angular momentum c and valence states of angular momentum $L = c + 1$ is given by (9.85). By separating off the diagonal and cross terms we have

$$I^q_\alpha = \mathcal{A}\,\mathcal{R}^2 \sum_{\substack{E_i > E_\mathrm{F} \\ i,\mathbf{k},m}} \sum_{p,M} \left[\, |a_{i,M}(\mathbf{k})|^2 + |b_{i,M}(\mathbf{k})|^2 \,\right] \, |e^q_{\alpha,p}|^2 |\langle L\,M|C^{(1)}_p|c\,m\rangle|^2$$

$$+ \mathcal{A}\,\mathcal{R}^2 \sum_{\substack{E_i > E_\mathrm{F} \\ i,\mathbf{k},m}} \sum_{\substack{p \neq p' \\ M \neq M'}} e^q_{\alpha,p}(e^q_{\alpha,p'})^* \, \langle L\,M|C^{(1)}_p|c\,m\rangle \langle L\,M'|C^{(1)}_{p'}|c\,m\rangle^*$$

$$\times \left[\, a_{i,M}(\mathbf{k})(a_{i,M'}(\mathbf{k}))^* + b_{i,M}(\mathbf{k})(b_{i,M'}(\mathbf{k}))^* \,\right]. \quad (9.88)$$

We can now perform an orientation average according to (9.87) by either summing of the three orthogonal polarization states $q = 0, \pm 1$ or over crystal directions $\alpha = x, y, z$. In both cases the cross term in (9.88) vanishes because $\sum_q e^q_{\alpha,p}(e^q_{\alpha,p'})^* = \sum_\alpha e^q_{\alpha,p}(e^q_{\alpha,p'})^* = 0$ for all p, p' combinations (see Appendix A.6), and the polarization averaged transition intensity is given by

$$\langle I\rangle = \frac{1}{3}\mathcal{A}\,\mathcal{R}^2 \underbrace{\sum_{\substack{E_i > E_\mathrm{F} \\ i,\mathbf{k},M}} \left(\, |a_{i,M}(\mathbf{k})|^2 \, + |b_{i,M}(\mathbf{k})|^2 \right)}_{N_\mathrm{h}} \underbrace{\sum_{p,m} |\langle L\,M|\, C^{(1)}_p|c\,m\rangle|^2 \underbrace{\sum_{q \text{ or } \alpha} |e^q_{\alpha,p}|^2}_{=1}}_{=\,L/2L+1}$$

$$= \mathcal{A}\,\mathcal{R}^2 \, \frac{L}{3(2L+1)} \, N_\mathrm{h}. \quad (9.89)$$

Here we have used (A.25) and (A.27) and the sum rule (A.21), and N_h is the total number of holes according to (7.25). This is an important result and we need to put a box around it. For the L-edge of the $3d$ transition metals the sum rule reads as follows.

The *orientation averaged "white line" intensity* of a core to valence $nc \rightarrow n'L$ transition with $c = L - 1$ is directly related to the total number of valence holes N_h in the *electronic ground state* according to

$$\langle I\rangle = C\, N_\mathrm{h} \; . \quad (9.90)$$

where

$$C = \mathcal{A}\,\mathcal{R}^2 \, \frac{L}{3(2L+1)} \; , \quad (9.91)$$

$\mathcal{A} = 4\pi^2\hbar\omega/137$ and $\mathcal{R}$ is the radial $nc \rightarrow n'L$ matrix element.

Note that according to (9.87), we have defined the angle-averaged intensity $\langle I \rangle$ to be equivalent to that obtained for a randomly oriented sample in a single measurement. It is of great importance, as stated above, that N_h is the total number of valence holes in the *electronic ground state*, not the excited electronic state. This is not obvious from our one-electron model calculation but can be proven in a more general configuration based model of the X-ray absorption process [100, 101]. For the special case of a $p \rightarrow d$ transition we have

$$\langle I \rangle = \frac{2\,\mathcal{A}\,\mathcal{R}^2}{15}\,N_\mathrm{h}\ . \tag{9.92}$$

9.6.3 Origin of the XMCD Effect

The important intensity sum rule for the number of holes suggests that if we could make the absorption process spin dependent we could measure an intensity difference that corresponds to the difference between the number of spin-up and spin-down holes, i.e., the magnetic moment. This can indeed be done by using circularly polarized photons and is the basis of XMCD spectroscopy.

Before we proceed we need to specifically state our assumptions. In using the important concept of proportionality of the white line intensity and the number of valence holes from the previous sections we implicitly assume that the measured white line intensity is independent of the sample crystallography. In the following we shall therefore assume that the sample is either polycrystalline or that we average three dichroism measurements along orthogonal crystalline directions.[11]

In order to understand the essence of the XMCD effect we assume a one-electron picture where the valence states exhibit a Stoner splitting as discussed in Sect. 7.4.2, and shown on the left side of Fig. 9.12. The shown density of states actually correspond to that calculated for Fe metal by band theory (see Fig. 12.1).

For maximum XMCD effect the magnetization direction $\boldsymbol{M}$ of the sample and the photon spin or angular momentum $\boldsymbol{L}_\mathrm{ph}$ are chosen to be *collinear*. As illustrated on the left side of Fig. 9.12, the dichroism effect is then given by the difference of the $p \rightarrow d$ transition (X-ray absorption) intensities, measured for photons with positive angular momentum ($q = +1$, $\boldsymbol{L}_\mathrm{ph}$ points in direction of wavevector $\boldsymbol{k}$) and negative angular momentum ($q = -1$, $\boldsymbol{L}_\mathrm{ph}$ points in direction of $-\boldsymbol{k}$) aligned along the fixed magnetization direction $\boldsymbol{M}$ of the sample. An equivalent way is to fix the X-ray photon spin direction and switch the magnetization directions [374].

On the right of Fig. 9.12 we show experimental L-edge XMCD spectra for Fe metal [96, 375] that have been corrected to correspond to 100% circularly

[11] More specifically, we also assume that the sample symmetry is higher than monoclinic so that the unit cell axes are orthogonal.

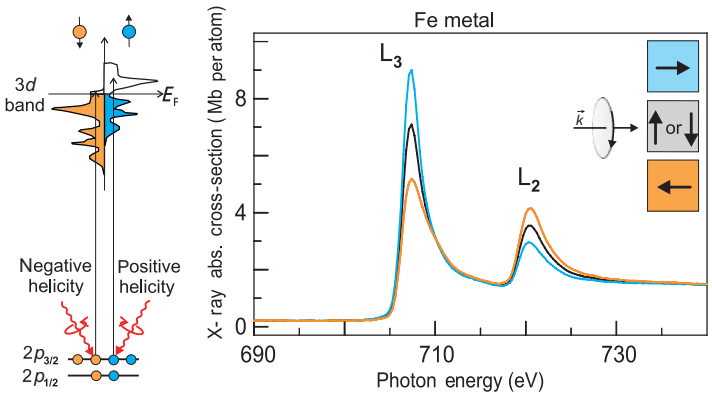

Fig. 9.12. The XMCD effect illustrated for the L-edge absorption in Fe metal. The shown density of spin-up and spin-down states closely resembles that calculated for Fe metal (compare Fig. 12.1). The experimental data on the right are from Chen et al. [96] and have been corrected to correspond to 100% circular polarization. We show the case of circularly polarized X-rays with positive angular momentum (helicity), and the color coded spectra correspond to the shown sample magnetization directions

polarized X-rays and parallel alignment of the photon spin and the magnetization. The dichroism effect is seen to be very large. If the photon spin is aligned perpendicular to the magnetization the cases of perpendicular "up" and "down" magnetization directions cannot be distinguished.

Denoting the *magnetization* $\boldsymbol{M}$ and *photon angular momentum* $\boldsymbol{L}_{\rm ph}$ directions by arrows, the dichroism effect is only dependent on the relative alignment of the two arrows. The convention adopted by the XMCD community is to plot the dichroism intensity of the $3d$ transition metals Fe, Co, and Ni so that the L_3 dichroism is negative (also see Fig. 10.12). According to Fig. 9.12 this corresponds to the definition,

$$\Delta I = I^{\uparrow\downarrow} - I^{\uparrow\uparrow}. \tag{9.93}$$

Note that the *minority* electron spin direction (= majority hole spin direction) is the same as that of the sample magnetization. The importance of the so defined XMCD intensity can be expressed as follows.

The *XMCD difference intensity*, defined as the white-line intensity difference between antiparallel and parallel orientations of the sample magnetization and the incident photon spin is directly proportional to the atomic magnetic moment.

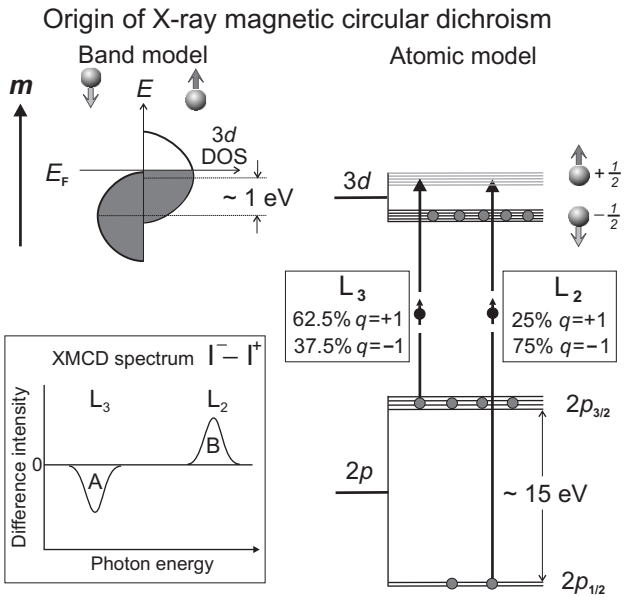

Fig. 9.13. Illustration of the L-edge X-ray absorption processes of circularly polarized photons with angular momentum $q = \pm 1$ (in units of $\hbar$). For the d valence shell we show the correspondence between the Stoner band picture of a magnetic material and an atomic one-hole d shell model. We have chosen our magnetization direction such that the "down-spins" are filled and the "up-spins" partially unfilled. In the atomic model we assume one "spin-up" hole and show the possible $2p$ core to $3d$ valence transitions assuming circularly polarized light with angular momentum q. The fraction of "up-spin" electrons excited from the p core shell through absorption of X-rays with angular momentum $q = \pm 1$ is listed for the L_3 and L_2 edges. Here we have assumed the X-rays to be incident parallel to the atomic magnetic moment $\boldsymbol{m}$. In the inset we show the XMCD difference spectrum calculated with the atomic model according to (9.95) and assuming the shown resonant peak shapes

The quantum mechanical origin of the XMCD effect at the L-edge is explained in more detail by the simple atomic model of Fig. 9.13. Here we have assumed the case of a "strong" ferromagnet with one filled spin channel. With the sample magnetized in the "up" direction, the spin-down states are filled and the spin-up states are only partially filled as shown in Fig. 9.13. For simplicity we ignore the weak spin–orbit interaction among the d electrons so that our sample has only a spin magnetic moment and the orbital moment is zero. We also show the correspondence between the Stoner band picture of a magnetic material and an atomic d shell model. In both cases the five spin-down d states are filled and the spin-up states are assumed to be par-

tially filled. For an empty spin-up shell the magnetic moment is $5\,\mu_\mathrm{B}$ in our simple atomic model and as we fill in more electrons it decreases by $1\,\mu_\mathrm{B}$ per (spin-up) electron.

For the special situation of a completely filled majority band shown in Fig. 9.13, the charge sum rule of Sect. 9.6.1 would actually be sufficient to give us the magnetic moment since it is equal to the total number of holes. In general, of course, we have to allow for partially filled majority and minority bands and therefore we need to make the X-ray absorption process spin dependent in order to determine the difference in majority and minority population.

For our quantum mechanical calculation we use the atomic model shown on the right side of Fig. 9.13 and calculate the dichroism effect by considering the angular part of the squared transition matrix element from the $p_{3/2}$ and $p_{1/2}$ states to the empty spin-up states of the d-band. We write the $p_{3/2}$ and $p_{1/2}$ wave functions in the basis $|l=\ 1, m_l, s, m_s\rangle$, as is done in Table A.5. For the spin-up $3d$ hole states we use the five d orbitals listed in Table A.2 with spin up $|\chi^+\rangle = |m_s = +1/2\rangle$. They are linear combinations of basis functions $|l=2, m_l, s, m_s\rangle$ so that all matrix elements can be calculated from the expressions in Table 9.1 under the assumption of spin conservation. The individual transition intensities (angular part only) are given by

$$|\langle d_n, \chi^+| \, \frac{P_z^q}{r} \, |p_j, m_j\rangle|^2 \tag{9.94}$$

with index values $n = 1, \ldots, 5$, $j = 3/2, 1/2$, $m_j = \pm 3/2, \pm 1/2$ and $q = 0, \pm 1$. The individual squared transition matrix elements are given in Fig. 9.14.

From the individual transition intensities in Fig. 9.14 we can now derive the XMCD effect. With the definition of (9.93) it is given by the difference of the $p \rightarrow d$ transition intensities with negative ($q = -1$) and positive ($q = +1$) photon spin,

$$\Delta I = I^{\uparrow\downarrow} - I^{\uparrow\uparrow} = I^- - I^+. \tag{9.95}$$

By summing the appropriate intensities and differences in Fig. 9.14 we obtain for the $\mathrm{L_3}$ and $\mathrm{L_2}$ dichroism effects:

$$\begin{aligned} \Delta I_{\mathrm{L_3}} &= \mathcal{A}\mathcal{R}^2 \sum_{n,m_j} |\langle d_n, \chi^+ | C_{-1}^{(1)} | p_{3/2}, m_j\rangle|^2 - |\langle d_n, \chi^+ | C_{+1}^{(1)} | p_{3/2}, m_j\rangle|^2 \\ &= -\frac{2}{9}\mathcal{A}\mathcal{R}^2 \, , \end{aligned} \tag{9.96}$$

and

$$\begin{aligned} \Delta I_{\mathrm{L_2}} &= \mathcal{A}\mathcal{R}^2 \sum_{n,m_j} |\langle d_n, \chi^+ | C_{-1}^{(1)} | p_{1/2}, m_j\rangle|^2 - |\langle d_n, \chi^+ | C_{+1}^{(1)} | p_{1/2}, m_j\rangle|^2 \\ &= +\frac{2}{9}\mathcal{A}\mathcal{R}^2 \, . \end{aligned} \tag{9.97}$$

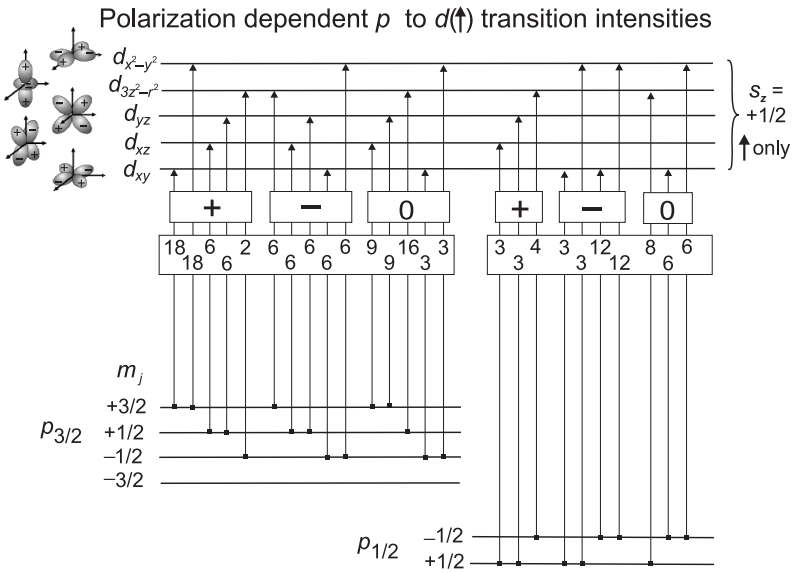

Fig. 9.14. Polarization dependent transition intensities in a one-electron model from spin–orbit and exchange split p core states $|j, m_j\rangle$ to *spin-up* ($m_s = +1/2$) d valence orbitals (Table A.2), assumed to be split by the exchange interaction. The listed intensities each need to be divided by 90 to get the proper absolute values in units of $\mathcal{A}\mathcal{R}^2$. We have chosen the z-axis as the spin quantization axis and the transition intensities are for circular polarization with $\boldsymbol{k} \parallel z$ and angular momenta $q = +1$ (labeled +) and $q = -1$ (labeled −) and for linear polarization with $\boldsymbol{E} \parallel z$ (labeled $q = 0$). We have assumed a splitting of the p states by the exchange interaction, lifting the degeneracy in m_j. Note that this causes an opposite order of m_j states for $p_{3/2}$, $l + s$ and $p_{1/2}$, $l - s$ because of the opposite sign of s

The relevant XMCD intensities are summarized in Fig. 9.13. The dichroism signal at the L_3 and L_2 edges are identical in magnitude but of opposite sign. At the L_3 edge, X-rays with positive ($q = 1$) photon spin excite more *spin-up* electrons than X-rays with negative ($q = -1$) photon spin, and at the L_2 edge the opposite is found. It is easy to show that for the calculation of the dichroism effect it is equivalent to fix the X-ray spin and switch the magnetization direction [374]. In principle, L-edge X-ray absorption spectra contain contributions from both $p \rightarrow d$ and $p \rightarrow s$ transitions, but in practice the $p \rightarrow d$ channel dominates by a factor > 20. [376]

9.6.4 Two-Step Model for the XMCD Intensity

The model calculations in Figs. 9.13 and 9.14 suggest a particularly simple two-step model.

In the *first* X-ray absorption step, conservation of angular momentum requires a transfer of the angular momentum of the incident circularly polarized X-rays to the excited photoelectrons. If the photoelectron is excited from a spin–orbit split level, e.g., the $2p_{3/2}$ level (L_3 edge), the angular momentum of the photon can be transferred in part to the spin through the spin–orbit coupling and the excited photoelectrons are spin polarized. The spin polarization is opposite for incident X-rays with positive ($+\hbar$) and negative ($-\hbar$) photon spin. Also, since the $2p_{3/2}$ (L_3) and $2p_{1/2}$ (L_2) levels have opposite spin–orbit coupling ($l + s$ and $l - s$, respectively) the spin polarization will be opposite at the two edges. The photoelectron spin quantization axis is identical to that of the photon spin, i.e., it is parallel or antiparallel to the X-ray propagation direction.

In the *second* step the exchange split valence shell with unequal spin-up and spin-down populations acts as the detector for the spin of the excited photoelectrons. For optimum detection the valence shell spin quantization axis (the "detector" axis) has to be aligned with the photon spin or photoelectron spin quantization axis.

For the specific case shown in Fig. 9.13 only spin-up electrons can be excited from the $2p$ core to the partially unfilled spin-up $3d$ valence shell because the dipole operator does not act on spin and therefore does not allow spin-flips during excitation. At the L_3-edge, X-rays with positive spin ($q = +1$) excite 62.5% spin-up electrons and negative spin X-rays ($q = -1$) excite 37.5% spin-up electrons, while for the L_2 edge the numbers are 25% spin-up electrons for $q = +1$ and 75% spin-up electrons for $q = -1$. Taking into account the two times higher population of the $2p_{3/2}$ state, one finds the dichroic intensity differences at the L_3 and L_2 edges calculated according to (9.96) and (9.97) where $\Delta I_{L_3} = A$ and $\Delta I_{L_2} = B$, to be identical in magnitude but of opposite sign, as shown in the inset of Fig. 9.13.

The results of Fig. 9.13 are readily extended to the general case where both majority and minority bands are partially empty since for transitions to spin-down (majority) states the same excitation percentages given in Fig. 9.13 are found, except with $q = +1$ and $q = -1$ interchanged. Thus the minority and majority band contributions to the dichroism intensity have opposite signs. If both contribute equally the dichroism signal vanishes, as required for a nonmagnetic material.

Note that the pure photon spin configurations with angular momenta $\pm\hbar$ are not converted into pure (100%) electron spin configurations. Some of the photon angular momentum is converted into electron orbital momentum which is also carried by the photoelectron. The photoelectron thus carries the angular momentum absorbed from the photon as spin and orbital momentum degrees of freedom. The orbital momentum of the photoelectron is detected if the valence shell has an orbital moment. A particularly interesting case is that of K-shell excitations.

K-shell Dichroism

For K-shell excitation the $1s$ core shell has zero angular momentum and hence no spin–orbit coupling. It may, however, exhibit a small splitting into $m_s = \pm 1/2$ states due to the exchange field or an external magnetic field. In Fig. 9.15 we give the polarization dependent transition intensities for two cases.

On the left side of Fig. 9.15 we show transitions from the spin-split $1s$ shell to empty exchange split $2p$ orbitals with $m_s = +1/2$ given by

$$|\langle p_n, m_s = +1/2| \, \frac{P_z^q}{r} \, |s, m_s\rangle|^2 \tag{9.98}$$

for $n = 1 \ldots 3$ and $q = 0, \pm 1$. On the right we show transitions from the spin–split $1s$ shell to empty spin–orbit coupled $2p_j$ ($j = 3/2, 1/2$) orbitals, further split by an external magnetic field into $-3/2 \leq m_j \leq +3/2$ Zeeman components,

$$|\langle p_j, m_j| \, \frac{P_z^q}{r} \, |s, m_s\rangle|^2 \tag{9.99}$$

for $j = 3/2, 1/2$, $m_j = \pm 3/2, \pm 1/2$, $m_s = \pm 1/2$, and $q = 0, \pm 1$. Note that our results for this case confirm those given earlier in Fig. 8.1.

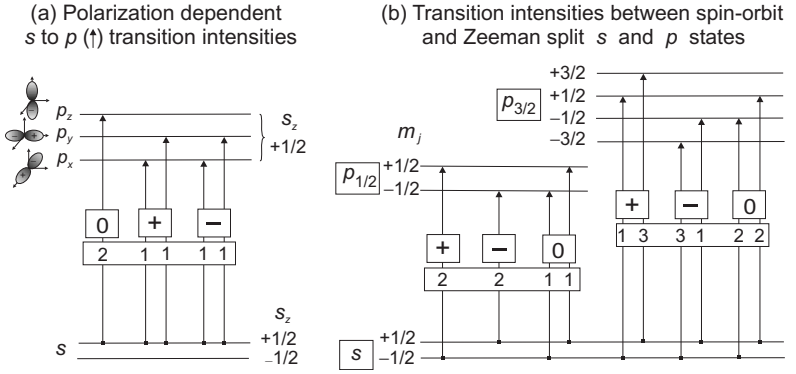

Fig. 9.15. (**a**) Polarization dependent transition intensities in a one-electron model between exchange (or Zeeman) split s core states and empty spin-up ($s_z = +1/2$) p valence orbitals, assumed to be separated from the full spin-down shell by the *exchange interaction*. The listed intensities each need to be divided by 6 to get the proper absolute values in units of $\mathcal{AR}^2$. We have chosen the z-axis as the spin quantization axis and the transition intensities are for circular polarization with $\boldsymbol{k} \parallel z$ and angular momenta $q = +1$ (labeled $+$) and $q = -1$ (labeled $-$) and for linear polarization (labeled $q = 0$) and $\boldsymbol{E} \parallel z$. (**b**) Transition intensities between exchange (or Zeeman) split s core states and spin-orbit coupled and *Zeeman split* p_j valence states denoted by quantum numbers m_j (see Table A.5). The listed intensities each need to be divided by 9 to get the proper absolute values. The coordinate system is the same as in (**a**).

For the K-edge excitation the $1s$ state has only a spin and no orbital angular momentum. Since the spin does not interact directly with the electric field, the photon spin is transferred to the photoelectron as an orbital angular momentum, either $\hbar$ or $-\hbar$. The orbital angular momentum of the photoelectron can only be detected by the valence shell if it possesses an orbital magnetic moment itself, that means if the valence band empty density of states has an imbalance of states with quantum numbers $+m_l$ and $-m_l$. If the valence shell does not possess an orbital moment, photoelectrons with orbital momenta $\hbar$ and $-\hbar$ cannot be distinguished and no dichroism effect will be observable. This is true even if the valence shell has a net spin polarization as in the Stoner model. Therefore, for K-shell excitation a dichroism effect exists only if the p valence shell possesses an orbital moment [377]. Sensitivity to the spin magnetic moment of the p shell arises only indirectly through the spin–orbit interaction.

Summary for the XMCD Intensity

We can summarize the models shown in Figs. 9.13–9.15 by the following two-step model of XMCD [374].

> The *two-step model* of XMCD:
> • In the *first step*, circularly polarized X-rays generate photoelectrons with a spin and/or orbital momentum from a localized atomic inner shell.
> • In the *second step*, the $3d$ shell serves as the detector of the spin or orbital momentum of the photoelectron. For maximum effect, the photon spin needs to be aligned with the magnetization direction.

The size of the dichroism effect depends on three important parameters:

- The degree of circular photon polarization P_{circ},
- The expectation value of the magnetic moment of the $3d$ shell $\langle \boldsymbol{m} \rangle$
- The angle θ between the directions of the photon angular momentum $\boldsymbol{L}_{\mathrm{ph}}$ and the magnetic moment $\boldsymbol{m}$

This can be cast into the following dependence of the XMCD intensity,

$$\boxed{I_{\mathrm{XMCD}} \propto P_{\mathrm{circ}}\ \boldsymbol{m} \cdot \boldsymbol{L}_{\mathrm{ph}} \propto P_{\mathrm{circ}} \langle \boldsymbol{m} \rangle \cos\theta}\ . \tag{9.100}$$

In theory we define the XMCD difference intensity according to (9.95), assuming $P_{\mathrm{circ}} = 1$. For our later discussion of the resonant magnetic scattering intensity is useful to write the XMCD absorption intensity in a form that involves matrix elements of Racah's spherical tensors, as done for the L_3 and L_2 signals in (9.96) and (9.97). By use of the short form

$$\langle C_q^{(1)} \rangle = \langle d_n, \chi^+ | C_q^{(1)} | p_j, m_j \rangle, \tag{9.101}$$

we can state as follows.

The *XMCD difference intensity* for X-ray propagation and magnetization direction aligned along z may be written in terms of angular matrix elements of the Racah spherical tensors according to,

$$\Delta I_{\mathrm{XMCD}} = \mathcal{A}\mathcal{R}^2 \sum_{\text{states}} |\langle C^{(1)}_{-1}\rangle|^2 - |\langle C^{(1)}_{+1}\rangle|^2. \tag{9.102}$$

The factor $\mathcal{A}$ is given by (9.61) and $\mathcal{R}$ is the radial transition matrix element given by (9.81).

9.6.5 The Orientation Averaged Sum Rules

In this section we want to formally state three important sum rules for orientation averaged intensities [100–102, 240, 241, 378–383]. The sum rules link the measured polarization dependent resonance intensities with valence band properties, in particular the number of empty states or "holes" N_{h} per atom, the spin magnetic moment m_s per atom and the orbital magnetic moment m_o per atom. Since these latter atomic quantities are defined by integration over the atomic volume and are therefore *isotropic* quantities, one needs to be sure that the measurement eliminates anisotropic effects caused by anisotropic charge and spin densities in the crystallographic unit cell. It is therefore necessary, in general, to first define a coordinate system for the crystallographic axes, so that one can properly average out anisotropies by suitable measurements.

In the following we shall assume that the crystal symmetry is higher than monoclinic so that we can chose the unit cell axes along the x, y, and z directions of a cartesian coordinate system. For a measurement we then specify the X-ray polarization and the magnetization direction in this frame and define a suitable intensity average according to (9.87). With this definition we can now use intensity averages of three measurements to determine physical quantities.

First we can determine the number of empty valence states per atom by measuring the transition intensity of core electrons into the empty valence states, as illustrated schematically in Fig. 9.16a for the L-edge in the magnetic $3d$ transition metals. We then have the first of three important sum rules, which we shall call the *charge sum rule*. It relates the measured averaged peak intensity to the number of empty states N_{h}. We can state it as follows.

The *charge sum rule* links the measured averaged X-ray absorption resonance intensity of a core to valence transition to the number of empty valence states N_{h} per atom

$$\langle I\rangle = C\, N_{\mathrm{h}}, \tag{9.103}$$

where C is the proportionality constant given by (9.91).

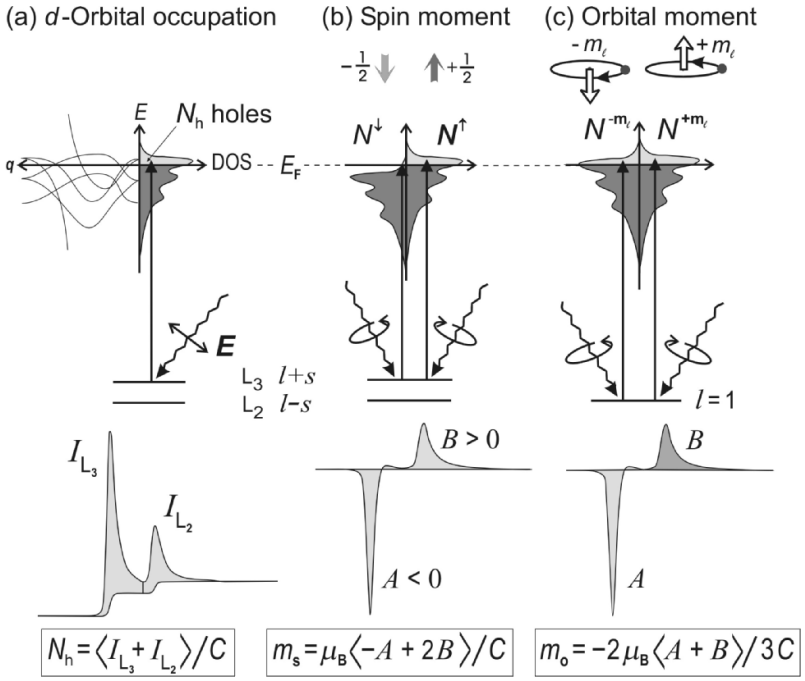

Fig. 9.16. Schematic of processes, spectra, and intensities underlying the quantitative determination of valence band properties such as the number of empty d states N_h, and the spin moment $m_s = \mu_\mathrm{B}(N_\mathrm{h}^{\uparrow} - N_\mathrm{h}^{\downarrow}) = \mu_\mathrm{B}(N_\mathrm{h}^{+m_s} - N_\mathrm{h}^{-m_s})$ and orbital moment $m_o = \mu_\mathrm{B}(N_\mathrm{h}^{+m_\ell} - N_\mathrm{h}^{-m_\ell})$. At the bottom we indicate the relationship between measured spectral intensities and the valence band properties. Note the sign of the dichroism difference intensities. In the shown cases we have $A < 0$ and $B > 0$

For the special case of the transition metal L-edges one needs to determine the total core to valence intensity given by the sum of the two spin–orbit split components as shown in Fig. 9.16a and (9.103) takes the form [102]

$$\langle I_{\mathrm{L}_3} + I_{\mathrm{L}_2} \rangle = C N_\mathrm{h} \ . \tag{9.104}$$

If the X-ray absorption spectrum is determined in terms of the absolute cross-section (with the dimension [area]) then the measured intensity I, given by the energy integration of the cross-section, has the dimension [area × energy], and therefore C is typically given in conventional units of [Mb eV]. For the $3d$ transition metals it has a value of about 10 Mb eV (see Fig. 9.17) [384].

In order to derive the magnetic spin moment for the $3d$ transition metals according to a sum rule due to Carra et al. [101] we also need to carry out an average as proposed by Stöhr and König [102]. One uses circularly polarized

light and measures XMCD spectra for $\boldsymbol{k}$ along the three crystallographic directions x, y, z. For each measurement one magnetically *saturates* the sample along the direction of $\boldsymbol{k}$ and determines the dichroic (difference) intensities A and B at the L_3 and L_2 edges as shown in Fig. 9.16b by either switching the photon spin for a given magnetization direction or by switching the magnetization direction for a given photon spin. Note that large fields of several Tesla may be needed for full magnetic alignment of the sample. One then performs the average of the difference intensities according to (9.87). This leads to the so-called *spin sum rule*. Note that in the case shown in Fig. 9.16 the areas A and B have opposite signs.

The *spin sum rule* links the angle averaged dichroism intensities with the size of the spin moment per atom according to

$$\langle -A + 2B \rangle = \frac{C}{\mu_{\mathrm{B}}}\, m_s \ . \tag{9.105}$$

where the constant C is the same as in the charge sum rule.

For Fe, Co, and Ni the orbital, m_o, and spin, m_s, moments are parallel because the d shell is more than half full. While the spin moment becomes anisotropic only in higher order through the spin–orbit coupling which is significantly smaller than the dominant isotropic exchange interaction, the orbital moment may be strongly anisotropic. The origin of this anisotropy lies in the ligand field which may preferentially destroy the orbital motion of the electrons about certain crystal axes as discussed in Sect. 7.9. One therefore also needs to average over three directions to determine the average orbital moment. The three measurements are identical to those for the spin moment yet for the sum rule analysis one takes a different linear combination of the dichroism intensities. The orbital moment is determined by use of the *orbital moment sum rule* due to Thole et al. [100]

The *orbital moment sum rule* links the angle averaged dichroism intensities with the size of the average orbital moment per atom according to

$$-\langle A + B \rangle = \frac{3C}{2\mu_{\mathrm{B}}}\, m_o \ . \tag{9.106}$$

The constant C is the same as in the charge and spin sum rules.

In practice, the determination of m_o requires high quality data and careful data analysis since $A+B$ is typically a small number, obtained by subtraction of two large numbers since $A < 0$ and $B > 0$. If the two intensities have the same size but opposite signs the orbital moment is zero.

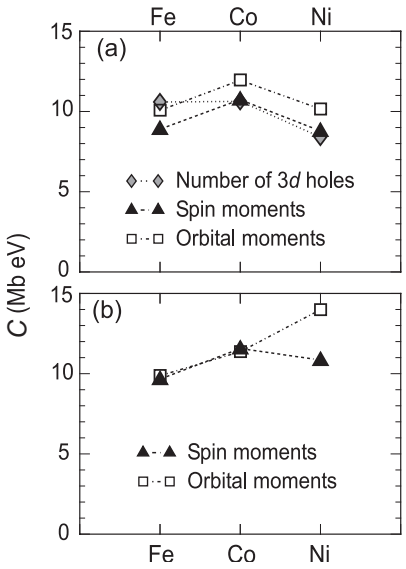

Fig. 9.17. Values for the constant C in the X-ray absorption sum rules determined by use of (9.103)–(9.106) from experimentally measured intensities and literature values for N_{h}, m_s, and m_o [384]. In (**a**) we used the values N_{h}, m_s, and m_o obtained by density functional theory including orbital polarization [385, 386] and in (**b**) the spin and orbital moments determined from the gyromagnetic ratio [387]

Figure 9.17 shows results for the constant C determined for Fe, Co, and Ni from experimental data and "known" values for the magnetic moments and the d shell occupation. A true determination of C is more difficult than first imagined since even for the elemental transition metals, there are some discrepancies between experimental and theoretical values for the moments. Furthermore, XMCD only measures the d electron contribution to the moments because $2p \rightarrow 4p$ transitions are not allowed by the dipole selection rule and $2p \rightarrow 4s$ transitions have much smaller cross-sections [376] than $2p \rightarrow 3d$ transitions.

If the intensities are not angle averaged, additional terms arise for the charge and spin moment sum rules that can be written in terms of a intraatomic quadrupolar charge contribution and a nonspherical intraatomic spin distribution. These terms average to zero when an angular average is performed as assumed earlier [102]. We shall come back to these anisotropic terms in Sect. 9.7.9.

9.7 The Orientation-Dependent Intensity: Charge and Magnetic Moment Anisotropies

In Sect. 9.6 we have treated the case of angle averaged X-ray absorption intensities. We assumed that the sample is either polycrystalline, of cubic symmetry or that a suitable angular average of three orthogonal crystalline directions is performed. In modern magnetism research, one often encounters single crystal samples or thin films with anisotropic bonding. We shall now discuss the X-ray absorption spectra of such samples, which may be magnetically oriented, for the cases of linearly and circularly polarized X-rays. In the process we shall encounter the generalization of the three orientation averaged sum rules discussed in Sect. 9.6.5.

The discussion of the orientation-dependent intensities naturally leads to the distinction between spectra recorded with linearly polarized X-rays and circularly polarized X-rays and we shall discuss the two cases in turn.

9.7.1 Concepts of Linear Dichroism

The term "linear dichroism" describes angle dependent effects when the direction of the linear polarized $\boldsymbol{E}$ vector is changed relative to the sample.[12] In nonmagnetic systems the anisotropy arises from an anisotropic charge distribution about the absorbing atom caused by bonding. For magnetic samples an additional anisotropy may exist relative to the magnetization direction of the sample. It is important to realize that in all cases the measured anisotropy arises from a nonspherical charge distribution. If the origin of the charge anisotropy is due to bonding alone we speak of "natural" linear dichroism, when it has a magnetic origin we use the term "magnetic" linear dichroism. Both may co-exist and in this case they can be separated either by temperature dependent studies or, for ferromagnets, by rotation of the magnetic alignment field relative to the fixed X-ray polarization .

Because of the close connection between the "natural" and "magnetic" dichroism effects we need to discuss both. We start with the case of nonmagnetic systems and present the physical origin of natural linear dichroism.

9.7.2 X-ray Natural Linear Dichroism

The easiest way to visualize the polarization dependence underlying X-ray natural linear dichroism or XNLD is the "search light effect" [189]. It can be stated as follows.

[12] Note that natural or circular polarized light defines a polarization plane perpendicular to the propagation direction $\boldsymbol{k}$ and therefore both also give rise to an angular polarization effect when the sample is turned in the beam. For nonmagnetic samples this case can be treated by assuming that one has two orthogonal linearly polarized $\boldsymbol{E}$-vector components perpendicular to $\boldsymbol{k}$, and the intensities $\propto |\boldsymbol{E}_i|^2$ $(i = 1, 2)$ associated with the two components are added incoherently, i.e., there is no interference term.

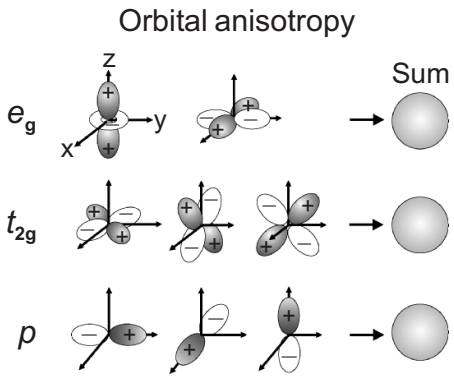

Fig. 9.18. Spatial orientation of p and d orbitals. All individual orbitals are anisotropic but the sums of the e_g and t_{2g} d orbitals or the sum of the p orbitals is spherically symmetric as shown

In an X-ray absorption experiment electrons are excited from a selected core shell to empty valence states. For *linear polarized X-rays* the electric field vector $\boldsymbol{E}$ acts like a *search light* for the direction of the maximum and minimum number of empty valence states. The transition intensity is directly proportional to the number of empty valence states in the direction of $\boldsymbol{E}$.

In an X-ray absorption measurement we sum over all degenerate levels of the core state. In accordance with Fig. 9.18 this leads to a spherically symmetric core contribution. This is obvious for K-edge spectra where the $1s$ core state is spherically symmetric. For L-edge spectra we also get a spherical core contribution if we sum over the $p_{3/2}(\mathrm{L}_3)$ and $p_{1/2}(\mathrm{L}_2)$ intensities. The dependence of the X-ray absorption intensity on $\boldsymbol{E}$-vector orientation is then entirely determined by the spatial distribution of the *empty valence states*.

The search light effect can be readily demonstrated for the case of K- and L-edges, where the electronic transitions involve $1s \rightarrow 2p$ and $2p \rightarrow 3d$ core-to-valence excitations. All we have to look for is the spatial charge distribution of the empty valence states involved in the transitions. For convenience we can do this by picturing the valence states by the familiar real p and d orbitals, as illustrated in Fig. 9.18. In a cubic ligand field the d orbitals form the e_g and t_{2g} irreducible representations. The sum of the orbitals within each representation is spherically symmetric. The p orbitals are not split in cubic symmetry and their sum is also spherically symmetric. In cubic symmetry the X-ray absorption intensity in nonmagnetic materials is therefore independent of $\boldsymbol{E}$-vector orientation relative to the sample.

It is clear that the charge distribution of the *individual* p and d orbitals is asymmetric in space, and therefore as the symmetry is lowered below cubic, transitions to individual p and d orbitals will depend on the orientation of the $\boldsymbol{E}$-vector relative to the x, y, z coordinate system of the crystal. This is the origin of the natural linear dichroism effect. Some of the most beautiful examples of this effect are found for small molecules or organic molecules with directional covalent bonds as discussed in detail in the book *NEXAFS Spectroscopy* [189].

For the K-edge we readily recognize the foundation of the search light effect, since the p orbitals have directions of maximum charge density and perpendicular nodal planes where the charge density is zero. The X-ray absorption intensity is maximum when $\boldsymbol{E}$ is aligned along the orbital and is zero when $\boldsymbol{E}$ lies in the *nodal plane*. One can remember the search light effect by the following simple picture. The photoelectron is ejected from the spherically symmetric core state along the direction of the $\boldsymbol{E}$-vector. The $\boldsymbol{E}$-vector "search light" then senses the hole density of the valence orbital. If the density in the direction of $\boldsymbol{E}$ is zero the transition intensity vanishes. In general, the transition intensity scales directly with the orbital density along $\boldsymbol{E}$. For L-edges the transition intensity is zero if the $\boldsymbol{E}$-vector lies along the d orbital *nodal axis*, which is the intersection of two nodal planes (see Fig. 9.19).

9.7.3 Theory of X-ray Natural Linear Dichroism

The "search light effect" follows from a quantum mechanical calculation of the angle dependent transition matrix element which we shall outline now.

In order to facilitate our discussion we shall assume that we are dealing with a nonmagnetic sample. Since XNLD does not depend on spin we can use the same formalism as above but only consider one spin. Inclusion of the other spin would simply give a factor 2 higher intensity. We therefore start with (9.85), written for one spin, and take care of the other spins by a factor of 2. We have,

$$I_\alpha^q = 2\,\mathcal{A}\,\mathcal{R}^2 \sum_{\substack{E_i > E_\mathrm{F} \\ i,\mathbf{k},m}} \left| \sum_{p,M} a_{i,M}(\mathbf{k})\; e_{\alpha,p}^q \,\langle LM|C_p^{(1)}|c\,m\rangle \right|^2 . \tag{9.107}$$

This equation is valid for an atom in a solid described by a band-like valence electron wavefunction

$$\begin{aligned} |\psi_i(\mathbf{k},r)\rangle &= |R_{n',L}(r)\rangle\,|\phi_i(\mathbf{k})\rangle \\ &= |R_{n',L}(r)\rangle \sum_M a_{i,M}(\mathbf{k})\,|L\,M\rangle\ . \end{aligned} \tag{9.108}$$

There are $2L+1$ such states for a given L-manifold. If we drop the $\boldsymbol{k}$ dependence, the state (9.108) also describes a ligand field state. For the d orbitals,

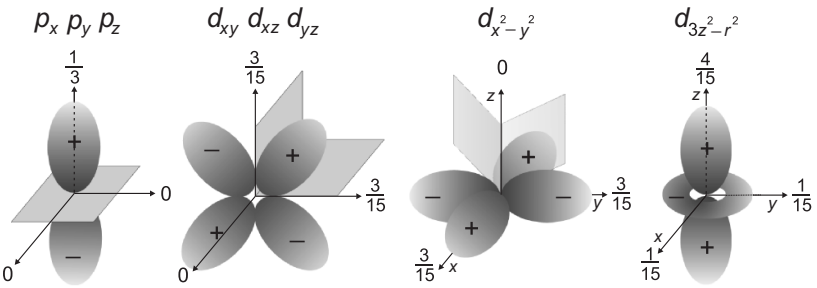

Fig. 9.19. Polarization dependent core to valance transition intensities (square of the transition matrix elements) for $\boldsymbol{E}$ along the principal coordinate axes. Listed are the intensities for the four basic symmetry cases, $s \to p_i$ $(i = x, y, z)$, $p \to d_{ij}$ $(i \neq j = x, y, z)$, $p \to d_{x^2-y^2}$ and $p \to d_{3z^2-r^2}$. All intensities are per orbital per spin in units of $\mathcal{AR}^2$

for example, the coefficients $a_{i,M}$ would be the coefficients in Table A.2. Equation (9.107) is valid for transitions from a spherically symmetric core manifold $|c\,m\rangle$ and the sum is over all $2c+1$ orbital substates. In the measurement of XNLD we therefore assume that we sum over any spin–orbit split states in the core. This is automatically fulfilled for K-edge spectra, and for L-edge spectra we add the L_3 and L_2 intensities. Because in XNLD one wants to learn about the anisotropy of the valence charge around the absorbing atom one best uses linearly polarized light since the directional $\boldsymbol{E}$-vector acts like a search light, as discussed later. We shall therefore restrict our discussion to linearly polarized X-rays.

The search light effect is most clearly seen by considering transitions from a core manifold to specific molecular orbitals. Results for the squared transition matrix elements are summarized in Fig. 9.19. In particular, we list the polarization-dependent transition intensities

$$|\langle 2p_n|\frac{P_\alpha^0}{r}|1s\rangle|^2 \tag{9.109}$$

from a s core state to the p_x, p_y, and p_z valence orbitals, assuming linearly polarized light with $\boldsymbol{E} \parallel x, y, z$, and similarly the intensities

$$|\langle 3d_n|\frac{P_\alpha^0}{r}|2p\rangle|^2 \tag{9.110}$$

from a p core state to the five d_n orbitals, assuming linearly polarized light with $\boldsymbol{E} \parallel x, y, z$.

For all $s \to p_i$, $(i = x, y, z)$ transitions (e.g., K-edge) we have a transition intensity 1/3 when the $\boldsymbol{E}$-vector is along the p_i orbital lobe and zero otherwise. The polarization averaged intensity per p_i orbital is $\langle I\rangle = 1/9$. For all transitions from p core states to the clover-leaf-shaped d orbitals, shown in

the middle of Fig. 9.19, we have a transition intensity 3/15 for $\boldsymbol{E}$ along the two axes that lie in the plane of the orbital and zero along the perpendicular nodal direction. The transition intensity to the $d_{3z^2-r^2}$ orbital is different as illustrated in Fig. 9.19. For $p \rightarrow d_i$ transitions (e.g., L-edge) we have the polarization-averaged intensity per d_i orbital $\langle I \rangle = 2/15$.

In practice, one often encounters the case where the sample has cylindrical symmetry about an axis. Let us consider a nonmagnetic system with cylindrical symmetry about z. For $\boldsymbol{E}$ along z the X-ray absorption intensity for a transition between states $|a\rangle$ and $|b\rangle$ is obtained with the dipole operator P_z^0 in Table A.4 as,

$$I_z^0 = \mathcal{A}\,\mathcal{R}^2 \left| \langle b|C_0^{(1)}|a\rangle \right|^2 . \tag{9.111}$$

Similarly we obtain the intensities for $\boldsymbol{E}$ along x and y as

$$I_x^0 = I_y^0 = \frac{1}{2}\mathcal{A}\,\mathcal{R}^2 \left[\left| \langle b|C_{-1}^{(1)}|a\rangle \right|^2 + \left| \langle b|C_1^{(1)}|a\rangle \right|^2 \right] . \tag{9.112}$$

The cross terms vanish because only one of the operators $C_q^{(1)}$ couples a given pair of substates $|cm\rangle$ and $|LM\rangle$ with $L = c + 1$ and $M - m = q = 0, \pm 1$, according to the dipole selection rule. For later reference it is important to state that one obtains the same intensity as in (9.112) for circularly or natural light incident along z (operators $P_z^{\pm}$ in Table A.4), i.e.,

$$I_z^{+1} = I_z^{-1} = \frac{1}{2}\mathcal{A}\,\mathcal{R}^2 \left[\left| \langle b|C_{-1}^{(1)}|a\rangle \right|^2 + \left| \langle b|C_1^{(1)}|a\rangle \right|^2 \right] . \tag{9.113}$$

For a spherically symmetric charge distribution we have $I_\alpha^q = I_{\alpha'}^q = I_\alpha^{q'}$.

The Angle-Dependent XNLD Intensity

More generally, the measured intensity can be written as a function of the angle θ of the $\boldsymbol{E}$-vector with the symmetry axis (labeled $\|$) and the intensity has the form [388]

$$I(\theta) = I_\| \cos^2\theta + I_\perp \sin^2\theta \; . \tag{9.114}$$

This expression is valid for higher than three fold symmetry about the axis labeled $\|$. The intensities $I_\|$ and $I_\perp$ are determined by the projection of the charge distribution along the symmetry axis and a direction perpendicular to it.[13] If the charge distribution has a node perpendicular to the symmetry axis, we have $I_\perp = 0$, and the linear dichroism intensity has the famous cosine squared polarization dependence.

[13] The charge distribution function itself cannot be determined by XNLD but only its projections along the cartesian coordinate axes. The projections $f_\| = I_\|/(I_\| + 2I_\perp)$ and $f_\perp = I_\perp/(I_\| + 2I_\perp)$ are called *orientation factors* [388].

For a uniaxially aligned system the *X-ray linear dichroism intensity* varies as

$$I(\theta) = I_{\parallel} \cos^2\theta = 3\langle I\rangle \cos^2\theta, \tag{9.115}$$

where θ is the angle of the $\boldsymbol{E}$-vector with the symmetry axis and $\langle I\rangle$ is the angle averaged intensity (9.103).

9.7.4 XNLD and Quadrupole Moment of the Charge

We have seen that polarized X-ray absorption spectroscopy can probe the local anisotropy of the charge density, in particular the hole density, around the absorbing atom. Because the core shell is so localized, XNLD is very sensitive to deviations of the local valence charge in the atomic volume from spherical symmetry. In a picture based on the search light effect the measured X-ray absorption intensity is proportional to the projection of the number of holes in the direction of $\boldsymbol{E}$. By measuring X-ray absorption along three orthogonal directions, i.e., $\boldsymbol{E} \parallel x, y, z$, we can determine the projection of the number of holes along the three directions, as illustrated in Fig. 9.19.

Sometimes it is useful to describe the origin of polarization dependent X-ray absorption in another way. Starting from the fact that the polarization-averaged intensity is a constant according to (9.103), i.e.,

$$\langle I\rangle = C\, N_{\mathrm{h}}, \tag{9.116}$$

one may write the intensity for a given direction α as a deviation from the constant. For a given polarization direction, say along z, we write $I_z = \langle I\rangle - f(z^2)$. The general formalism given in Appendix A.8 yields the expression

$$\boxed{I^0_\alpha = CN_{\mathrm{h}}\,(\,1\,-\,\mathcal{B}\,\langle Q_{\alpha\alpha}\rangle)}\,, \tag{9.117}$$

where $\langle Q_{\alpha\alpha}\rangle$ is the quadrupole moment of the charge distribution. The other factors are

$$C = \mathcal{A}\,\mathcal{R}^2\,\frac{L}{3(2L+1)}\,, \qquad \mathcal{B} = \frac{2L+3}{2L}\,, \tag{9.118}$$

with $\mathcal{A} = 4\pi^2\,\hbar\omega\,(e^2/4\pi\epsilon_0\hbar c)$ and $\mathcal{R}$ being the radial transition matrix element. One can make the following general statement.

The *angle-dependent XNLD intensity* is proportional to the sum of the total number of valence holes and the quadrupole moment of the spatial hole density.

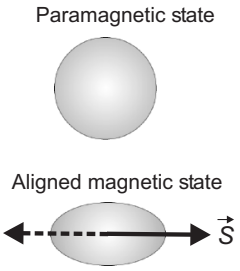

Fig. 9.20. Illustration how a spherical charge density may be modified in the presence of a magnetic alignment of the spins in the sample. The charge distortion arises from the spin–orbit coupling and an asymmetry is induced relative to the spin axis (not direction!). The effect exists in both collinear ferromagnets and antiferromagnets

This formalism appears rather complicated but it is very powerful. We shall see later that it also describes the angle dependent XMCD intensity for the important $3d$ transition metals. In that case the isotropic term proportional to N_h in (9.117) is replaced by the isotropic spin moment m_s and the quadrupolar charge distribution by a quadrupolar spin distribution.[14]

9.7.5 X-ray Magnetic Linear Dichroism

In order to differentiate *magnetic* from *natural* linear dichroism let us assume a sample of cubic symmetry where no XNLD is present. We also assume that the sample becomes magnetically aligned, either ferromagnetic or antiferromagnetic, below the magnetic transition temperature. In the paramagnetic state above the transition temperature the core and valence charge density is then spherically symmetric according to Sect. 9.7.2. As the sample is cooled into a magnetic state with collinear spin alignment, the spin–orbit coupling may lead to a deformation of the charge. This charge distortion is of uniaxial symmetry about the spin direction as shown schematically in Fig. 9.20. Now the X-ray absorption intensity will be different for $\boldsymbol{E}$ aligned *parallel* and *perpendicular* to the spin direction.

> The *XMLD effect* arises from a nonspherical distortion of the atomic charge by the spin–orbit interaction when the *atomic spins* are axially aligned by the exchange interaction.

In order to illustrate the effect of the spin–orbit coupling on the charge density we plot in Fig. 9.21 the charge densities of the individual $|j, m_j\rangle$ components of the spin–orbit split $p_{1/2}$ and $p_{3/2}$ manifolds. This is readily done by use of the wavefunctions listed in Table A.2. We see that all individual densities (squares of wavefunctions) are anisotropic in space relative to the z alignment axis of the spin. In contrast, the sum over all m_j substates of each j manifold are spherically symmetric. We can therefore conclude that a linear *magnetic* dichroism effect will only exist if somehow the m_j substates in

[14] The latter term is the infamous T_z term derived by Carra et al. [101].

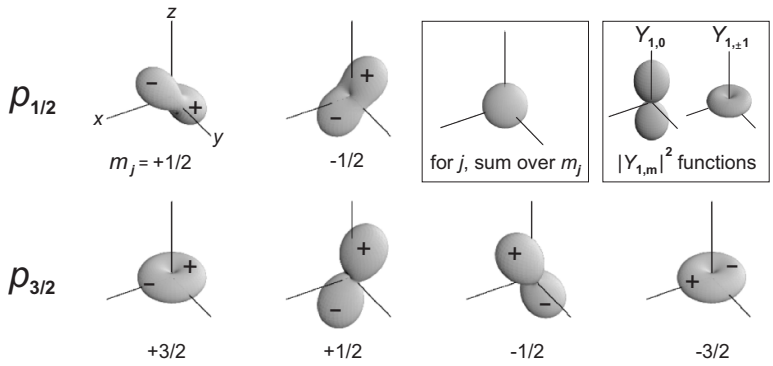

Fig. 9.21. Orbital densities for the $p_{1/2}$ and $p_{3/2}$ manifolds calculated with the functions given in Table A.5. The substates $|l, s, j, m_j\rangle$, for $j = 1/2$ and $j = 3/2$ are labelled for brevity by the quantum numbers m_j. In all cases the spin quantization axis is taken to be the z axis. The charge distributions are seen to be asymmetric in space and they give rise to different X-ray absorption intensities when the $\boldsymbol{E}$-vector is aligned along z and perpendicular to z. One inset shows the spherically symmetric charge density obtained when summing over all m_j states and also when for a given j the m_j states are summed. The upper right inset shows a plot of the charge density $|Y_{l,m}|^2$ for $l = 1, m = 0, \pm1$, associated with the spherical harmonic basis functions for the p states. They are important when the $|j, m_j\rangle$ states are expressed as a function of spin-up and spin-down functions as given in Table A.5

either the initial or final states of the electronic transition are split and do not contribute equally to the X-ray absorption intensity. In magnetic materials a splitting between m_j substates in the valence and core shells naturally arises in the presence of the exchange interaction below the magnetic transition temperature, as discussed in Sect. 6.6.2.

An unequal spectral contribution of such energetically split m_j substates may arise via two effects. First, if at low temperature the substates have an unequal population [389]. Second, if the energetic splitting between the substates can be observed experimentally.

The XMLD effect for the *ferromagnetic transition metals* predominantly arises from the second mechanism, as shown by Kuneš and Oppeneer [390]. We shall discuss their model in Sect. 9.7.6.

9.7.6 Simple Theory of X-ray Magnetic Linear Dichroism

The XMLD model of Kuneš and Oppeneer [390] is illustrated in Fig. 9.22.

To illustrate the origin of the XMLD effect for the 3*d* transition metals we start with a Stoner-like band model as previously used for the explanation of the XMCD effect in Fig. 9.13. Again we simplify the description of the *d* states in an atomic model assuming that the ("down") majority spins are filled. We

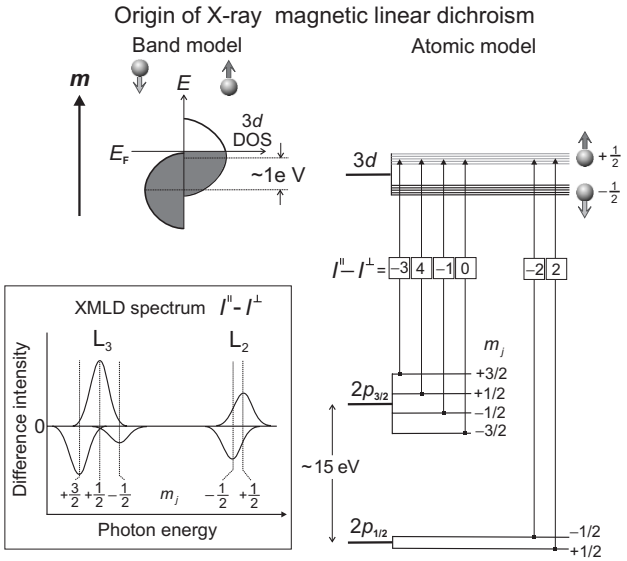

Fig. 9.22. Illustration of the L-edge X-ray absorption processes of linearly polarized photons with angular momentum $q = \pm 1$. For the d valence shell we show the correspondence between the Stoner band picture of a magnetic material and an atomic one-hole d shell model. We have chosen our magnetization direction such that the "down-spins" are filled and the "up-spins" partially unfilled. In the atomic model we assume one "spin-up" hole and show the possible $2p$ core to $3d$ valence transitions assuming circularly polarized light with angular momentum q. The fraction of "up-spin" electrons excited from the p core shell through absorption of X-rays with angular momentum $q = \pm 1$ is listed for the L_3 and L_2 edges. Here we have assumed the X-rays to be incident parallel to the atomic magnetic moment $\boldsymbol{m}$. We have assumed a splitting of the p states by the exchange interaction, lifting the degeneracy in m_j. Note that this causes an opposite order of m_j states for $p_{3/2}$, $l+s$ and $p_{1/2}$, $l-s$ because of the opposite sign of s. Listed are the relative difference intensities which can be obtained from Fig. 9.14 according to $I^{\parallel} - I^{\perp} = I^0 - (I^+ + I^-)/2$. The absolute difference intensities in units of $\mathcal{AR}^2$ are obtained by dividing the listed values by a factor of 90

then consider electronic transitions from the spin–orbit split p core states to the d minority spin states, as shown in Fig. 9.22. From our earlier discussion we know that a magnetic linear dichroism can only exist if we can differentiate transitions between states that are not spherically symmetric.

In our simple model we assume that the empty $3d$ density of minority spin states is spherically symmetric, so that we describe the d shell simply by an equal weighting of all spin-up d_i orbitals. Our assumption is reasonable for band-like systems with cubic symmetry like Fe and Ni where an effec-

tive averaging of the $\boldsymbol{k}$-dependent states over the Brillouin zone leads to an equal contribution of the d_i orbitals. In addition the spin–orbit interaction in the $3d$ valence shell is small ($\sim 50\,\mathrm{meV}$) compared to the exchange interaction (1–2 eV) and for the moment we shall neglect it altogether. We shall see later that the spin–orbit interaction in the valence shell actually leads to the distinction of two kinds of magnetic linear dichroism.

From Fig. 9.21 we know that the total $2p$ core state is also spherically symmetric, and so are the two individual spin–orbit components $2p_{3/2}$ and $2p_{1/2}$. However, the charge density of the individual m_j substates are *anisotropic*. Indeed, in a ferromagnet the exchange field (which only acts on the spin) leads to a small exchange splitting of the m_j substates of the $2p_{3/2}$ and $2p_{1/2}$ states, as discussed in Sect. 6.6.2 and shown in Fig. 9.22. For the $3d$ metals the splitting between the individual m_j states is rather small, of order 0.2 eV [390–392]. The spin enters in our model since only spin-conserving core-to-valence transitions are allowed by the dipole transition operator.[15]

The XMLD difference intensity is obtained from two measurements with $\boldsymbol{E}$-vector parallel and perpendicular to the sample magnetization direction $\boldsymbol{M}$,

$$\Delta I_{\mathrm{XMLD}} = I^{\parallel} - I^{\perp}. \tag{9.119}$$

A simple atomic-like model calculation which is similar to that carried out in conjunction with Fig. 9.14, shows that an XMLD effect exists for the various individual transition intensities as illustrated in Fig. 9.22. The XMLD difference spectrum then consists of the sum of all the individual difference intensities. Assuming magnetic alignment along the z-axis, the energy dependent XMLD difference intensity is given by the difference of the intensities measured for $\boldsymbol{E} \parallel z$ and $\boldsymbol{E} \perp z$. With the dipole operators in Table A.4 we obtain for example, for $\boldsymbol{E}$ along z and x,

$$\begin{aligned}\Delta I_{\mathrm{XMCD}} = \mathcal{A}\mathcal{R}^2 \sum_{n,j,m_j} & \left| \langle d_n, \chi^+ | C_0^{(1)} | p_j, m_j \rangle \right|^2 \\ & - \frac{1}{2} \left| \langle d_n, \chi^+ | C_{-1}^{(1)} - C_{+1}^{(1)} | p_j, m_j \rangle \right|^2 . \end{aligned} \tag{9.120}$$

The cross terms can be shown to vanish and by use of the short form (9.101) we obtain the following expression for the *XMLD difference intensity*,

$$\Delta I_{\mathrm{XMLD}} = \frac{1}{2} \mathcal{A}\mathcal{R}^2 \sum_{\mathrm{states}} 2|\langle C_0^{(1)} \rangle|^2 - |\langle C_{-1}^{(1)} \rangle|^2 - |\langle C_{+1}^{(1)} \rangle|^2 \, . \tag{9.121}$$

[15] The effective charge asymmetry that enters into the transition matrix element is actually not that of the j, m_j core functions but that of their spherical harmonic components. This comes about because the dipole operator only links the minority (up-spin) projections of the p functions given by $Y_{1,m}\chi^+$ (see Table A.5) to the minority d valence states of the form $Y_{2,M}\chi^+$. However, the "spherical" harmonics $Y_{1,m}$ with $m = -1, 0, +1$ are actually very anisotropic as shown in the upper right inset of Fig. 9.21 (also see Table A.2).

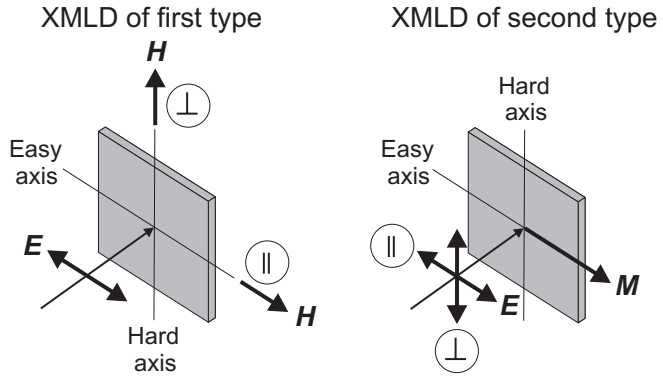

Fig. 9.23. The two methods to record XMLD spectra, called XMLD of the first and second kind. XMLD of the *first kind* is measured with a fixed sample orientation relative to the linearly polarized X-rays, and the magnetization of the sample is rotated between the easy and the hard directions by a sufficiently strong magnetic field. The measured effect is a pure magnetic effect. XMLD of the *second kind* corresponds to saturating the sample along the easy axis and measuring the absorption with the easy axis either parallel or perpendicular to the $\boldsymbol{E}$-vector. This can be done either by rotating the $\boldsymbol{E}$-vector relative to the sample, as shown, or the sample relative to the $\boldsymbol{E}$-vector. In all cases shown the measured intensities are labeled $\parallel$ and $\perp$, as shown, with the XMLD signal defined by (9.119)

We shall come back to this expression later in conjunction with the resonant magnetic scattering intensity in Sect. 9.8.

9.7.7 XMLD of the First and Second Kind

In the above discussion we have assumed that we have a sample of cubic symmetry that is magnetically aligned. The assumption of cubic symmetry eliminates any XNLD effect. This would also be true for a polycrystalline sample. In such cases the linear dichroism signal will only be due to a magnetic effect, namely the charge deformation about the magnetic axis. In single crystal samples with lower than cubic symmetry both XNLD and XMLD effects can be present. The expressions for the general case when both natural and magnetic dichroism effects are present are more complicated and have been discussed by Carra et al. [378].

In principle we can eliminate any XNLD effect by performing a different type of measurement as illustrated in Fig. 9.23. The two depicted types of measurements explained in the figure caption are often referred to XMLD of the *first* and *second* type, following Guo et al. [380].

Although experimentally more demanding, the XMLD effect of the first kind has the advantage that it eliminates the XNLD effect.[16] It also contains useful information on the magnetocrystalline anisotropy (MCA) as discussed below. If the MCA of the sample is negligible and the sample has either cubic symmetry or is polycrystalline the two types of XMLD measurements give the same result. For example, polycrystalline films of the elemental ferromagnets typically have an in-plane easy axis and a weak in-plane anisotropy. In lowest order it then does not matter whether we measure the XMLD effect by either rotating the magnetization direction $\boldsymbol{M}$ with a field relative to the fixed $\boldsymbol{E}$-vector or whether we rotate $\boldsymbol{E}$ relative to the fixed magnetization $\boldsymbol{M}$. Therefore, our theory developed above should describe the experimental XMLD spectra.

The lineshape predicted by our simple model is indeed observed as shown in Fig. 9.24 [393, 394]. The measurements actually correspond to the XMLD effect of the first kind.[17] The size of the XMLD effect plotted in Fig. 9.24 corresponds to a per-atom normalization of the original spectra, with the edge jump set to unity. The XMLD difference intensity is seen to be significantly smaller than the corresponding XMCD effect in Fig. 9.12. This confirms the expectations from our model calculation.

Despite the larger linewidth ($\sim$1 eV) of the individual transitions than the core exchange splitting ($\sim$0.2 eV) the small energy shifts of the individual components still have a pronounced effect on the measured XMLD *line shape*. As shown in the bottom left inset of Fig. 9.22, the small energetic shifts of the individual transitions leads to a pronounced differential resonance line shape at both the L_3 and L_2. It arises from shifted positive and negative components which, when added, give a similar differential lineshape from negative to positive intensity for both edges. The same lineshape at the two edges is a consequence of the fact that for the $p_{3/2}$, $(l + s)$ and $p_{1/2}$, $(l - s)$ levels the signs of both s and m_j are inverted as discussed already in Sect. 6.6.2 in conjunction with Fig. 6.18. The intensity of the largest peak in the XMLD (difference) spectrum in the inset of Fig. 9.22 is $(4/90)\mathcal{AR}^2$. This compares to the value $(2/9)\mathcal{AR}^2$ for the XMCD difference, given by (9.96) or (9.97), and indicates that the XMLD effect should be considerably smaller than the XMCD effect. XMLD spectra can also be measured by analyzing the polarization of the X-rays rather than measurement of the absorption. Such magneto-optical polarization spectroscopy, discussed in Sect. 8.7.4, can be performed in several different geometries [395], and is complementary to X-ray absorption spectroscopy.

[16] In *antiferromagnets* one can, in principle also "flop" the magnetization axis from the easy into the hard direction, but typically very large fields are required.

[17] Note that the geometry used in reference [393] is opposite to the one shown in Fig. 9.23 and therefore the measured difference denoted $\alpha^{\perp} - \alpha^{\parallel}$ by the authors actually agrees with our definition in (9.119).

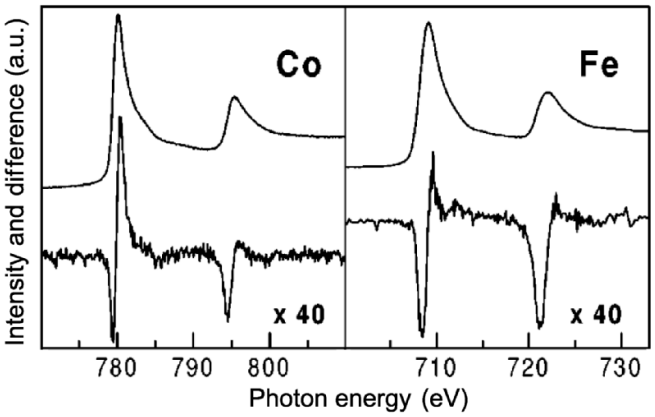

Fig. 9.24. X-ray absorption spectra and XMLD difference spectra for Co and Fe metal [393]. The plotted intensities of the difference spectra correspond to $I^{\parallel} - I^{\perp}$, with the original spectra normalized to an edge jump of 1, far above the edges. The measurements actually correspond to XMLD of the first kind, but because of the weak magnetocrystalline anisotropy and the polycrystalline nature of the samples, the difference between spectra of the first and second kind is negligibly small

XMLD of the first kind, which is measured by fixing the X-ray polarization vector $\boldsymbol{E}$ along either the hard axis or easy axis and then rotating the magnetic axis by 90° using a sufficiently strong external magnetic field, avoids any natural linear dichroism contribution because only the magnetically induced change in charge distribution is measured. In addition, we know from Sect. 7.9.3 that the energy associated with the rotation of the magnetic axis is the magnetocrystalline anisotropy ΔE_{so}. It is therefore not surprising that XMLD measurements of the first kind can indeed measure the magnetocrystalline anisotropy. This was first pointed out by van der Laan [396] who also established a sum rule that links the magnetocrystalline anisotropy with a linear combination of the XMLD intensity measured at the L_3 and L_2 edges, according to

$$\frac{\Delta I_{\mathrm{L}_3} - 2\Delta I_{\mathrm{L}_2}}{\langle I_{\mathrm{L}_3} + I_{\mathrm{L}_2} \rangle} = \frac{16\sqrt{3}}{5\,\zeta_{3d}} \frac{\Delta E_{\mathrm{so}}}{N_{\mathrm{h}}} \ . \tag{9.122}$$

Here ΔE_{so} is the magnetocrystalline anisotropy energy given by (7.50), ζ_{3d} the spin–orbit parameter defined in (6.87), N_{h} is the number of $3d$ holes, and $\langle I_{\mathrm{L}_3} + I_{\mathrm{L}_2} \rangle$ is the white line intensity defined in (9.104). The sum rule was experimentally verified by Dhesi et al. [394].

It is interesting to note that the magnetocrystalline anisotropy energy values derived from XMLD are significantly larger than the energies measured with conventional methods. This is similar to the determination of the magne-

tocrystalline anisotropy energies from the angular dependence of the orbital moment, as discussed in Sect. 7.9.3. The origin for these discrepancies are not understood [333, 394].

Summary for the XMLD Intensity

We can summarize as follows.

> *X-ray magnetic linear dichroism*, XMLD, arises from charge anisotropies induced by the exchange and spin–orbit interactions relative to the easy magnetic *axis* of the sample. The effect arises from *uniaxial* spin alignment and exists for both ferromagnets and antiferromagnets.

In practice, the measured magnitude of the XMLD intensity depends on three important parameters,

- The degree of linear polarization $P_{\rm lin}$
- The expectation value of the square of the magnetic moment $\langle \boldsymbol{m}^2 \rangle$
- The angle θ between the $\boldsymbol{E}$-vector and the magnetic axis

This can be cast into the following general dependence of the XMLD intensity,

$$\boxed{I_{\rm XMLD} \propto P_{\rm lin}\, |\boldsymbol{m} \cdot \boldsymbol{E}|^2 \propto P_{\rm circ}\, \langle \boldsymbol{m}^2 \rangle \cos^2\theta}\,. \tag{9.123}$$

In theory, one calculates the maximum linear dichroism effect by assuming $P_{\rm lin} = 1$ and assuming two perpendicular measurements with $\boldsymbol{E}$ parallel and perpendicular to $\boldsymbol{m}$. In this case one obtains (9.121) for the XMLD difference intensity. We can state as follows.

> The *XMLD difference intensity* for a system with its *magnetic axis along z* may be written in terms of angular matrix elements of the Racah spherical tensors according to,
>
> $$\Delta I_{\rm XMLD} = \frac{\mathcal{A}\mathcal{R}^2}{2} \sum_{\rm states} 2|\langle C_0^{(1)} \rangle|^2 - |\langle C_{-1}^{(1)} \rangle|^2 - |\langle C_{+1}^{(1)} \rangle|^2 \,. \tag{9.124}$$
>
> The factor $\mathcal{A}$ is given by (9.61), and $\mathcal{R}$ is the radial transition matrix element given by (9.81).

It is important to note the difference between the expectation value $\langle \boldsymbol{m}^2 \rangle$ measured by XMLD and the quantity $\langle \boldsymbol{m} \rangle^2$ which can be determined by XMCD [93]. The difference between the two quantities plays an important

role in the temperature dependence of the XMLD intensity [93, 105, 106], as discussed by Regan [284].[18]

9.7.8 Enhanced XMLD through Multiplet Effects

In our discussion above we have used a simple one-electron model which describes the electronic excitation of an "active" electron and ignores its coupling to the other atomic electrons, which are therefore assumed to be "passive". In practice, such a model only works if correlation effects are small. The success of our simple treatment of the XMLD effect in the magnetic transition metals is largely based on the fact that they can be reasonably well described by density functional theory which is largely based on an independent-electron picture as discussed in Chapter 7.

For strongly correlated systems such as the transition metal oxides, we have seen in Chapter 7 that multiplet effects have to be taken into account. In particular we have discussed multiplet effects that arise from the coupling between the electrons within the $3d$ valence shell. Such coupling leads to ${}^{2S+1}L$ ionic terms that are furthermore split by the ligand field and the exchange and spin-orbit interactions. The electronic ground state is the lowest-energy state. For such systems one can no longer describe X-ray absorption in a one-electron model but one needs to use a configuration based approach, as discussed in Sect. 9.5.1.

For $3d$ transition metals, the configuration picture calculates the X-ray absorption spectrum as transitions from the electronic ground to an excited configuration [266, 267, 397, 398]. The electronic ground configuration consists of a filled $2p^6$ core shell and a $3d^N$ shell with N electrons. In the final configuration one electron has been removed from the core shell and added to the $3d$ shell. We have the *electron* excitation scheme,

$$\text{Electron excitation picture:} \qquad 2p^6\, 3d^N \rightarrow 2p^5\, 3d^{N+1}. \tag{9.127}$$

If the $3d$ shell is more than half full it simplifies things to use the concept of holes instead of electrons. This is possible because we have learned in Sect. 6.5 that for a given shell the Coulomb and exchange interactions can be equivalently treated in either an electron or hole picture if we take care of signs. For

[18] The two quantities, $\langle \boldsymbol{m}^2 \rangle$ and $\langle \boldsymbol{m} \rangle^2$ are related by the magnetic susceptibility χ and temperature T according to

$$\frac{\langle \boldsymbol{m}^2 \rangle}{\mu_0} = \frac{\langle \boldsymbol{m} \rangle^2}{\mu_0} + k_\mathrm{B} T \chi. \tag{9.125}$$

If the susceptibility χ is not known one may use a molecular field expression to relate the two expectation values according to [93]

$$\langle \boldsymbol{m}^2 \rangle = g_J^2 \mu_\mathrm{B}^2 J(J+1) - g_J \mu_\mathrm{B} \langle \boldsymbol{m} \rangle \coth\left(\frac{g_J \mu_\mathrm{B} H_\mathrm{ext}}{2 k_\mathrm{B} T} \right). \tag{9.126}$$

example, Hund's third rule states that the spin–orbit interaction changes sign and the LF splitting is upside down as shown in Fig. 7.16. With these rules we can use instead of (9.127) the following *hole* excitation scheme,

$$\text{Hole excitation picture:} \qquad 2p^0\,3d^{10-N} \rightarrow 2p^1\,3d^{9-N}. \tag{9.128}$$

We can state as follows.

> L-edge spectra for multielectron $3d^N$ valence systems may be derived by considering either electron or hole configurations. The two schemes give the same ^{2S+1}L free ion multiplets but the sign of the spin–orbit and LF splittings have to be inverted.

The simplest case involves initial (ground) and final (excited) configurations with only two particles. It is encountered for NiO which has a (predominantly) $2p^6\,3d^8$ ground state and a $2p^5\,3d^9$ excited state configuration. The hole picture involves a $p^0\,d^2 \equiv d^2$ ground and $2p^1\,3d^1 \equiv 2p\,3d$ final configuration. Hence we see that in this case the hole picture is simpler and involves the interactions between two-holes, both in the initial and final configurations. The X-ray absorption spectrum then corresponds to transitions between these two configurations. Let us take a look at the electronic states involved in the corresponding L-edge X-ray absorption spectrum.

The energy states involved in the L-edge transitions for Ni^{2+} in an octahedral ligand field (e.g., NiO) are shown in Fig. 9.25. The electronic ground configuration $2p^63d^8$ ($p^0\,d^2 \equiv d^2$ hole state) consists of a filled $2p$ core shell and 8 electrons in the $3d$ shell which are coupled by the strong Coulomb and exchange interactions (total splitting about $\sim$5 eV), resulting in a ^3F free ion ground state which lies below the next higher states (^1D,^3P) by about 2 eV [266]. The ^3F state is split by the LF as shown in Fig. 7.16 ($10D_q \simeq 1.5$ eV) with a lowest energy $^3A_{2g}$ orbital singlet state with a spin $S = 1$, corresponding to a spin moment of $2\mu_B$ and a quenched orbital moment. From Table 7.7 we see that the $d^8(^3A_{2g}, t_{2g}^6 e_g^2)$ ground state can be thought of as two holes of the same spin in the two e_g orbitals $d_{3z^2-r^2}$ and $d_{x^2-y^2}$. According to Table A.2 these d orbitals correspond to the spherical harmonics $Y_{2,0}$ and $Y_{2,\pm2}$, respectively. Thus the $^3A_{2g}$ state can be written as products of the two one-electron functions $\hat{\boldsymbol{A}}(Y_{2,0}\,Y_{2,\pm2})$, where $\hat{\boldsymbol{A}}$ means that the product has been properly antisymmetrized, i.e., is a Slater determinant. With the angular momentum addition rules $M_L = m_\ell^1 + m_\ell^2$, where $m_\ell^i = 0, \pm1$ are the magnetic quantum numbers of the two electrons, one can then see that the state $^3A_{2g}$ has the form

$$|^3A_{2g}\rangle \sim |\hat{\boldsymbol{A}}(Y_{2,0}\,Y_{2,\pm2})\rangle \sim |^3F, M_L = \pm2, M_S\rangle. \tag{9.129}$$

The $^3A_{2g}$ state is further split by the superexchange interaction. The exchange field felt by the Ni^{2+} ion consists of the sum over the six nearest neighbors [399]

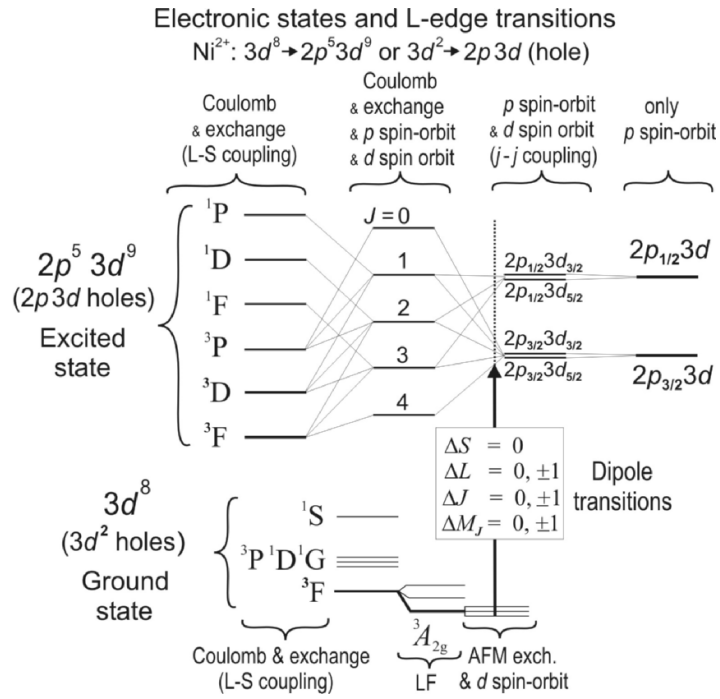

Fig. 9.25. Illustration of the electron states involved in the L-edge transitions for Ni^{2+} in an octahedral ligand field (e.g., NiO) as discussed in the text. The $2p^6\,3d^8$ electronic *ground state* configuration, corresponding to a $2p^0\,3d^2 \equiv 3d^2$ hole configuration, is coupled by the strong Coulomb and exchange interactions to a ^3F free ion ground state which is split in an octahedral LF, resulting in a lowest energy $^3A_{2g}$ ground state. The $2p^5\,3d^9$ electronic *final state* configuration ($2p\,3d$ hole configuration) is dominated by the strong $2p$ core spin–orbit interaction, as shown on the *right*. In practice, the two-hole final states are described by an "intermediate" coupling scheme, indicated by the *dotted vertical line*. These states may be written as linear combinations of $L-S$ coupling (*left*) or $j-j$ coupling states (*second from right*), whose correspondence may be seen by means of the common J states (*second from left*) [182]. We have also listed the dipole selection rules in L–S–J coupling

and is about 0.15 eV. It aligns the atomic moments into an antiferromagnetic arrangement, as shown in Fig. 7.25. Together with the even weaker spin–orbit interaction ($\zeta_{3d} \sim 50$ meV) it leads to a magnetic splitting of the $^3A_{2g}$ state, where the lowest energy state may be written in the form[19]

[19]The $3d$ spin–orbit interaction also mixes the $^3A_{2g}$ LF ground state with the higher energy $^3T_{2g}$ and $^3T_{1g}$ LF states, resulting in a small orbital moment.

$$|\mathrm{GS}\rangle = \sum_{\substack{J=4,3,2 \\ M_J}} a_{J,M_J} |^3F_J, M_J\rangle \ . \tag{9.130}$$

The $2p\,3d$ hole final configuration of the electronic excitation cannot simply be treated in L–S coupling because the largest interaction is the spin–orbit coupling for the $2p$ hole, which leads to a $2p_{3/2} - 2p_{1/2}$ splitting of about 15 eV, and is larger than the $2p\,3d$ Coulomb and exchange interaction ($\sim$5 eV). Hence the final state corresponds to a coupling scheme [182] that is "intermediate" between that where the Coulomb and exchange interaction is turned off, schematically shown on the right side of Fig. 9.25 and the L–S scheme shown on the left side. For reference we also show a j–j coupling scheme, assuming a small spin–orbit interaction in the $3d$ shell. In general, there are n energetically different final states which form two separate spin-orbit split groups and within each group exhibit multiplet structure. They can also be written as linear combinations of $|L, S, J, M_J\rangle$ states according to[20]

$$|\mathrm{FS}\rangle_n = \sum_{\substack{J=4,3,2 \\ M_J}} b^n_{J,M_J} |^3F_J, M_J\rangle + \sum_{\substack{J=3,2,1 \\ M_J}} c^n_{J,M_J} |^3D_J, M_J\rangle \ . \tag{9.131}$$

The fine structure of the L-edge absorption spectrum calculated by van der Laan and Thole [402] for a $3d^8$ electronic ground state and different strengths of the spin–orbit and Coulomb interactions in the $2p^5 3d^9$ final state is shown in Fig. 9.26a. Here the evolution of the spectrum is shown between two extreme cases. If the Coulomb and exchange interactions are zero, the spectrum (top trace) shows one-electron like behavior with two peaks separated by the $2p$ spin–orbit splitting. In the other extreme of zero $2p$ core spin–orbit splitting but strong Coulomb and exchange splitting, the spectrum (bottom trace) is that calculated in pure L–S coupling. It consists of two peaks, corresponding to the allowed ($\Delta S = 0, \Delta L = 0, \pm 1$) transitions ${}^3F \rightarrow {}^3D$ and ${}^3F \rightarrow {}^3F$. In the intermediate region, where both the $2p$ core spin–orbit and $2p$–$3d$ Coulomb and exchange splitting are present, a more complicated L-edge spectrum is found. The situation encountered in practice for Ni^{2+} in octahedral symmetry is indicated by an arrow on the left, and the calculated spectrum is shown in Fig. 9.26b [402]. The agreement with experiment demonstrates the power of multiplet calculations.

The enhancement of the XMLD effect in the presence of multiplet splitting arises from the same physical principle as in the one-electron case. An XMLD effect will only exist if the exchange and spin–orbit interactions break the spherical symmetry in either or both of the initial and final states involved in the electronic transitions. The origin of the magnetically induced charge

[20] In general, one can always express functions written in one coupling scheme as a linear combination of functions written in another coupling scheme. In practice, this is done today by use of the elegant scheme developed by Racah [400] and Wigner [401], which is treated in detail by Cowan [182] and Shore and Menzel [181].

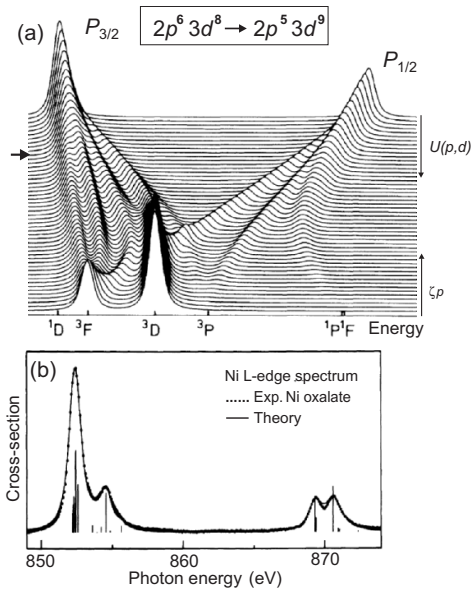

Fig. 9.26. (**a**) Calculated L-edge transition probability from a $2p^6\,3d^8$ configuration with a ^3F free ion ground state to the $2p^5\,3d^9$ electronic *final state* configuration [402]. The horizontal scale corresponds to excitation energy, while the $2p$–$3d$ Coulomb and exchange interaction $U(p,d)$ and the $2p$ spin–orbit coupling ζ_p are varied vertically. The top trace correspond to pure $2p$ spin–orbit coupling ($U(p,d)=0$) and the lowest trace to pure L–S coupling ($\zeta_p = 0$). The case corresponding to experiment is marked with an *arrow* on the *left side*. (**b**) Experimental (*dotted line*) and calculated L-edge spectra (*data points*) for Ni oxalate [402]

asymmetry in the ground state (9.130) and the excited states (9.131) is best seen by realizing that any multiplet state $|^{2S+1}L_J\rangle = |L,S,J\rangle$ is spherically symmetric, similar to the one-electron case shown in Fig. 9.21. Only when the M_J-degeneracy is lifted through magnetic interactions do the $|L,S,J,M_J\rangle$ substates exhibit a charge asymmetry.

Both the ground state (9.130) and the excited states (9.131) are seen to consist of a linear combination of M_J substates, weighted by coefficients a_{J,M_J}, b^n_{J,M_J}, and c^n_{J,M_J} and are therefore, in general, not spherically symmetric. In addition, the dipole operator couples the M_J-states in the ground state and the M'_J states in the excited states differently for linearly polarized light along z, namely $M'_J - M_J = 0$, and for linearly polarized light perpendicular to z, namely $M'_J - M_J = \pm 1$. One may summarize the reasons for the enhanced XMLD effect in spectra with multiplet effects as follows.

The *XMLD effect is enhanced in the presence of multiplet effects* for the following reasons:

- The X-ray absorption spectrum for a sample with a $2p^6 3d^N$, $1 < N < 9$, ground configuration consists of several resonances that are due to the multiplet structure of the final configuration $2p^5 3d^{N+1}$.
- In general, for magnetically aligned samples both the electronic ground state of the $2p^6 3d^N$ ground configuration and the excited states of the final configuration $2p^5 3d^{N+1}$ are not spherically symmetric.
- The dipole operator selects and weights the various resonant transitions depending on the light polarization, often with opposite intensity changes for energetically separated resonances.

The XMLD effect measured for a thin epitaxial NiO film grown on MgO(100) is shown in Fig. 9.27 [403]. In this case the XMLD effect arises from the preferential alignment of the antiferromagnetically coupled spins perpendicular to the film surface. In comparison, the results of a multiplet

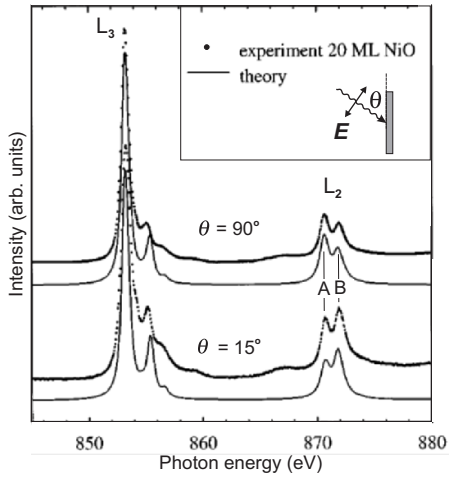

Fig. 9.27. Experimental (*dotted line*) polarization dependent Ni L-edge spectra for a 20 monolayer (ML) thick epitaxial NiO(100) film grown on MgO(100) [403], measured at room temperature. The angle $\theta = 90°$ corresponds to normal incidence with $\boldsymbol{E}$ in the plane of the film and $\theta = 15°$ to grazing incidence with $\boldsymbol{E}$ nearly along the surface normal. The theoretical spectra (*solid line*) were calculated with a multiplet theory including an octahedral LF and assuming an exchange interaction along a magnetic axis that lies nearly perpendicular to the surface along $\langle \pm 2 \pm 1 \pm 1 \rangle$

calculation are also shown. They are found to be in good agreement with the data. Particularly important is the strong change of the two peaks A and B associated with the L_2-edge. By comparison of experiment and theory one can establish the following rule: when the $\boldsymbol{E}$-vector is aligned along the magnetic axis the higher energy peak B has maximum intensity. The peak intensity ratio is often used to determine changes in the orientation of the magnetic axis [105, 403–405].

The magnetic origin of the observed linear dichroism effect may be proven by heating the sample above the Curie temperature, as illustrated for strontium doped $LaFeO_3$ in Fig. 9.28. If about 40% of the La atoms are replaced by Sr, the high Néel temperature of $LaFeO_3$ (1013 K) is reduced to around 200 K. The Fe $L_{2,3}$ NEXAFS spectra of such a $La_{0.6}Sr_{0.4}FeO_3$ sample recorded below and above the Néel temperature are plotted in Fig. 9.28a, b, respectively. The spectra recorded at 100 K, well below the expected Néel temperature, reveal the presence of a strong polarization dependence, which completely vanishes in case of the room temperature spectra. This clearly demonstrates the purely magnetic origin of the linear dichroism observed for $La_{0.6}Sr_{0.4}FeO_3$ below its Néel temperature.

Both $LaFeO_3$ (see Fig. 10.9) and $La_{0.6}Sr_{0.4}FeO_3$ have the same crystal structure with six oxygen atoms surrounding each Fe atom. Since the oxygens have a higher electronegativity than Fe, $LaFeO_3$ is an ionic compound in which Fe has a valency of 3+ and a d^5 high spin ground state. Correspondingly, the rich fine structure of the spectra can be explained by a multiplet calculation performed for an Fe^{3+} ion in a high-spin ground state [407], which considers the multiplet coupling of the five Fe $3d$ valence electrons (or holes) in the ground state, and the multiplet coupling of the four $3d$ holes and the $2p$ core hole in the final state. The oxygen ligands surrounding the Fe^{3+} ion give rise to an octahedral crystal field, which is taken into account via the cubic $10Dq$ crystal field parameter. In general, more than one multiplet state contributes to each of the peaks in the absorption spectrum. Since these different states typically differ in their polarization dependence, the intensities of the absorption structures typically vary between two finite extreme values and do not vanish completely for any orientation of the electric field vector relative to the AFM axis.

9.7.9 The Orientation-Dependent Sum Rules

In Sect. 9.6.5 we established relationships between orientation-averaged X-ray absorption resonance intensities and physical quantities which represent averages over the atomic volume, like the number of valence holes per atom and the atomic spin and orbital moments. It turns out that these orientation averaged sum rules are integrated versions of more general orientation-dependent sum rules. The latter link the intensities of orientation-dependent XNLD, XMLD, and XMCD spectra to the same atomic-volume integrated physical quantities plus an orientation-dependent term related to the quadru-

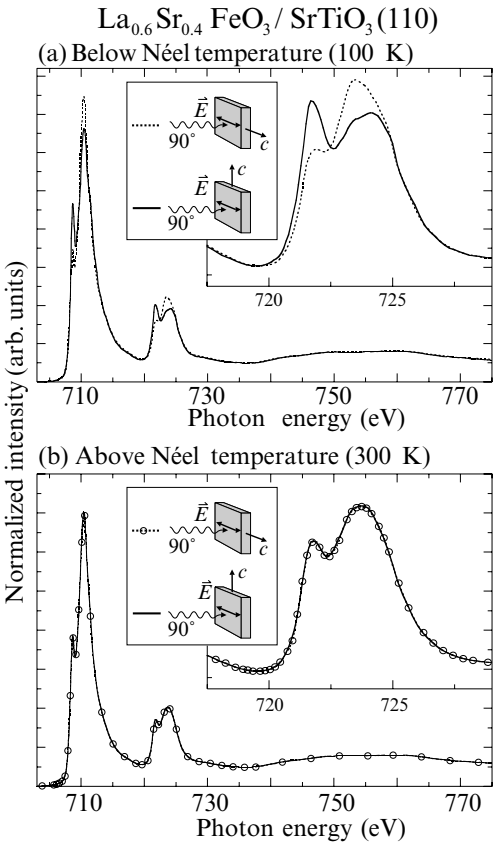

Fig. 9.28. Saturation corrected electron yield spectra at the Fe $L_{2,3}$-edge of $La_{0.6}Sr_{0.4}FeO_3$, grown as a 40 nm thin $La_{0.4}Sr_{0.6}FeO_3$ film on a $SrTiO_3(110)$ substrate, for the two indicated geometries, (**a**) below and (**b**) above the Néel temperature. The absence of any dichroism above the Néel temperature demonstrates the magnetic origin of the linear dichroism effect observed below the Néel temperature. Spectra taken from Lüning et al. [406]

pole moment. The orientation-dependent term simply integrates to zero when an orientational average is performed.

In the context of this book we restrict our discussion to the generalized form of three sum rules of Sect. 9.6.5. In particular, we simply state their form since a more detailed discussion has been given elsewhere [102, 333, 384, 408]. Also, there are other sum rules for the case of XMLD, and we refer the interested reader to the original papers [378, 382, 383].

When generalized, the *charge sum rule* (9.103) takes the form (9.117) or A.31 which we can write in simplified form as (see Appendix A.8),

$$[\,I_{\mathrm{L}_3} + I_{\mathrm{L}_2}]_\alpha = C(N_\mathrm{h} + N_Q^\alpha). \tag{9.132}$$

We have characterized the anisotropy by an index α that specifies the orientation of $\boldsymbol{E}$ (linear polarization) or $\boldsymbol{k}$ (circular polarization). The sum rule correlates the polarization dependent white line intensity with the total number of d holes N_h and a quadrupole term N_Q^α which expresses the anisotropy of the charge density in the atomic volume as discussed in Sect. 9.7.4 and Appendix A.8. The term N_Q^α vanishes when an angular average is performed, $\sum_\alpha N_Q^\alpha = N_Q^x + N_Q^y + N_Q^z = 0$ yielding the isotropic sum rule (9.103).

For $3d$ compounds the *spin sum rule* (9.105) originally derived by Carra et al. [101] takes the general form [102, 408]

$$[-A + 2B]_\alpha = \frac{C}{\mu_\mathrm{B}}(m_s + m_D^\alpha)\ . \tag{9.133}$$

We see that its form closely resembles the charge sum rule, and in fact its derivation in a one-electron model proceeds along the same lines as that of (9.132). In general, the term m_D^α arises from the anisotropic spin density in the atomic volume. It is given by $m_D^\alpha = -7\langle T_\alpha\rangle\mu_\mathrm{B}/\hbar$ [408] where $\boldsymbol{T} = \boldsymbol{S} - 3\hat{\boldsymbol{r}}(\hat{\boldsymbol{r}}\cdot\boldsymbol{S})$ is the intra-atomic magnetic dipole operator [101]. In general we have $T_\alpha = \sum_\beta Q_{\alpha\beta}S_\beta$, so that the charge (expressed by the quadruple operator Q, see Appendix A.8) and spin (S) components of T are coupled. If the atomic spin–orbit coupling is comparable to the ligand field effects experienced by the magnetic atom, the charge distribution is no longer decoupled from the spin distribution and in this case the term m_D^α is always present in addition to the spin moment. This provides a problem since the spin moment cannot be independently determined. We shall not discuss this difficult case here but refer the reader to references [409–411].

If the spin–orbit coupling is weak relative to the ligand field effects, the atomic spin density closely follows the atomic charge density. The term m_D^α is then mainly determined by the anisotropy of the charge due to bonding and it may be eliminated by three orthogonal measurements, provided the ligand field symmetry is not too low [102, 333].

Many $3d$ compounds fall in this category since the spin–orbit coupling is small. In this case there is more than a formal similarity between the charge sum rule (9.132) and the spin sum rule (9.133). In this case the total number of holes, N_h, and the charge density term, N_Q^α in (9.132), are simply replaced by the isotropic spin moment, m_s, and a spin density term $m_D^\alpha = (7/2)\sum_i Q_\alpha^i m_s^i$ in (9.133), respectively. The latter consists of a sum over the d_i-orbital projected spin moments m_s^i and the quadrupole matrix elements Q_α^i of the d_i-orbitals defined in (A.32). This term is nonzero in anisotropic bonding environments and reflects the fact that the number of spins in the atomic volume differs along different crystallographic (bonding) directions. Polarized X-rays

therefore offer the capability of probing the angular distribution of the spins in the atomic volume, whereas conventional magnetometry only probes the integrated number of spins, i.e., the essentially isotropic spin moment per atom. For small spin–orbit coupling, the term m_D^α vanishes when an angular average is performed because of its link to the quadrupole moment. We then have $(1/3)\sum_\alpha m_D^\alpha = 0$, and the isotropic sum rule (9.105) is obtained. The angular average requires that in all measurements the sample is magnetically saturated by a strong external magnetic field along the X-ray propagation direction.

Finally, we discuss the general *orbital moment sum rule*. When an XMCD measurement is performed for a given sample orientation in the presence of an external magnetic field which is sufficiently large to magnetically saturate the sample along the X-ray propagation direction $\boldsymbol{k}$, the orbital moment m_o^α along the field direction α can be directly determined by use of the sum rule

$$-[\,A+B]_\alpha = \frac{3C}{2\mu_\mathrm{B}}\; m_o^\alpha \;. \tag{9.134}$$

Note that in contrast to the quantities N_h and m_s which by definition correspond to isotropic atomic quantities, the orbital moment m_o^α is in general anisotropic, as discussed in Sect. 7.9.3. We have also seen in that section that the difference between the orbital moments measured along the easy and hard magnetization directions is related to the magnetocrystalline anisotropy.

9.8 Magnetic Dichroism in X-ray Absorption and Scattering

We conclude this chapter by connecting the magnetic dichroism effects observed in X-ray absorption and resonant scattering. We have seen in Sect. 9.4.2 that the X-ray absorption cross-section is given by the imaginary part $f_2(E) = F''(E)$ of the resonant forward scattering factor $F(E)$, according to the optical theorem (9.49) or

$$\sigma^\mathrm{abs}(E) = 2\,r_0\,\lambda\,\mathrm{Im}[F(\boldsymbol{Q},E)]_{\boldsymbol{Q}=0} = \frac{C^*}{E} f_2(E)\;, \tag{9.135}$$

where $C^* = 2\,h\,c\,r_0 = 0.70\times10^8\,\mathrm{b\,eV}$. This general relationship also holds for *dichroic* absorption and scattering. For example, if we measure the XMCD absorption cross-section $\sigma^\mathrm{abs}(E)$ we can use the Kramers–Kronig transformation to obtain the dichroic scattering factors, and by their use we obtain the resonant scattering cross-section in the long-wavelength limit according to (9.48) or

$$\sigma^\mathrm{scat} = \sigma_\mathrm{e}\left([f_1(E)]^2 + [f_2(E)]^2\right). \tag{9.136}$$

As an example we show in Fig. 9.29 the L-edge dichroic absorption and scattering cross-sections for Fe metal, using the data of Kortright and Kim [353].

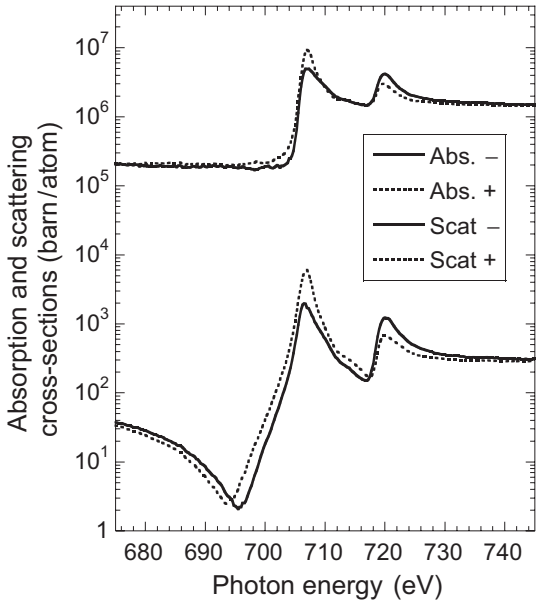

Fig. 9.29. Fe L-edge XMCD cross-sections for the absorbed and elastically scattered intensity [353]. The shown cross-sections are the polarization-dependent versions of those in Fig. 9.6 in the presence of magnetic alignment

The plot is the dichroic version of that in Fig. 9.6. The figure shows that magnetic effects are prominent both in X-ray absorption and resonant scattering.

In Sect. 9.5.3 we have stated the quantum mechanical results for the X-ray absorption cross-section, given by (9.59), and the resonant scattering cross-section in the long-wavelength limit, given by (9.63). We now want to establish the link between these expressions, which in essence constitutes the proof of dichroic version of the optical theorem (9.49).

9.8.1 The Resonant Magnetic Scattering Intensity

We start with expression (9.63) for the differential cross-section for the resonantly scattered intensity in the dipole approximation, i.e.,

$$\left(\frac{\mathrm{d}\,\sigma}{\mathrm{d}\Omega}\right)^{\mathrm{scat}} = r_0^2\,|F(\hbar\omega)|^2 = \frac{\hbar^2\omega^4}{c^2}\;\alpha_{\mathrm{f}}^2\left|\sum_n \frac{\langle a|\boldsymbol{r}\cdot\boldsymbol{\epsilon}_2^*|n\rangle\langle n|\boldsymbol{r}\cdot\boldsymbol{\epsilon}_1|a\rangle}{(\hbar\omega - E_R^n) + \mathrm{i}(\Delta_n/2)}\right|^2 \quad . \tag{9.137}$$

For a magnetic sample, we define the z quantization axis to lie along the magnetization direction. One can then express the double matrix element in terms of matrix elements of spherical tensors $C_q^{(1)}$ $(q = 0, \pm 1)$ and products

involving the unit polarization vectors and the unit vector $\hat{\boldsymbol{m}} = \boldsymbol{e}_z$ according to [412]

$$\begin{aligned}\langle a|\boldsymbol{r}\cdot\boldsymbol{\epsilon}_2^*|n\rangle\langle n|\boldsymbol{r}\cdot\boldsymbol{\epsilon}_1|a\rangle = \frac{\mathcal{R}^2}{2}\big[&(\boldsymbol{\epsilon}_2^*\cdot\boldsymbol{\epsilon}_1)\left\{|C_{+1}|^2+|C_{-1}|^2\right\}\\ &+\mathrm{i}(\boldsymbol{\epsilon}_2^*\times\boldsymbol{\epsilon}_1)\cdot\hat{\boldsymbol{m}}\left\{|C_{-1}|^2-|C_{+1}|^2\right\}\\ &+\ (\boldsymbol{\epsilon}_2^*\cdot\hat{\boldsymbol{m}})(\boldsymbol{\epsilon}_1\cdot\hat{\boldsymbol{m}})\left\{2|C_0|^2-|C_{-1}|^2-|C_{+1}|^2\right\}\big],\end{aligned} \tag{9.138}$$

where $\mathcal{R} = \langle a|r|n\rangle$ is the radial transition matrix element and the factors $|C_q|^2$ are dipole matrix elements of the Racah spherical tensors given by

$$|C_q|^2 = |\langle a|C_q^{(1)}|n\rangle|^2. \tag{9.139}$$

This gives the following key result for the *resonant magnetic scattering factor*, defined in (9.20) [365, 412].

The *elastic resonant magnetic scattering factor* in units [number of electrons] is given by

$$F(\hbar\omega) = \frac{\hbar\omega^2\alpha_\mathrm{f}\mathcal{R}^2}{2cr_0}\left[\underbrace{(\boldsymbol{\epsilon}_2^*\cdot\boldsymbol{\epsilon}_1)\,G_0}_{\text{charge}} + \underbrace{\mathrm{i}(\boldsymbol{\epsilon}_2^*\times\boldsymbol{\epsilon}_1)\cdot\hat{\boldsymbol{m}}\,G_1}_{\text{XMCD}} + \underbrace{(\boldsymbol{\epsilon}_2^*\cdot\hat{\boldsymbol{m}})(\boldsymbol{\epsilon}_1\cdot\hat{\boldsymbol{m}})\,G_2}_{\text{XMLD}}\right], \tag{9.140}$$

where α_f is the dimensionless fine structure constant given by (9.62), $\mathcal{R}^2$ the radial transition matric element, r_0 the classical electron radius, and

$$G_0 = \sum_n \frac{|\langle a|C_{+1}^{(1)}|n\rangle|^2 + |\langle a|C_{-1}^{(1)}|n\rangle|^2}{(\hbar\omega - E_R^n) + \mathrm{i}(\Delta_n/2)}\ , \tag{9.141}$$

$$G_1 = \sum_n \frac{|\langle a|C_{-1}^{(1)}|n\rangle|^2 - |\langle a|C_{+1}^{(1)}|n\rangle|^2}{(\hbar\omega - E_R^n) + \mathrm{i}(\Delta_n/2)}\ , \tag{9.142}$$

and

$$G_2 = \sum_n \frac{2|\langle a|C_0^{(1)}|n\rangle|^2 - |\langle a|C_{-1}^{(1)}|n\rangle|^2 - |\langle a|C_{+1}^{(1)}|n\rangle|^2}{(\hbar\omega - E_R^n) + \mathrm{i}(\Delta_n/2)}\ . \tag{9.143}$$

The first term in (9.140) is independent of the magnetic moment. The numerator of G_0 has the form of the natural linear dichroism intensity given by (9.112) for linear polarization and (9.113) for circular polarization. As indicated in (9.140) it describes the resonant scattering from a *spherical* charge

distribution. The polarization dependence $(\boldsymbol{\epsilon}_2 \cdot \boldsymbol{\epsilon}_1)$ is the same as for Thomson scattering. The scalar product is finite only if the incident and scattered polarizations are collinear, that is the photon polarization is not rotated upon scattering.

The second term has a linear dependence on the magnetic moment and the numerator of the matrix element G_1 has the same form as (9.102), describing XMCD. It therefore describes magnetic *circular* dichroism. The polarization dependence is $(\boldsymbol{\epsilon}_2 \times \boldsymbol{\epsilon}_1)$ so that the polarization is rotated on scattering.

The third term is quadratic in the magnetic moment and the matrix elements in G_2 are of the same form as those for XMLD given by (9.124). Hence the term describes magnetic *linear* dichroism. The polarization dependence is more complicated and in general the polarization is partially rotated in the scattering process.

9.8.2 Link of Magnetic Resonant Scattering and Absorption

In order to establish the link between the imaginary part $f_2(\hbar\omega)$ of the magnetic resonant scattering factor and the X-ray absorption cross-section $\sigma^{\mathrm{abs}}(\hbar\omega)$, we start from $F(\hbar\omega)$ given by (9.137). For simplicity we restrict ourselves to one well-defined resonant transition via a state $|n\rangle = |b\rangle$ so that we can drop the sum. This gives

$$F(\hbar\omega) = \frac{\hbar\omega^2}{cr_0}\,\alpha_{\mathrm{f}}\,\frac{\langle a|\boldsymbol{r}\cdot\boldsymbol{\epsilon}_2^*|b\rangle\langle b|\boldsymbol{r}\cdot\boldsymbol{\epsilon}_1|a\rangle}{(\hbar\omega - E_{ba}) + \mathrm{i}(\Delta_b/2)}\ . \tag{9.144}$$

where $E_{ba} = E_b - E_a$ is the resonant energy and Δ_b is the FWHM of the intermediate state.

We now want to prove the relationship (9.135). Without dealing with the different polarization cases, which we shall do later, let us quickly see how the scattering factor transforms into the absorption cross-section. If we assume that the unit polarization vectors are real and consider *forward scattering* so that $\boldsymbol{\epsilon}_1 = \boldsymbol{\epsilon}_2 = \boldsymbol{\epsilon}$ we get $\langle a|\boldsymbol{r}\cdot\boldsymbol{\epsilon}|b\rangle\langle b|\boldsymbol{r}\cdot\boldsymbol{\epsilon}|a\rangle = |\langle b|\boldsymbol{r}\cdot\boldsymbol{\epsilon}|a\rangle|^2$. Next we rewrite the denominator in (9.144) as a real and imaginary part

$$\frac{1}{(\hbar\omega - E_{ba}) + \mathrm{i}(\Delta_b/2)} = \frac{\hbar\omega - E_{ba}}{(\hbar\omega - E_{ba})^2 + (\Delta_b/2)^2} - \mathrm{i}\pi \underbrace{\frac{2}{\pi\Delta_b}\,\frac{(\Delta_b/2)^2}{(\hbar\omega - E_{ba})^2 + (\Delta_b/2)^2}}_{\rho(E_b)}\ . \tag{9.145}$$

The imaginary term denoted by an under-bracket represents a normalized Lorentzian of unit area and dimension [1/energy] according to Appendix A.9. As indicated we can use this function to represent the density of states $\rho(E_b)$ associated with the intermediate state $|b\rangle$. By substituting into (9.144) and with $\hbar\omega = E$ we obtain the desired result

$$\mathrm{Im}[F(\hbar\omega)] = f_2(\hbar\omega) = \frac{\pi\omega}{cr_0}\,\alpha_\mathrm{f}\,\hbar\omega\;|\langle b|\,\boldsymbol{\epsilon}\cdot\boldsymbol{r}|a\rangle|^2\;\rho(E_b)\;.$$
$$= \frac{\omega}{4\pi cr_0}\,\sigma^{\mathrm{abs}}(\hbar\omega) = \frac{\hbar\omega}{2h\,c\,r_0}\,\sigma^{\mathrm{abs}}(\hbar\omega) = \frac{E}{C^*}\,\sigma^{\mathrm{abs}}(\hbar\omega)\,. \quad (9.146)$$

Here we have used (9.59), with implicit requirement of the energy conserving δ-function. Our result (9.146) constitutes a quantum mechanical proof of the optical theorem (9.49), extended to magnetic systems. Let us now take a closer look at the detailed polarization-dependent terms in the resonant magnetic scattering factor given by (9.140).

Linear Polarization

For linearly polarized incident X-rays, $\boldsymbol{\epsilon}$ is real and only the first and third terms are nonzero. By use of (9.145) we obtain from (9.140)

$$f_2(\hbar\omega) = \underbrace{\frac{\hbar\omega}{2hcr_0}}_{E/C^*}\underbrace{4\pi^2\alpha_\mathrm{f}\hbar\omega}_{\mathcal{A}}\mathcal{R}^2\;\;\rho(E_b)\;\Bigg[\underbrace{\frac{1}{2}\left\{|C_{+1}|^2+|C_{-1}|^2\right\}}_{\text{charge}}$$
$$+\underbrace{\frac{1}{2}|\boldsymbol{\epsilon}\cdot\hat{\boldsymbol{m}}|^2\left\{2|C_0|^2-|C_{-1}|^2-|C_{+1}|^2\right\}}_{\text{XMLD}}\Bigg]\,. \quad (9.147)$$

In comparing the terms labelled "charge" and "XMLD" to the relevant expressions for the X-ray absorption *intensities* we need to ignore the conversion factor E/C^* and integrate the density of states factor $\rho(E_b)$ over energy which per our definition gives unity (see Appendix A.9). Our result for the charge term is then found to be identical to the X-ray absorption intensity for linear polarized X-rays given by (9.112). Since the result does not depend on the orientation of the polarization vector $\boldsymbol{\epsilon}$ in space, we see that this term reflects absorption by a spherically symmetric charge density.

The XMLD term is identical to our previous result given by (9.124) if we take the difference of the intensities for $\boldsymbol{\epsilon} \parallel \hat{\boldsymbol{m}}$ and $\boldsymbol{\epsilon} \perp \hat{\boldsymbol{m}}$ according to (9.119). This establishes the link between the resonant scattering factor in the forward scattering geometry and the XMLD absorption intensity.

Circular Polarization

For incidence along the z quantization axis, circularly polarized X-rays with positive and negative helicity are described by (5.35) and (5.36) or

$$\boldsymbol{\epsilon}^{\pm} = \mp \frac{1}{\sqrt{2}} \left(\boldsymbol{\epsilon}_x \pm \mathrm{i} \boldsymbol{\epsilon}_y \right) , \tag{9.148}$$

Defining $\boldsymbol{\epsilon}_x \times \boldsymbol{\epsilon}_y = \boldsymbol{\epsilon}_{\boldsymbol{z}} = \boldsymbol{k}_0$, where $\boldsymbol{k}_0$ is the unit vector in the direction of X-ray propagation, we have

$$\mathrm{i} \left[(\boldsymbol{\epsilon}^{\pm})^* \times \boldsymbol{\epsilon}^{\pm} \right] = \mp \boldsymbol{k}_0 \ , \tag{9.149}$$

meaning that for positive helicity light the cross product gives $-\boldsymbol{k}_0$ and for negative helicity light $+\boldsymbol{k}_0$. We obtain from (9.140),

$$f_2(E) = \frac{E}{C^*} \mathcal{A} \mathcal{R}^2 \, \rho(E_b) \left[\underbrace{\frac{1}{2} \left\{ |C_{+1}|^2 + |C_{-1}|^2 \right\}}_{\text{charge}} \underbrace{\mp (\boldsymbol{k}_0 \cdot \hat{\boldsymbol{m}}) \frac{1}{2} \left\{ |C_{-1}|^2 - |C_{+1}|^2 \right\}}_{\text{XMCD}} \right] . \tag{9.150}$$

The charge term is equivalent to the natural linear dichroism intensity given by (9.112) for linear polarization and (9.113) for circular polarization. Since it does not depend on the orientation of the polarization vector ϵ in space it represents the resonant scattering from a *spherical* charge distribution.

If we form the difference between intensities measured with left and right circular polarization according to our XMCD definition (9.95), the charge term drops out and we obtain

$$\Delta f_2(E) = f_2^-(E) - f_2^+(E) = \frac{E}{C^*} \mathcal{A} \mathcal{R}^2 \, \rho(E_b) \left\{ |C_{-1}|^2 - |C_{+1}|^2 \right\} . \tag{9.151}$$

Without the conversion factor E/C^* and after energy integration this result is identical to that derived earlier in (9.102).

In Chap. 10 we shall explore through experiments the theoretical concepts developed earlier.

10

X-rays and Magnetism: Spectroscopy and Microscopy

10.1 Introduction

The goal of the present chapter is to give an overview of experimental X-ray techniques for the determination of the magnetic properties of matter. While it will be advantageous for the reader to have worked through the theoretical concepts developed in Chap. 9, the present chapter is mostly written from an experimentalist's point of view. The chapter may therefore be understood without having mastered the detailed theory of Chap. 9. To facilitate this task, we will present a short summary of the concepts underlying the various X-ray dichroism effects in Sect. 10.2. We will then focus on experimental procedures, data analysis techniques, and the relation of X-ray resonance intensities with magnetic quantities, for example the link between X-ray absorption intensities and magnetic moments. In all cases we illustrate the concepts by experimental results. Our treatment reflects the fact that polarized X-ray techniques have become of considerable importance for the study of magnetic phenomena and materials, owing to their elemental, chemical, and magnetic specificity. We will show here that spectroscopic and microscopic results may be linked to magnetic properties of interest by simple analysis procedures.

We highlight X-ray absorption techniques, both spectroscopy and spectromicroscopy, because of their simplicity and direct link to magnetic properties. We also touch on X-ray scattering, in particular, the use of resonant coherent techniques for magnetic imaging. Absorption and scattering are related as discussed in Sect. 9.8. In practice, the resonantly scattered intensity can always be obtained by the Kramers–Kronig transformations as discussed in Sect. 9.4.4. We shall not specifically discuss reflectivity experiments, which are closely related to scattering experiments and, like the magneto-optical Kerr technique, may conveniently be used for magnetic characterization [358–361]. In contrast to X-ray absorption, however, scattering and reflectivity experiments contain information on both the absorptive and refractive part of the refractive index $n(\omega)$ (see (9.1), (9.6), and (9.7)) and the analysis is there-

fore more complicated. In particular, care has to be exercised regarding the measured sign of the dichroism signal [358, 361].

Two types of X-ray absorption spectroscopy are often distinguished. The first is concerned with the study of resonances near the absorption edges, often called *near edge X-ray absorption fine structure* (NEXAFS) [189] or *X-ray absorption near edge structure* (XANES) [413]. The near edge fine structure originates from transitions between a core state and localized valence states. For the transition metals, for example, we are mostly interested in dipole transitions from $2p$ core to $3d$ valence states. The intensity of such transitions provides direct information on the magnetic properties of the important d valence electrons and represents the most powerful use of X-ray absorption spectroscopy for the study of magnetic materials.

The second type of spectroscopy deals with nonresonant absorption and is typically called the extended X-ray absorption fine structure (EXAFS) [413]. Magnetic EXAFS, which exists in the region starting tens of eV above the absorption edge, originates from spin-dependent scattering of the excited photoelectron off the magnetic neighbors and may be useful for studies of the local magnetic structure [414, 415]. We shall not treat it here because we believe resonant effects to be more important.

The structure of the chapter is as follows. We first give a quick overview over the four most important dichroism effects and how they manifest themselves in measured spectra. The rest of the chapter consists of two major parts, dealing with spectroscopy and microscopy. We first discuss experimental procedures for polarization dependent X-ray absorption spectroscopy, data analysis methods and present selected results. We concentrate on spectroscopic studies of the $3d$ transition metals, using their L absorption edges. We then turn to magnetic microscopy with X-rays, better called "spectro-microscopy", because the method combines the principles of spectroscopy such as changes of X-ray energy and polarization with imaging methods. Both real space imaging methods and reciprocal space methods such as holography are discussed and illustrated by examples.

10.2 Overview of Different Types of X-ray Dichroism

The term "dichroism" needs a short explanation. We have learned in Chap. 9 that historically, the term *dichroism* specifically referred to polarization dependent *absorption* of light. On a microscopic level the origin of dichroic behavior of a material originates from the spatial anisotropy of the charge or the spin. In cases where the spins are not aligned and the effect depends on charge, only, one speaks of *charge or "natural" dichroism*.

X-ray "natural" dichroism refers to the absence of spin alignment.

- X-ray natural linear dichroism – X**NL**D – is due to an anisotropic charge distribution. The effect is parity even and time even.
- X-ray natural circular dichroism – X**NC**D – may be present for anisotropic charge distributions that lack a center of inversion. The effect is parity odd and time even.

If the origin of dichroism is due to preferential spin alignment or magnetic order one speaks of *magnetic dichroism*. We distinguish *directional* spin alignment, as in a ferromagnet or ferrimagnet, from *axial* spin alignment as in a collinear antiferromagnet. The term "directional" is more restrictive since a directional alignment is also axial, but not vice versa. There are two important types of magnetic dichroism.

X-ray "magnetic" dichroism is due to spin alignment and the spin–orbit coupling.

- X-ray magnetic linear dichroism – X**ML**D – arises from a charge anisotropy induced by *axial* spin alignment. The effect is parity even and time even.
- X-ray magnetic circular dichroism – X**MC**D – arises from *directional* spin alignment. The effect is parity even and time odd.

There are other more complicated types of "magnetic" dichroism where charge and spin effects are both present [88, 416]. For example, X-ray *magnetochiral dichroism* arises from axial spin alignment and a chiral charge distribution and the effect is parity odd and time odd [417]. X-ray *nonreciprocal linear dichroism* arises from charge chirality that is induced by an axial spin alignment and the effect is parity odd and time odd [418]. We shall not discuss these cases here. Rather we shall first give a summary of the four kinds of natural and magnetic dichroism highlighted by the boxes above and then specifically treat the three cases of XNLD, XMLD, and XMCD. It turns out that these three types of dichroism are connected and in contrast to XNCD they all arise within the dipole approximation.

The simplest case of dichroism which has been extensively discussed in the book *NEXAFS Spectroscopy* [189] is *X-ray natural linear dichroism*, XNLD, due to anisotropic bonding. The most beautiful examples of XNLD are found in covalently bonded systems, such as organic molecules and polymers, where the bonding is directional. Often a simple picture, called the "search light effect", can be used to predict the angle-dependent intensity associated with a transition of a core electron to an empty molecular (valence) orbital. If the $\boldsymbol{E}$ vector points into the direction of maximum density of the empty molecular orbital (one could say "hole" density), the transition is strongest, and it is weakest for $\boldsymbol{E}$ perpendicular to the orbital density. An example is shown in

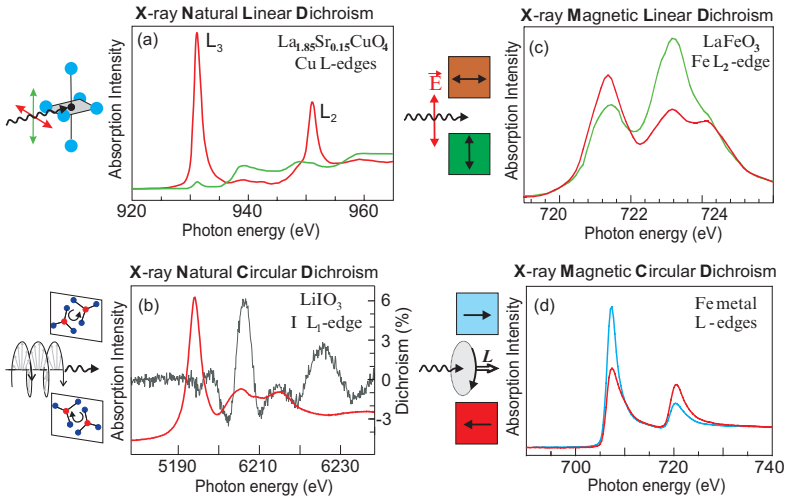

Fig. 10.1. Four important types of dichroism. (**a**) X-ray natural linear dichroism spectra of $La_{1.85}Sr_{0.15}CuO_4$ near the Cu L-edge [419]. The resonances are due to transitions to the highest energy unfilled $d_{x^2-y^2}$ orbital. (**b**) X-ray absorption spectrum (red) of single crystal $LiIO_3$ and the difference spectrum (gray), the X-ray natural circular dichroism spectrum, obtained from absorption spectra with left and right circularly polarized X-rays, incident along a special crystalline axis [420]. (**c**) Magnetic linear dichroism spectrum of an epitaxial thin film of antiferromagnetic $LaFeO_3$ with the $\boldsymbol{E}$ vector aligned parallel and perpendicular to the antiferromagnetic axis [406]. The splitting of the L_2 resonance is due to multiplet effects. (**d**) X-ray magnetic circular dichroism spectrum around the L_3 and L_2 edges of Fe metal. The photon angular momentum was aligned parallel or antiparallel to the magnetization direction of the sample [96]

Fig. 10.1a for the Cu L-edge of $La_{1.85}Sr_{0.15}CuO_4$ [419]. The single crystal sample has a layered structure. The Cu atom shown in black is surrounded by 4 in-plane O atoms and two out-of-plane O atoms. If we define the x, y plane of our coordinate system to lie in the plane of the layers (shown in gray) the in-plane $d_{x^2-y^2}$ orbital is unfilled and when the $\boldsymbol{E}$ lies in the x, y plane a large peak-like transition is observed to this orbital. This resonance is absent when $\boldsymbol{E}$ is oriented perpendicular to the plane, as shown, since there are no empty states in the perpendicular direction. XNLD is used to probe the anisotropy of the valence charge. It is a powerful technique for the determination of the orientation of molecules and functional groups on surfaces and in organic materials [189], the direction and the nature of local bonds in materials [372], and even the orientational order in amorphous materials, that is materials without translational order [388, 421].

X-ray natural circular dichroism, XNCD, may be observed if the bonding around the absorbing atom lacks a center of inversion. The origin of XNCD

may be visualized by picturing the bonding around the absorbing atom as possessing a handedness in space. When the handed circular light is also pictured in space, as shown in Fig. 5.3, it is then intuitively plausible that the X-ray absorption depends on whether the handedness of the charge and that of the EM wave are the same or opposite. This model also conveys the important fact that the EM wave must contain a $\boldsymbol{k}$ dependence, since only then will it have a "twist" over the atomic volume. This intuitive picture is theoretically reflected by the fact that XNCD vanishes in the dipole approximation.[1] An example of XNCD is shown in Fig. 10.1b for the Iodine L_1-edge X-ray absorption spectrum (red) of single crystal $LiIO_3$. The XNCD spectrum, defined as the difference of two absorption spectra obtained with left and right circularly polarized X-rays, is shown in gray [420, 422, 423]. It was obtained by aligning the single crystal sample along a special crystalline axis. The effect is seen to be remarkably large of the order of several per cent. Within the context of this book we shall not discuss XNCD any further.

Next we give a brief introduction to *X-ray magnetic linear dichroism*, XMLD. We have seen above that both *natural* and *magnetic* linear dichroism effects are parity even and time even. They are therefore related and their separation is sometimes tricky. The principal difference is that XMLD only exists in the presence of magnetic alignment and hence it vanishes at temperatures above the Neél or Curie temperature, or for paramagnets in the absence of an external magnetic field. There are two important prerequisites for the existence of XMLD: the existence of atomic magnetic moments and the *spin–orbit interaction*. For example, in ferro- and antiferromagnets, the exchange interaction creates a spin magnetic moment. The spin–orbit interaction creates an orbital magnetic moment which is locked to both the spin moment and the lattice. The result is the creation of a macroscopic "easy" axis along which the spins lie. Ferro- or ferri-magnets are *directional* since there is a net moment direction while collinear antiferromagnets are *axial* since all spins lie along a particular axis of the crystal but there is no net moment. Both can be studied with XMLD.

[1] The dipole approximation neglects the $\boldsymbol{k}$ dependence of the EM wave. It assumes $\boldsymbol{E}\mathrm{e}^{\mathrm{i}\boldsymbol{k}\cdot\boldsymbol{r}} = \boldsymbol{E}(1+\mathrm{i}\boldsymbol{k}\cdot\boldsymbol{r}+\cdots) = \boldsymbol{E}$ (see Sect. 9.5.3) and thus neglects the spatial "twist" of the wave over the atomic volume. XNCD arises from keeping the first order term in $\boldsymbol{k}$ in the transition matrix element $M = \langle b|\,(\boldsymbol{p}\cdot\boldsymbol{E})\,(1+\mathrm{i}\boldsymbol{k}\cdot\boldsymbol{r})\,|a\rangle$, so that

$$M = \underbrace{\langle b|\boldsymbol{p}\cdot\boldsymbol{E}|a\rangle}_{\mathcal{A}} + \underbrace{\frac{\mathrm{i}}{2}\langle b|(\boldsymbol{r}\times\boldsymbol{p})\cdot(\boldsymbol{k}\times\boldsymbol{E})|a\rangle}_{\mathcal{B}} + \underbrace{\frac{\mathrm{i}}{2}\langle b|(\boldsymbol{k}\cdot\boldsymbol{r})(\boldsymbol{p}\cdot\boldsymbol{E}) + (\boldsymbol{k}\cdot\boldsymbol{p})(\boldsymbol{r}\cdot\boldsymbol{E})|a\rangle}_{\mathcal{C}}\,.$$

Term $\mathcal{A}$ is the electric dipole term, $\mathcal{B}$ the electric dipole/magnetic dipole interference term, and $\mathcal{C}$ the electric dipole/electric quadrupole interference term. NCD in the optical range arises from term $\mathcal{B}$, whereas XNCD is mostly due to term $\mathcal{C}$. XNCD vanishes for samples without orientational order, and single crystal samples are required. Also, not all samples that lack inversion symmetry exhibit XNCD but only a subgroup, as discussed in more detail by Natoli et al. [422].

The existence of a macroscopic magnetic axis leads to a difference in X-ray absorption intensity when the polarization vector is either parallel or perpendicular to the magnetic axis. This can happen in different ways. The most obvious case is when in the presence of magnetic order the lattice lowers its symmetry. For example, a cubic lattice may experience a contraction along the magnetic axis. The charge becomes anisotropic and this causes a *natural* linear dichroism effect that is magnetically induced. Another prominent origin of XMLD is the presence of coupled electronic (multiplet) states that are formed under the influence of the exchange and spin–orbit interactions. Such states typically have a nonspherical charge distribution and when transitions between pairs of such states are energetically separated there can be a large polarization dependence of individual transitions. This is the origin of the large XMLD effect in the multiplet-split Fe L_2 resonance in $LaFeO_3$ shown in Fig. 10.1c. The spectra show the difference in absorption when the $\boldsymbol{E}$ vector is aligned parallel and perpendicular to the antiferromagnetic axis in $LaFeO_3$ [406]. XMLD is extensively used today for the study of antiferromagnets, in particular, the determination of the orientation of the antiferromagnetic axis in thin films and near surfaces, and the imaging of antiferromagnetic domains.

We conclude the overview of dichroism effects with *X-ray magnetic circular dichroism*, XMCD. It is used to measure the size and direction of magnetic moments. Both the magnetic moments and the XMCD effect are time odd and parity even. As illustrated in Fig. 10.1d for the Fe L-edge in Fe metal, the XMCD effect is maximum when the X-ray angular momentum is parallel and antiparallel to the magnetic moment of the sample. The effect is seen to be very large at the resonance positions and is opposite at the L_3 and L_2 edges. This directly reflects the opposite sign of the spin component at the two edges, $j = l + s$ at the L_3 edge and $j = l - s$ at the L_2 edge. Like magnetic linear dichroism, XMCD requires the presence of a magnetic alignment, which has to be directional. It is therefore zero for antiferromagnets. It also requires the presence of spin–orbit coupling because the photon angular momentum does not directly couple to the electron spin but only indirectly via the orbital angular momentum. This is because the electronic transition is driven by the electric field which does not act on spin but only on the orbital angular momentum through the charge.

In a simple picture, in the absorption process a handed photon transfers its angular momentum to a core electron. The X-ray energy is tuned so that the created photoelectron is excited into the valence shell. If the valence shell has a preferential angular momentum direction the transition probability will depend on whether the photon and valence shell angular momenta are parallel or antiparallel. The dependence of XMCD on the spin–orbit coupling has the benefit that it allows the separate determination of spin and orbital angular momenta (and therefore moments) from linear combinations of the measured L_3 and L_2 dichroism intensities. This and the ability to determine the size and direction of the moments is a consequence of the famous XMCD sum rules that we shall discuss later in the chapter. XMCD has become an important magnetic tool partly because it allows the study of magnetic properties in

combination with submonolayer sensitivity, elemental specificity, and chemical state specificity. When nanoscale magnetic imaging and ultrafast time resolution are added we have a method that is unique for the study of modern magnetic materials.

10.3 Experimental Concepts of X-ray Absorption Spectroscopy

This section gives concepts and experimental details of X-ray absorption spectroscopy. We do not yet discuss *polarization dependent* changes in the spectra, i.e., dichroic effects, but rather concentrate on the basic concepts that determine absorption spectra of magnetic materials spectra. In particular, we outline basic experimental techniques, and by examples of selected X-ray absorption spectra, we discuss important spectral features and aspects of data normalization and analysis. As examples we will predominantly use L-edge spectra of the transition metals since they are best suited to obtain information for the important $3d$ transition metals. We mention that other absorption edges have also been used, like the K-edges of the $3d$ transition metals, first investigated by Schütz in her pioneering XMCD work [95], or the $M_{2,3}$ edges of the $4d$ metals [424, 425] and even the $M_{4,5}$ edges of the actinides [409].

10.3.1 General Concepts

In the last chapter we have seen that the *X-ray absorption intensity* is attenuated upon transmission through a sample of thickness d according to

$$I = I_0 \, \mathrm{e}^{-\mu_x \, d} = I_0 \, \mathrm{e}^{-\rho_\mathrm{a} \, \sigma^\mathrm{abs} \, d} \; . \tag{10.1}$$

Here μ_x is the linear *X-ray absorption coefficient* with a dimension of [length^{-1}], and σ^abs is the *X-ray absorption cross-section* of dimension [length^2/atom]. The two quantities are related according to (9.29) by the atomic number density $\rho_\mathrm{a} = N_\mathrm{A}\rho_\mathrm{m}/A$ with dimension [atoms/length^3], where $N_\mathrm{A} = 6.02214 \times 10^{23}$ [atoms/mol] is Avogadro's number. We have listed in Table 10.1 the relevant parameters for Fe, Co, and Ni.

Table 10.1. Bulk Properties of $3d$ metals Fe, Co, Ni. Listed are the mass density ρ_m at room temperature, the atomic mass number A, the atomic number density ρ_a and the atomic volume V_a

Element	ρ_m [kg/m^3]	A [g/mol]	ρ_a [atoms/nm^3]	V_a [Å^3]
Fe (bcc)	7,874	55.845	84.9	11.8
Co (hcp)	8,900	58.933	90.9	11.0
Ni (fcc)	8,908	58.693	91.4	10.9

Historically, X-ray absorption has been measured in a transmission geometry as shown in Fig. 10.2a and the transmitted intensity drops when the X-ray absorption channel is opened up at a threshold (absorption edge), corresponding to loss of photons through core electron excitation to empty states. On the right side of Fig. 10.2a we show a typical measured transmission intensity I_t, normalized to the incident number of photons I_0. The shown spectrum corresponds to a $d = 10\,\mathrm{nm}$ Co film, calculated by means of (10.1) from the

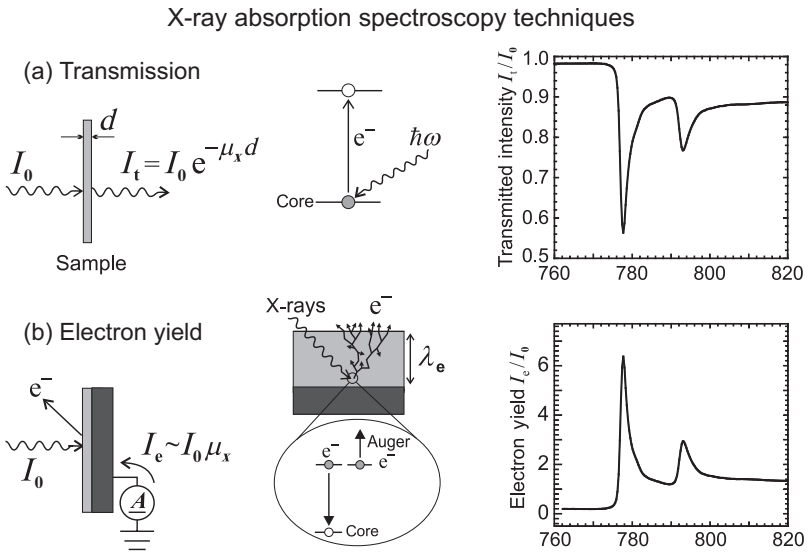

Fig. 10.2. Two common methods for the measurement of X-ray absorption. In the top row (**a**) we show a typical transmission geometry used for X-ray absorption measurements, the core electron excitation process during an absorption event, and a schematic of the measured transmitted intensity. We have used real data for Co metal, and the plotted transmission intensity I_t/I_0 corresponds to a Co thickness of 10 nm. In the bottom row (**b**) we illustrate the method and principles of recording absorption spectra by electron yield (or total electron yield) detection. The absorbed photons create core holes that are filled by Auger electron emission. The primary Auger electrons cause a low energy cascade through inelastic scattering processes on the way to the surface. The total number of emitted electrons is directly proportional to the probability of the Auger electron creation, that is the absorption probability. The emitted electron yield is simply measured with a picoammeter that measures the electrons flowing back to the sample from ground. The electron yield spectrum I_e/I_0 shown on the right is that of Co metal. The numbers on the ordinate actually correspond to the cross-section in Mb since we have simply converted (renormalized) the measured electron yield ratio I_e/I_0 into a cross-section as discussed in conjunction with Fig. 10.9

experimentally measured averaged dichroism spectra shown in Fig. 10.12. It is common to present X-ray absorption spectra "downside-up" by plotting the quantity $\ln(I_0/I)$ which is proportional to μ_x or σ^{abs} and we shall use such plots from now on.

There are two other methods for the measurement of X-ray absorption by solids, X-ray fluorescence and electron yield (EY) detection, as discussed in detail by Stöhr [189]. Of the two methods, EY detection, also called *total electron yield detection*, is particularly often used in the soft X-ray region where it offers larger signals due to the dominance of the Auger over the fluorescence decay channel after X-ray excitation [189]. It is also experimentally simple and requires just a picoammeter for the measurement of the photocurrent. It is for these reasons and the important fact that it underlies photoemission electron microscopy (PEEM), discussed later, that we shall discuss EY detection here. The experimental method and the underlying electronic processes are shown in Fig. 10.2b and are explained in the caption. EY detection directly gives a spectrum that is proportional to the X-ray absorption coefficient or the absorption cross-section because the yield is directly proportional to the probability of X-ray absorption. This is seen by writing down the number of absorbed photons according to (10.1) under the assumption of a thin sample $d \ll 1/\mu_x$. We get

$$I_0 - I_t = I_0(1 - \mathrm{e}^{-\mu_x\, d}) \simeq I_0\, d\, \mu_x = I_0\, \rho_{\text{a}}\, d\, \sigma^{\text{abs}}. \tag{10.2}$$

Fortunately, for EY measurements the approximation (10.2) is not only valid for thin samples d but it turns out that it is valid in general since one always measures in the limit of a "thin sample." This is due to the fact that the EY signal originates only from a depth $\lambda_{\text{e}} \sim 2$ nm that is much shorter than the X-ray penetration length or *X-ray absorption length* λ_x into the sample. This topic has been discussed extensively elsewhere [189, 426] and we shall here only review the important facts.

The X-ray absorption length $\lambda_x = 1/\mu_x$ is the distance in a material over which the intensity has dropped to $1/e$ of its original value. This length depends strongly on the photon energy and as the absorption coefficient μ_x increases close to an edge, λ_x becomes shorter. For convenience we have listed in Table 10.2 values for σ^{abs} and μ_x for Fe, Co, and Ni at three characteristic

Table 10.2. X-ray absorption cross-sections σ^{abs} [Mb] and linear absorption coefficients $\mu_x[\text{nm}^{-1}]$ for Fe, Co, Ni for three energies, 10 eV below the L_3 peak, at the L_3 peak and 40 eV above the L_3 peak. For the conversion between σ^{abs} and μ_x it is convenient to remember that $1\,\text{M}b = 10^{-4}\,\text{nm}^2$

	10 eV below L_3		at L_3 peak		40 eV above L_3	
Element	σ^{abs} [Mb]	$\mu_x[\text{nm}^{-1}]$	σ^{abs} [Mb]	$\mu_x[\text{nm}^{-1}]$	σ^{abs} [Mb]	$\mu_x[\text{nm}^{-1}]$
Fe (bcc)	0.21	1.8×10^{-3}	7.1	6.0×10^{-2}	1.45	1.2×10^{-2}
Co (hcp)	0.195	1.8×10^{-3}	6.4	5.8×10^{-2}	1.34	1.2×10^{-2}
Ni (fcc)	0.18	1.6×10^{-3}	4.6	4.2×10^{-2}	1.28	1.2×10^{-2}

energies, 10 eV below the L_3 peak, at the L_3 peak, and 40 eV above the L_3 peak. We see that the X-ray absorption length $1/\mu_x$ is about 500 nm before the edge, 20 nm at the L_3 peak and 80 nm above the L_3 peak.

We now take a look at the *electron sampling depth* λ_e. As illustrated in Figs. 10.2b and 10.3, the absorption of the incident X-rays leads to the production of Auger electrons that trigger an electron cascade. Only those cascade electrons that have enough energy to overcome the work function of the sample contribute to the measured electron yield. If one thinks of the sample as consisting of atomic layers parallel to the surface, as illustrated on the left side of Fig. 10.3, one can show that the EY contribution from the individual layers falls off exponentially with their perpendicular distance from the surface plane [189].[2] The depth below the surface of the layer whose contribution is $1/e$ of that of the first layer is called the *electron sampling depth* λ_e, and experiments show it to be about 2 nm for Fe, Co, and Ni [426]. One may also refer to λ_e as an effective secondary electron mean free path (see footnote 2). The short value of λ_e causes a high sensitivity to the near surface region or layers, as illustrated on the right side of Fig. 10.3 for a wedge sample. It was grown on a Si substrate (not shown) and consists of a 5 nm-thick Ni film, covered by an Fe wedge of thickness 0–3.5 nm, a constant thickness (1 nm) Cu film and a 1.5 nm Pt cap layer. As the X-ray beam is moved across the wedge toward increasing Fe thickness the EY spectra clearly reveal the increase in the Fe signal and the decrease of the Ni substrate signal, as expected for the short EY sampling depth.

For the L-edge absorption region of Fe, Co, and Ni, the $1/e$ *electron yield sampling depth* λ_e from which 63% of the signal originates is about 2 nm. In contrast, the $1/e$ *X-ray absorption length* $\lambda_x = 1/\mu_x$ is strongly energy dependent and is about 500 nm before the edge, 20 nm at the L_3-edge, and 80 nm above the edge.

Despite the fact that the X-ray absorption length λ_x is at least 10 times larger than the electron yield sampling depth λ_e one still needs to be careful in the quantitative analysis of EY absorption spectra since the peak intensities are slightly reduced relative to the true X-ray absorption cross-section [426]. This is referred to as the *saturation effect* in the literature. Its origin is easy to understand. Ideally the different layers in the sample contribute to the EY with an exponentially decaying intensity as shown on the left side of Fig. 10.3.

[2] This can be derived in analogy to the concepts used in photoemission, where the inelastic scattering or attenuation of the elastic electrons along a direction x is described by an exponential decay of the form $I = I_0 \exp(-i\ell_e x)$, where ℓ_e is the *electron mean free path*. This leads to an exponential decay of the elastic photoemission signal from layers below the surface, similar to that shown in Fig. 10.3. In total electron yield measurements one defines an *effective mean free path* λ_e that averages over the various scattering channels [189].

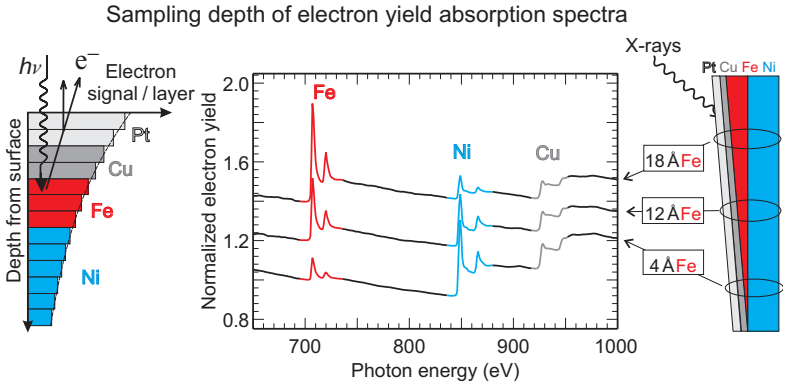

Fig. 10.3. *Left*: Illustration of layer-by-layer contributions to the electron yield signal from a sample consisting of different layers. We have assumed that the X-ray absorption length is much larger than the electron sampling depth, $\lambda_x \gg \lambda_e$. For simplicity we have also assumed that both λ_x and λ_e are the same for the different layers. *Middle* and *right*: X-ray absorption spectra of a wedge sample grown on a Si substrate with the layered structure Ni(5 nm)/Fe(0–3.5 nm)/Cu(1 nm)/Pt(1.5 nm). The spectra reveal the preferential sensitivity to the near-surface layers. As the Fe wedge gets thicker its signal increases relative to that of the underlying Ni. The Cu layer of constant thickness contributes an approximately constant signal, as revealed by the jump at its absorption edge. The Pt cap layer has no absorption edge in the shown spectral region and contributes only a constant background signal. The curves have been vertically shifted relative to each other to facilitate their comparison

If the X-ray absorption length λ_x becomes shorter at the resonance position, say $\lambda_x \approx 10\lambda_e$, of the order of 10% of the photons with that energy are absorbed within the electron sampling depth. This means that the X-ray intensity that reaches the deeper layers in the sample is already reduced by several percent at the resonance positions. Therefore the contributions from the deeper layers at the resonance energy is less than the ideal contribution shown in Fig. 10.3, and the relative total EY intensity at the resonance position is reduced relative to that outside the resonance. EY absorption spectra therefore need to be corrected for saturation effects as discussed in the literature [406, 426–431]. We shall come back to this point below (see Fig. 10.9).

10.3.2 Experimental Arrangements

In the soft X-ray region, X-ray absorption experiments on magnetic materials are typically carried out as shown in Fig. 10.4.

A suitable undulator produces X-rays of selectable polarization, and a monochromator selects the photon energy of interest with a typical energy resolution of 0.2 eV. The monochromatic X-rays are then focused to a spot

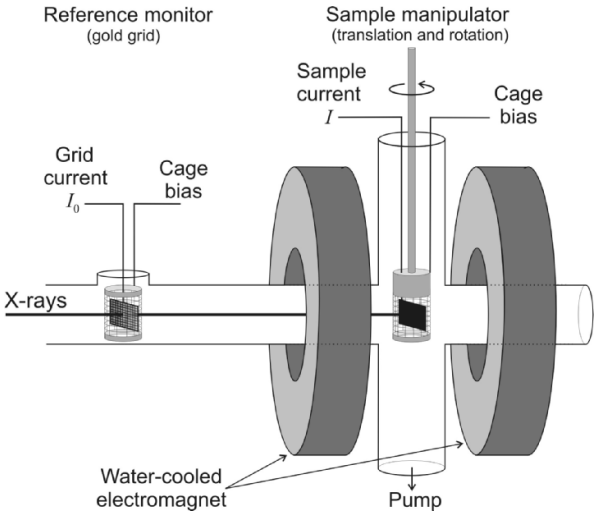

Fig. 10.4. Basic components of X-ray magnetic dichroism spectroscopy. The polarized, monochromatic X-rays are incident on an intensity reference monitor consisting of a high transmission (∼80%) metal (e.g., gold) grid that is enclosed by a cage that is positively biased relative to the sample. The electron photocurrent from the grid, I_0, measured with a picoammeter, serves as a reference of the X-ray beam intensity. For electron yield measurements the sample is also enclosed by a biased nonmagnetic cage which is used to pull the photoelectrons away from the sample. The sample current I is directly measured with a picoammeter. The sample is positioned in the homogeneous field of an electromagnet which is typically parallel to the X-ray propagation direction. The sample can be translated in the beam and rotated about the vertical axis

on the sample that is of the order of a few hundred micrometers in size. On their way to the sample the X-rays pass through a beam intensity monitor which consists of a metal grid surrounded by a wire cage, both made from nonmagnetic materials and coated with a material, often chosen to be Au, that has no prominent absorption edges in the spectral range of interest. The grid inside the cage is chosen to have a large number of fine metal wires within the beam diameter to minimize intensity changes with beam drifts, and typically absorbs about 20% of the incident X-rays. The cage consists of a coarser grid and is positively biased (∼+20V) to pull off the photoelectrons from the grid inside. The electron current (of order nA) flowing back to the grid from ground is measured with a picoammeter and it serves as the beam intensity signal I_0.

The sample is positioned in the center of an electromagnet or superconducting magnet, with the field axis typically aligned along the horizontal beam direction. The sample can be rotated in the beam about a vertical axis. If the

sample is in the form of a thin film the transmission is measured with a suitable detector like a photodiode that is positioned behind the sample, outside the magnet. It is most common, however, to simply measure the photocurrent of the sample with a picoammeter. Again a biased metal cage around the sample is used to pull of the photoelectrons from the sample. The biased cage has another benefit in that it minimizes the effect of the magnetic field on the measured sample current. When circular dichroism spectra are recorded with fixed photon spin by switching the field direction in the electromagnet, it is best to switch the field at every energy point in the dichroism spectrum. This eliminates effects due to beam instability. The switching typically takes of the order of 1 s and one only counts when the new field has been established. By adjusting the bias voltage of the grid, one can make the signals for the two field directions nearly the same, i.e., minimize the effect of the field on the signal.

A more versatile experimental configuration uses a magnet with variable field directions, as the octopole magnet implemented by Arenholz and Prestemon [432], shown in Fig. 10.5 and described in the caption. The magnetic field with a strength of 0.8 T can be oriented into a random direction, but is

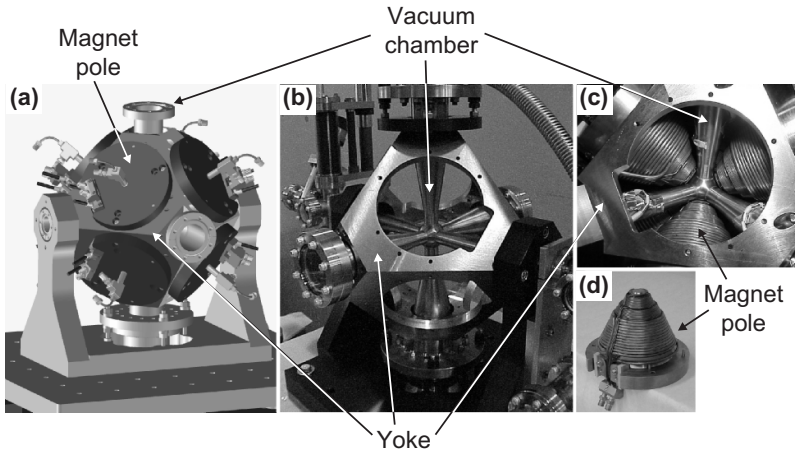

Fig. 10.5. Octopole magnet for the generation of an arbitrary field direction [432]. (**a**) shows a design drawing with an identification of the main components, the Ti-alloy vacuum chamber, the steel box yoke, and the magnetic poles with water cooling circuits. The photographs (**b**)–(**d**) show the manufactured and partly assembled components in more detail. The vacuum chamber is a six cross with vacuum flanges and a spherical center chamber of about 5 cm diameter. The shared steel yoke holds all eight magnetic poles and provides flux closure. The eight pole design offers better field uniformity in the center (below 1%) and larger fields than a six pole design, which in principle would be sufficient. The pole pieces are surrounded by the magnet coils and on the outside by three parallel water cooling circuits to avoid overheating

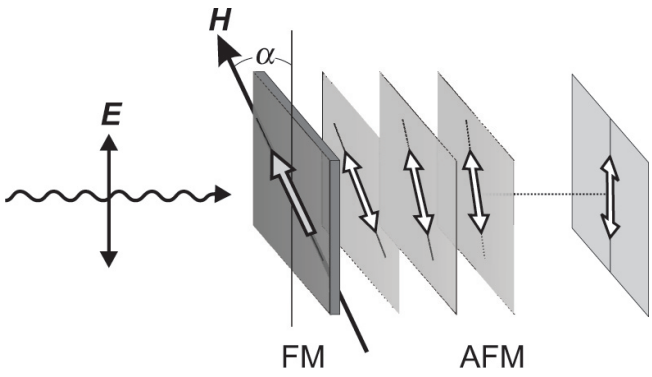

Fig. 10.6. Winding up of an antiferromagnetic exchange spring. An external magnetic field is used to rotate a ferromagnetic (FM) layer that is exchange coupled to an antiferromagnet (AFM). If the antiferromagnet is soft, its antiferromagnetic axis near the FM–AFM interface follows the rotation of the ferromagnetic magnetization. Deep in the bulk the axis remains unchanged. Thus an antiferromagnetic wall is formed that consists of a spring-like twist of the AFM axis by an angle α. This has been observed for Co/NiO by X-ray magnetic linear dichroism spectroscopy [405] using the octopole magnet in Fig. 10.5. The incident X-ray polarization $\boldsymbol{E}$ was fixed and the magnetic field direction $\boldsymbol{H}$ could be rotated relative to $\boldsymbol{E}$. By use of EY detection only the rotated fraction of the antiferromagnetic domain wall near the interface is observed

typically aligned either along the beam direction or along the horizontal or vertical directions perpendicular to the beam.

An octopole magnet is ideally suited for X-ray magnetic linear dichroism measurements. An example of such an experiment is schematically shown in Fig. 10.6. Without discussing the details of the experiment which can be found elsewhere [405], we only show the concept and the results. The experiment was conducted to prove the conjecture of the *Mauri model* of exchange bias [433] that an antiferromagnetic wall is formed at the ferromagnet–antiferromagnet interface when the ferromagnet is rotated in an external magnetic field. By fixing the direction $\boldsymbol{E}$ of the incident linearly polarized light, the experiment measured the orientation of both, the ferromagnetic magnetization and the antiferromagnetic axis near the interface, as a function of the orientation of the magnetic field vector $\boldsymbol{H}$ relative to the $\boldsymbol{E}$-vector. The magnetic linear dichroism effect in NiO revealed that the AFM axis indeed followed the rotation of the ferromagnetic Co magnetization, and therefore an exchange spring is wound up with one end coupled to the FM and the other end anchored deep in the bulk. The use of EY detection assured that only the rotating spin region in the AFM near the FM–AFM was observed.

10.3.3 Quantitative Analysis of Experimental Absorption Spectra

The quantities $\ln(I_0/I_t)$ obtained from a transmission measurement and I_e/I_0 from an EY experiment are called *X-ray absorption spectra*. Their intensity is directly proportional to the X-ray absorption coefficient or cross-section. In most cases, the sample thickness or the factors that determine the electron yield are not accurately known so that the spectral intensity is in arbitrary units. For the quantitative analysis of the spectra it is usually necessary to convert them into meaningful units. In doing so one uses the fact that, according to (10.1), for a given atom the measured intensity is proportional to $\mu_x d$ and therefore increases linearly with the number of atoms in the beam. Therefore also the *edge jump* of the absorption spectrum, defined as the difference of the *average* intensities well above and below the edge, depends linearly on the number of absorbing atoms.

By definition, the edge jump assumes that the absorption intensity changes by a sudden jump from a smooth curve below the edge to a smooth curve above the edge, as observed for the X-ray absorption spectra of atoms [189]. As an example we show in Fig. 10.7 the *atomic cross-sections* around the L-edges of the $3d$ transition metals taken from the Henke–Gullikson tables [362, 363].

We see that each atom has its characteristic edge jump, whose value is separately shown as circles, connected by a gray line. The cross-sections are simply obtained by extrapolating the ones measured at higher energy, outside the resonance region, into the near edge region and therefore do not account for the "white-line" resonance structure due to bonding. It is therefore common in the analysis of X-ray absorption spectra to proceed as follows.

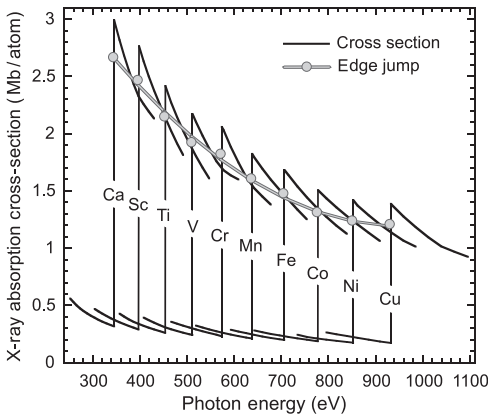

Fig. 10.7. Atomic cross-sections and L-edge jumps (L_3 plus L_2) for the $3d$ transition metals taken from the Henke–Gullikson tables [362,363]. Note that the *atomic* cross-sections simply extrapolate the values determined well above the edge into the near edge region and therefore all resonance effects due to bonding are absent

In the *analysis of X-ray absorption spectra* one distinguishes the intensities of *resonance structures* or "white lines" at the absorption thresholds which is sample and bonding-specific from the *atomic-like nonresonant background*. The smooth atomic-like background is independent of the atomic environment and is available as tabulated atomic X-ray absorption cross-sections.

The atomic edge jump picture still holds for bonded atoms if the core electrons are excited to continuum states that lie significantly higher in energy than any bonding (antibonding) orbitals. When the absorption spectrum of a given atom is measured in different environments like the gas phase, in a liquid or in different solids, the fine structure of the absorption edge will greatly change due to the atomic environment, yet for the same number of atoms in the X-ray beam the intensity outside the resonance region will be smooth and its value will be independent of bonding. This is illustrated schematically in Fig. 10.8.

Since the edge jump is proportional to the number of absorbing atoms we can renormalize the measured spectra for a given atom in different samples to a per atom basis by simply scaling and fitting them below the edge and well above the edge to the atomic cross section. We can make the following general statement that underlies different analysis methods of X-ray absorption spectra.

By renormalizing the measured absorption spectra of a given atom in different samples to the same *edge jump* one obtains spectra that correspond to the same number of absorbing atoms.

Absolute X-Ray Absorption Cross Sections

In practice, one rarely determines the *absolute* x-ray absorption cross section of a sample. If needed, one simply fits experimental spectra to the Henke–Gullikson cross-sections [362, 363] outside the resonance region where the cross section is smooth and atomic like. Often, experimental spectra have some background slope which is adjusted to match the slope of the tabulated atomic cross-section. The method is illustrated in Fig. 10.9a for the absorption spectrum of $LaFeO_3$ [406], which exhibits a large resonance intensity superimposed on a small edge jump. Once the region before and above the edge are properly fitted the resonance intensities are automatically obtained in the proper cross-section units.

For electron yield spectra, which may contain saturation effects in the resonance region, one exploits the fact that saturation effects are generally negligible before and above the edge, because in these regions the X-ray absorption length is much larger than the electron sampling depth (see Table 10.2). The

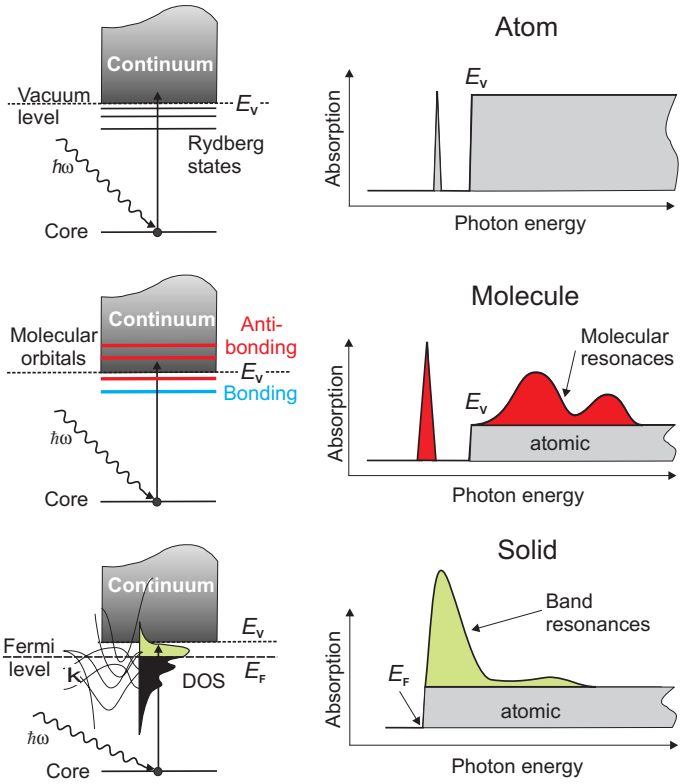

Fig. 10.8. Characteristic X-ray absorption spectra of an atom, the same atom in a molecule and the same atom in a solid, assumed to be a metal. For an atom the lowest energy resonances correspond to transitions to Rydberg states [189], which merge into a step-like structure at the core electron ionization potential (IP), corresponding to transitions from the core shell of interest to states just above the vacuum level (E_V). For a molecule transitions to unfilled orbitals result in pronounced resonances as shown. For atoms embedded in a metal the lowest energy transition correspond to states just above the Fermi level (E_F). The X-ray absorption intensity follows the Brillouin zone (k) integrated density of states (DOS). In all cases resonant transitions to specific electronic states are superimposed on smooth atomic-like cross-sections given in the Henke–Gullikson tables [362,363]. In the analysis one assumes that the *atomic* cross-sections well above the "edge" can be simply extrapolated to lower energies, with a step like onset that is positioned either at E_V or E_F [189] or, for solids, at the position of the first resonance [96]

converted EY spectra do, however, still contain saturation effects in the resonance region. They can be eliminated if the electron sampling depth λ_e is known [406,426–431]. This is illustrated in Fig. 10.9 for $LaFeO_3$, where $\lambda_e = 20$ Å. The saturation effects are seen to be quite large in this case due to the large resonant cross-section (short λ_x), and the fact that the *effective* X-ray penetration depth perpendicular to the surface is further shortened to $\lambda_x \sin 20°$, since the spectrum was recorded at a 20° grazing X-ray incidence angle from the surface.

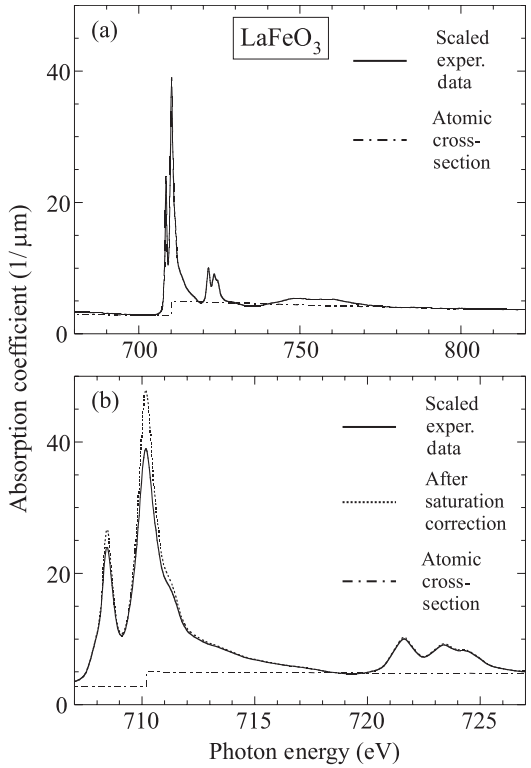

Fig. 10.9. (**a**) Illustration of converting the measured electron yield spectrum of $LaFeO_3$ (*solid line*) into an absolute X-ray absorption coefficient. The spectrum is fitted outside of the resonance region to the calculated absolute atomic absorption coefficient (*dashed-dotted line*) taken from the Henke–Gullikson tabulation [362,363]. The experimental spectrum was measured at a grazing X-ray incidence angle of 20° from the surface plane. (**b**) Enlarged $L_{2,3}$ region of (**a**). Here we also show the saturation corrected electron yield spectrum as a *dotted line*. Spectra taken from Lüning et al. [406]

Relative Absorption Cross Sections: Edge-Jump Normalization

In many cases one is simply interested in the relative intensities of absorption resonances or dichroic differences. Then the determination of absolute x-ray absorption cross sections can be avoided, and one uses a simple method which goes as follows. One measures two samples, one with known and one with unknown properties, in exactly the same way. If the two spectra have a different average slope with photon energy one approximately matches the slopes. Then a background is subtracted so that the region before the absorption edge has zero intensity. One then simply multiplies the spectra by constants to make the *edge jump* the same in both spectra. They now correspond to the same number of atoms in the beam, without knowing their number. All we know is that the chosen number for the edge jump corresponds to the same number in both spectra. One can now compare the relative intensities of the resonance structures in the spectra.

For example, we shall see below that the L-edge resonance structures in the magnetic 3*d* transition metals show a large magnetic dichroism effect that is proportional to the magnetic moment per atom. If we wanted to know the size of the magnetic moment in a sample of interest, say one that contains Co, we would take a dichroism spectrum of this sample and compare it to that of Co metal, where we know the magnetic moment per atom. We would normalize both experimental spectra in an identical fashion to the same edge jump, and then compare the size of the resonant dichroism effects in the two samples. This would allow us to determine the unknown magnetic moment per atom by comparison of the two dichroism effects.

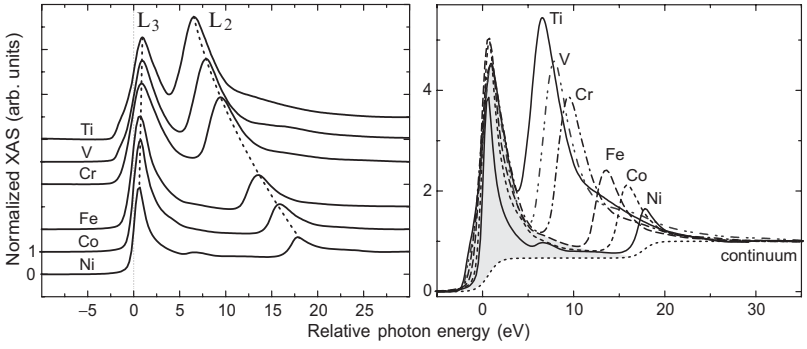

Fig. 10.10. Polarization averaged X-ray absorption spectra for Ti, V, Cr, Fe, Co, and Ni metal [434]. The spectra are normalized to the same unit edge jump for easier comparison. Spectra on the *left* are vertically offset

10.3.4 Some Important Experimental Absorption Spectra

Fig. 10.10 shows the L-edge X-ray absorption spectra of some important 3*d* transition metals [434]. The spectra are normalized to the same unit edge jump

for easy comparison of the separation between the L_3 and L_2 resonances. While for the "heavy" $3d$ metals Fe, Co, and Ni the spin–orbit splitting of the $2p$ core electrons is significant larger than the width of the associated white line resonances, for the light $3d$ metals the splitting decreases and the width increases. As illustrated in Fig. 9.26, the comparable size of the spin–orbit coupling and the intraatomic correlation energy will then lead to a mixing of absorption channels leading to the observed resonances. This leads to complications in the determination of spin magnetic moments [435, 436] which is based on the separate analysis of the two $3d \rightarrow 2p_{3/2}$ and $3d \rightarrow 2p_{1/2}$ excitation channels, as illustrated in Fig. 9.16.

Because of the importance of the $3d$ transitions metals and their oxides we show in Fig. 10.11 the properly normalized X-ray absorption spectra of the magnetic $3d$ transition metals and their oxides. We have plotted the X-ray absorption coefficient in units of μm^{-1} as a function of energy. These spectra form the basis for much of the dichroism work discussed in the rest of the book. Comparison of the spectra in Fig. 10.11 shows the rich resonance fine structure

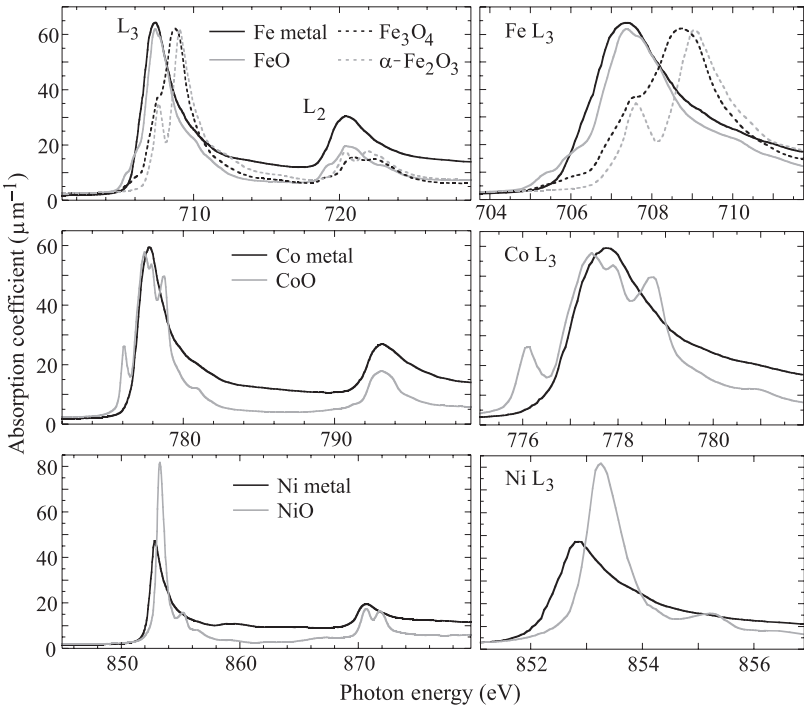

Fig. 10.11. Polarization averaged X-ray absorption spectra for Fe, Co, and Ni metal and their oxides [431]. The spectra are plotted in absolute intensity units of the X-ray absorption coefficient. The rich fine structure of the oxide spectra is due to multiplet effects

in the near edge region. This *chemical sensitivity* allows the identification of different bonding environments for a given atom. Besides the *atomic specificity* of X-ray absorption indicated by the greatly different L-edge positions of Fe, Co, and Ni, the chemical specificity and the later discussed *magnetic specificity* constitute three important cornerstones of the X-ray absorption technique.

Magnetic dichroism spectroscopy offers:

- *Atomic specificity* through the energy separation of characteristic X-ray absorption edges.
- *Chemical sensitivity* through the resonant fine structure at a given atomic absorption edge.
- *Magnetic specificity* through the polarization dependence of the near-edge fine structure.

The rich fine structure in the oxide spectra is due to so-called multiplet splitting. As discussed in more detail in Sect. 9.7.8, the detailed splitting depends on three main quantities, the ligand field symmetry, the valency of the atom, and spin configuration of the electronic ground state.

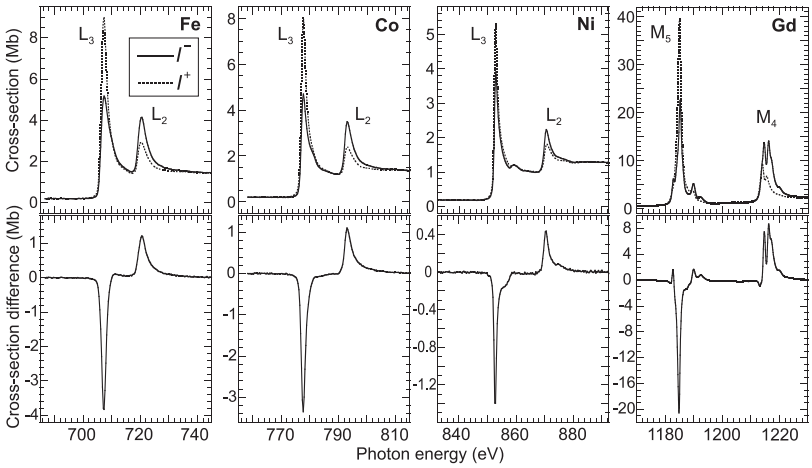

Fig. 10.12. XMCD spectra for the elemental ferromagnetic metals, corrected to correspond to 100% circularly polarized X-rays. The data for Fe, Co, and Ni are from Chen et al. [96, 375], those for Gd are from Prieto et al. [356]. The difference spectra shown underneath correspond to the convention $I^- - I^+$ of (9.95)

10.3.5 XMCD Spectra of Magnetic Atoms: From Thin Films to Isolated Atoms

Data for the four elemental ferromagnets, Fe, Co, Ni [96, 375] and Gd [356], are shown in Fig. 10.12. In all cases, the shown data correspond to maximum

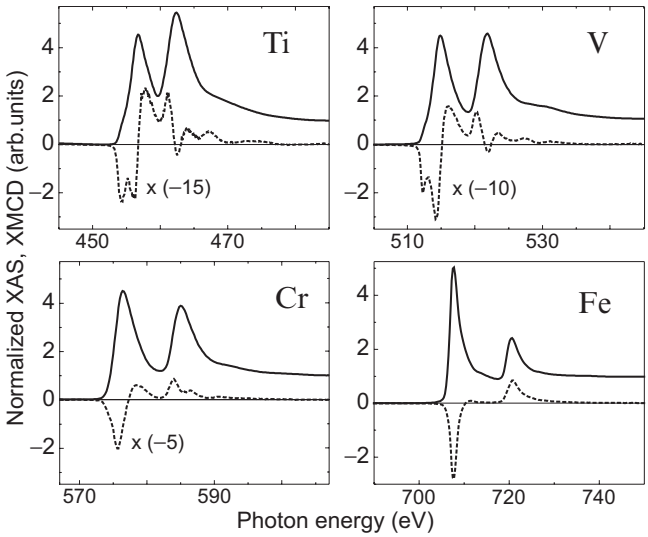

Fig. 10.13. Angle-averaged L-edge X-ray absorption spectra (*solid lines*) for thin metal layers of Ti, V, Cr deposited on Fe and the corresponding dichroism spectra (*dashed*) [434]. The data were corrected for incomplete polarization and saturation effects. The Ti, V, and Cr layers are magnetic through proximity effects, i.e., induced magnetism. Their coupling to Fe is antiparallel as revealed by the sign of the original dichroism spectra. In our plot the dashed XMCD spectra for Ti, V, and Cr have been inverted to avoid overlap of the XAS and XMCD traces. All plotted intensities correspond to a unit edge jump normalization in the original spectra

dichroism effect (100% polarization and alignment of the photon spins and sample magnetization), and we have also plotted the data for the same relative orientations of photon spins and sample magnetization. The more complicated spectrum for Gd is due to multiplet splitting, the origin of which was discussed in Sect. 9.7.8.

The sensitivity of XMCD to small magnetic moments is illustrated in Fig. 10.13. Here we have plotted the absorption and XMCD spectra of Fe and compared it to absorption and dichroism spectra for thin films of Ti, V, and Cr deposited on an Fe substrate. The small dichroism in the Ti, V, and Cr spectra, indicated by the listed multiplicative factors, is due to induced magnetic moments caused by the adjacent Fe layer. Note that we have plotted inverted dichroism (difference) spectra (dashed lines) for the cases of Ti, V, and Cr to avoid overlap of the solid and dashed curves. Since in the original Ti, V, and Cr data the dichroism effects (the dashed spectra) were upside down from those shown in Fig. 10.13, comparison to the spectrum of the Fe standard shows that in all cases the magnetization in the deposited thin films is opposite to that in the Fe substrate.

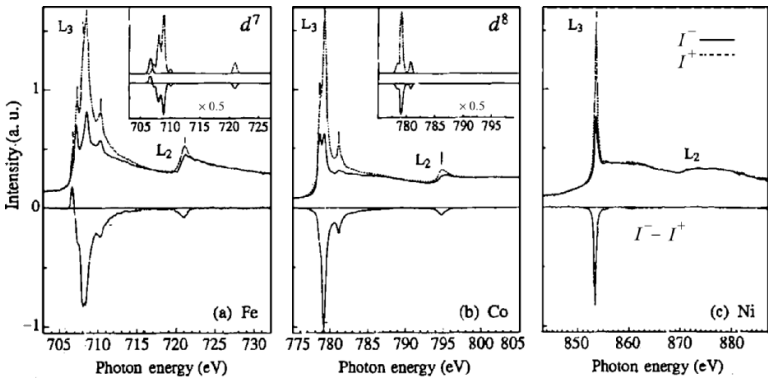

Fig. 10.14. XMCD spectra for isolated $3d$ impurities deposited on K films, corresponding to coverages of 0.015 monolayer for Fe, 0.015 monolayer for Co, and 0.004 monolayer for Ni [437]. The spectra were recorded at 10 K in fields up to ± 7 T. The insets show the spectra calculated for the d^7 and d^8 atomic configurations [438] with the energies renormalized to match the experimental ones

The metal spectra are seen to exhibit rather broad resonances. Only the dichroic difference spectra of the lighter atoms Cr, V, and Ti show significant fine-structure which is associated with multiplet effects. Such effects become pronounced for isolated Fe, Co, and Ni atoms deposited on K films as shown in Fig. 10.14 [437].

The spectra were recorded at 10 K, and fields up to ± 7 T were used to align the atomic moments. The presence of multiplet structure clearly shows the localized character of the $3d$ electrons in the atoms. The multiplet structure serves as a sensitive fingerprint of the electronic ground state configuration which can be determined by comparison of the experimental spectra to those calculated by atomic multiplet theory [438]. The calculated spectra, shown as insets, correspond to $3d^n \rightarrow 2p^5 3d^{n+1}$ transitions assuming zero ligand field. The comparison of experiment and theory readily allowed the determination of the respective ground states d^7, $^4F_{9/2}$ for Fe, d^8, $^3F_4$ for Co and d^9, $^2D_{5/2}$ for Ni (see Table 7.1). These differ from the approximate configurations d^6 for Fe, d^7 for Co and d^8 for Ni in the metals (see Sects. 7.3 and 12.2.2). In fact, prior to the XMCD measurements there had been considerable debate as to the electronic ground state configuration.

The measured XMCD effects are larger than in the bulk metals and show very different ratios of the L_3 and L_2 dichroism intensities and opposite signs. In particular, the L_2 dichroism for Ni is zero. The latter is understood from the ground state configuration d^9, $^2D_{5/2}$, which does not allow L_2-edge transitions, which in a configuration picture correspond to $J = 5/2 \rightarrow J = 1/2$ and thus violate the dipole selection rule.

10.3.6 Sum Rule Analysis of XMCD Spectra: Enhanced Orbital Moments in Small Clusters

In Sect. 10.3.5 we have discussed the XMCD spectra of the ferromagnetic transition metals Fe, Co, and Ni in comparison to those of the isolated atoms, aligned at low temperature in a strong magnetic field. Here we want to take a look at what happens in the transition region between isolated atoms and bulk metals. We shall see that the magnetic properties of small transition metal clusters are quite fascinating, indeed. Because the XMCD studies of interest required a quantitative determination of magnetic moments by application of the sum rules discussed in Sects. 9.6.5 and 9.7.9, we shall use this opportunity to also comment on practical aspects of the sum rule analysis in XMCD.

Today, quantitative analysis of XMCD spectra is often carried out by means of the method suggested by Chen et al. [96]. This method determines the ratios of the spin and orbital moments divided by the number of valence holes. Hence, in order to determine the magnetic moments, the number of valence holes needs to be known. In practice, this is almost never the case for samples of interest. It is for this reason that we discussed in Sect. 9.6.5 the combined use of three sum rules, which all depend on the knowledge of the constant C, which in turn is determined by the radial transition matrix element as expressed by (9.91). The results shown in Fig. 9.17 demonstrate, that for elements with similar atomic number Z, like Fe, Co, and Ni, C is roughly constant. This fact has been utilized, for example, in the determination of the magnetic moment of Cu atoms in Co/Cu and Fe/Cu multilayers [315, 439], where in the analysis of the Cu XMCD spectra the average constant C for Fe, Co, and Ni was used.

The most robust and accurate method of determining magnetic moments is therefore typically the use of a reference sample with known moments, like the elemental ferromagnetic metals, and transfer of the constant C to the analysis of the sample of interest. This method has been successfully used to determine the orbital magnetic moments in small Co clusters and low dimensional structures [440, 441], with the results calibrated by comparison to bulk Co metal.

As shown in Fig. 3.9 small metal clusters in molecular beams show the expected increase in the total magnetic moment toward atomic values. One particularly interesting question is what role the orbital magnetic moment plays in the enhancement of the total moment. In fact, based on our discussion on the quenching effects of the ligand fields in Sect. 7.9 one might expect substantial enhancement of the orbital moment in clusters due to reduced coordination of the surface atoms. This is indeed found [440–442].

As an example we show in Fig. 10.15 the XMCD results for Co atoms on a Pt(997) surface in the form of monatomic chains, a monolayer and a thick Co film. For atoms in low-symmetry environments, the application of the spin sum rule given by (9.133) is complicated by the presence of the anisotropic spin density term m_{D}^{α} [410, 411]. In contrast, the orbital moment can be directly

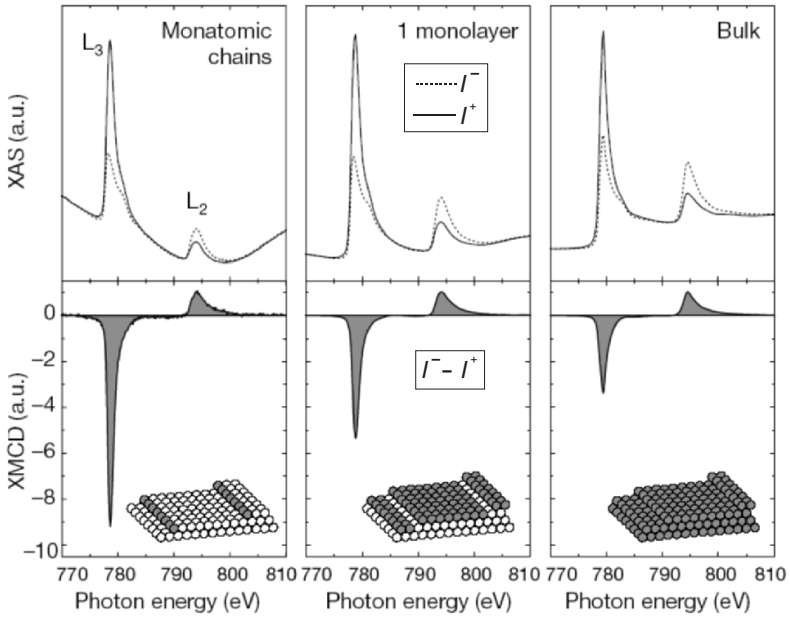

Fig. 10.15. Co L-edge X-ray absorption and dichroism spectra for, from left to right: monatomic chains, a monolayer and a thick Co film, all grown on Pt(997) [440]. Spectra are shown for parallel (I^+) and antiparallel (I^-) directions of X-ray helicity and field-induced magnetization. The dichroism signal ($I^- - I^+$) is obtained by subtraction of the absorption spectra in each panel and normalization to the intensity of the L_2-edge dichroism peak. Spectra were recorded in the electron-yield mode at $T = 10$K and $B = 7$T. Because of the low Co coverage, the edge structures of the monatomic wires are superimposed to a strong background. Changes in the L_3 XMCD intensity indicate that the orbital moment is substantially increased in going from bulk Co to a 2D Co monolayer and to the 1D chains

determined along the applied field direction. The spectra shown in Fig. 10.15 were recorded in the electron-yield mode at $T = 10$K and $B = 7$T. According to the orbital moment sum rule (9.134), the orbital magnetic moment is zero if the L_3 and L_2 dichroism intensities A and B have the same size but opposite signs. By normalizing the dichroism spectra to the L_2-edge intensity (peak B in Fig. 9.16), one can therefore conveniently see changes in the orbital moment, as illustrated at the bottom of Fig. 10.15.

We have summarized in Table 10.3 results for various types of Co structures on Pt, taken from work by Gambardella and collaborators [440, 441].

These results clearly show the strong dependence of the orbital magnetic moment on coordination. As expected, the orbital moment increases strongly with decreasing size or dimensionality of the Co structures. For a Co adatom

Table 10.3. Orbital magnetic moments $\langle L_z \rangle$ for various Co/Pt systems, measured by XMCD along the easy axis and values for the magnetocrystalline anisotropy constant K_1 determined from directional magnetization loops. The results were taken from work by Gambardella and collaborators [440, 441]

System	$\langle L_z \rangle$ [μ_B]	K_1 [meV/atom]
Co metal (hcp)	0.14	0.053
Co/Pt(997) ML	0.31	0.14 ± 0.01
Co/Pt(111) ML	0.29	
Co/Pt(997) chain	0.68 ± 0.05	2.0 ± 0.2
Co/Pt(111) adatom	1.1 ± 0.1	9.3 ± 1.6

on Pt it has a value of more than 1 μ_B and becomes comparable to the spin moment ($1.7\mu_B$) in bulk Co metal. This indicates that the enhancement for the total moment in Fe, Co, and Ni clusters with decreasing cluster size, seen by the Stern–Gerlach experiments on cluster beams [127] shown in Fig. 3.9, must be partly or even largely due to an orbital moment enhancement.

For Co structures on Pt, the increase in orbital moment is accompanied by an increase of the magnetocrystalline anisotropy (MCA) energy K_1, also listed in Table 10.3. It was derived from angle-dependent XMCD magnetization loop measurements and corresponds to the element specific MCA of Co in the various samples. For the monolayer and isolated adatoms of Co on Pt(111) the easy axis was found to be perpendicular to the surface and for the individual adatoms the MCA had a huge value of $K_1 = 9.1$meV per Co atom. This should be compared to the values found for the hardest thin film materials, e.g., Co/Pt multilayers with $K_1 \simeq 0.3$ meV per Co atom or bulk materials such as $SmCo_5$ with $K_1 = 1.8$ meV per atom [40, 443] or the ordered $L1_0$ phase of CoPt with $K_1 = 0.8$ meV per Co atom [443]. For Co on Pt(997), the Co monolayer had an out-of-plane easy axis and for the Co chains the easy axis was perpendicular to the chain at an angle of 43° from the sample normal. The observed easy axis orientation perpendicular to the chain axis agrees with earlier tight binding calculations for monoatomic Co chains on Pd [444]. These calculations showed the transition of the easy axis from along the chain axis for free monoatomic Co chains to a perpendicular orientation when the chains were placed on Pd.

The above experiments beautifully demonstrate the dependence of the magnetic properties on the dimensionality of the magnetic materials. For more information on low-dimensional magnetic systems we refer the reader to reviews by Bader [39,445] and Himpsel [250]. One particular strength of XMCD measurements in such systems is clearly the elucidation of the role of orbital magnetism. In addition to the studies reported here many beautiful studies of such systems have been performed by XMCD [325, 328, 442, 446–453]. The experiments also demonstrate the extreme sensitivity of XMCD. For example, the studies of isolated Co adatoms on Pt(111) [441] corresponded to a

coverage of 0.010 monolayers of Co or 1.5×10^{13} Co atoms per cm^2 or about 10^9 Co atoms in the X-ray beam.

10.3.7 Measurement of Small Spin and Orbital Moments: Pauli Paramagnetism

We conclude the spectroscopy section of this chapter by discussing the use of XMCD spectroscopy to determine truly small magnetic moments. With improvements of the experimental techniques of XMCD spectroscopy, one question that naturally arises is as to the ultimate sensitivity of the technique. How small a magnetic moment can be measured? Of course, the answer to this question depends on the system to be studied. Nevertheless, the following experiment provides a nice demonstration of the capabilities of XMCD in this direction.

We have seen in Sect. 10.3.5 above that we can magnetically align isolated paramagnetic atoms like Fe, Co, and Ni by use of a low temperature and a large magnetic field. This is also possible for paramagnetic metals. When cooled to low temperature and exposed to a large magnetic fields H, they actually

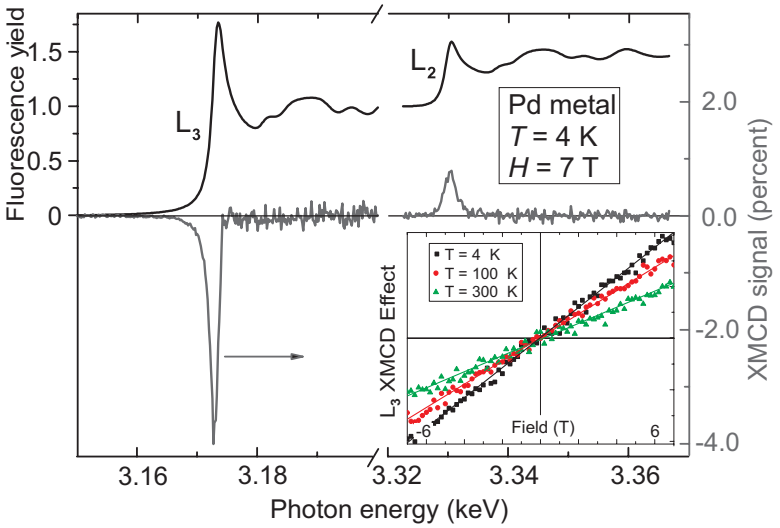

Fig. 10.16. $PdL_{2,3}$ X-ray absorption spectra (*top*) and XMCD difference spectra (*bottom*) of a Pd single crystal, recorded at $T = 4$K and in an applied field of 7 T. Spectra are corrected for self-absorption and incomplete circular polarization. Inset: Magnetization curves of Pd metal recorded at 4, 100, and 300 K by monitoring the PdL_3 XMCD signal. Figure courtesy of A. Rogalev [88]

acquire an induced magnetization M. The associated small susceptibility $\chi = M/\mu_0 H$ is found to be temperature independent, and this situation is referred to as *Pauli paramagnetism*, as discussed more in Sect. 15.3. Estimates carried out in that sections show that the expected moment is quite small, of order of $10^{-4}\mu_B$ per atom.

This small moment has indeed been measured in Pd metal using XMCD spectroscopy by Rogalev and collaborators [454], as shown in Fig. 10.16, despite the rather poor degree of circular polarization of only 12% at the L_3-edge and 22% at the L_2-edge available on the used beam line.

After correction of the data for incomplete circular polarization, the XMCD effect is in fact quite large as shown by the right side scale in Fig. 10.16, of order 4% at the L_3-edge and 1% at the L_2-edge. Sum rule analysis of the data gives a spin magnetic moment of $\approx 0.012\mu_B$ and an orbital magnetic moment of $\approx 0.004\mu_B$, under the conditions of the experiment, $T = 4\,\mathrm{K}$ and in an applied field of 7 T. The presence of an orbital moment shows, that in addition to the Pauli spin paramagnetism the system also exhibits an orbital susceptibility, as suggested by Kubo and Obata [455]. The inset in Fig. 10.16 shows that the measured susceptibility is nearly temperature independent over the 4–300 K range. This confirms that the measured effect is indeed largely due to the Pauli susceptibility. The slope of the curve gives a total paramagnetic susceptibility of the 4*d* electrons in Pd of $\approx 1.4 \times 10^{-4}$.

10.4 Magnetic Imaging with X-rays

Before we discuss the use of X-rays for magnetic imaging let us briefly take a look at the field of magnetic imaging, in general. One milestone is the 1998 book by Hubert and Schäfer [54] which gives a review of magnetic domains and magnetic imaging. Other valuable resources are the review by Freeman and Choi [456] and the book by Hopster and Oepen [457] which reviews advances in magnetic microscopies up to 2004. The latter book also contains articles by Scholl et al. and Kuch et al. on magnetic imaging by X-rays. The present section should be viewed against the backdrop of all the knowledge that has been accumulated over the years.

It is our goal to provide an overview of the prominent X-ray based imaging methods and to present illustrative examples of their unique power. Like other techniques, X-rays have their specific strength and weaknesses. It will become clear that spatial resolution is only one important asset of magnetic microscopy techniques. In this respect X-rays take second place behind other techniques such a spin-polarized scanning tunneling microscopy [458]. However, they offer capablities not afforded by other techniques, in particular, elemental and chemical state specificity, variable sampling depth, and the capability to follow ultrafast processes on the picosecond scale.

X-ray magnetic microscopy is based on the dichroism effects already discussed in Sect. 10.3. When the photon energy is tuned to a prominent reso-

nance in the X-ray absorption spectrum, like the L_3 or L_2 edges in the transition metals or the M_5 or M_4 edges for the rare earths, a large dichroism effect exists for magnetic materials. In general, this effect depends on the orientation of the photon polarization relative to the magnetic orientation. For XMCD we have a $\cos\theta$-dependence of the dichroism intensity on the angle θ between the photon angular momentum and the sample magnetization, expressed by (9.100). For XMLD we have a $\cos^2\theta$ dependence according to (9.123), where θ is the angle between the $\boldsymbol{E}$-vector and the magnetic axis. It is the X-ray polarization in conjunction with the tunable photon energy that forms the basis for X-ray magnetic imaging. Because of the utilization of these spectroscopy concepts one often speaks of X-ray spectromicroscopy.

It is quite easy to understand the origin of the magnetic contrast. Let us assume that we tune the photon energy to a resonance and fix the photon polarization. If now the sample contains microscopic regions with different magnetic orientations then the signal from these regions will vary because of the dichroic absorption effect. In a transmission experiment, some regions will absorb less and others more, depending on their orientation in the beam. In an electron yield experiment the number of photoelectrons will also be different from the differently oriented regions in the beam. The different signal strength can therefore be used as a contrast mechanism for microscopy. We have seen that we can expect the signal to vary by as much as 20–30% depending on the magnetic orientation. This is indeed a very large contrast considering that Kerr microscopy works with contrasts of less than 1%. All we have to figure out is how to separate the signals from the microscopic areas of the sample by some kind of microscopy technique. We shall first discuss three real space microscopy techniques and then, in Sect. 10.4.1, a technique based on reconstructing a real space image from a coherent X-ray scattering pattern.

10.4.1 X-ray Microscopy Methods

Similar to electron microscopy there are two main approaches, either based on scanning or imaging methods. Three common experimental implementations based on X-rays are illustrated in Fig. 10.17 and we shall now discuss them in turn.

Scanning Transmission X-ray Microscopy – STXM

In scanning X-ray microscopy, illustrated in Fig. 10.17a, a monochromatic X-ray beam is focused to the smallest possible spot size and the X-ray intensity transmitted through the sample is monitored as a function of the focused beam position on the sample [459]. In principle, either the sample or the beam position may be scanned but in practice one typically scans the sample. One may also measure the fluorescent X-ray or electron intensity from the sample, as indicated in the figure, but measurement of the transmitted intensity is most

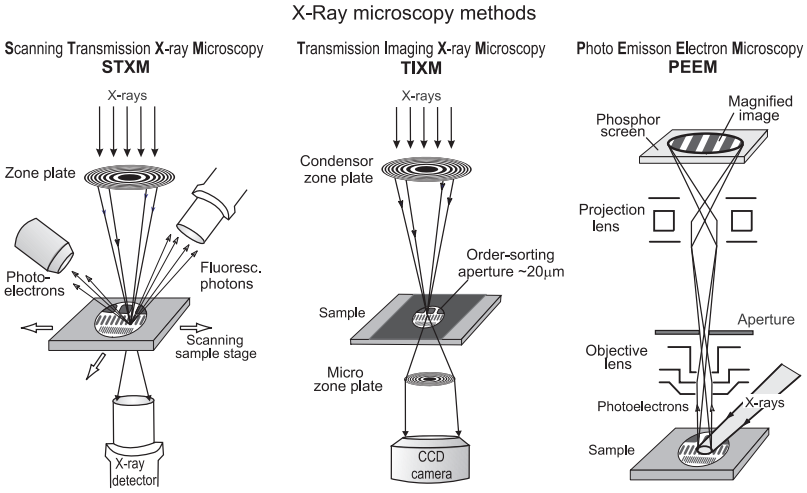

Fig. 10.17. Schematic of three X-ray microscopy methods for imaging of nanoscale magnetic structures. (**a**) In scanning transmission X-ray microscopy, STXM, a monochromatic X-ray beam is focused to a small X-ray spot by a suitable X-ray optic, e.g., a zone plate as shown, and the sample is scanned relative to the X-ray focal spot. The spatial resolution is determined by the spot size which is determined by the width of the outermost zones in the zone plate. The intensity of the transmitted X-rays or the fluorescence or electron yield from the sample are detected as a function of the sample position and thus determine the contrast in the image. (**b**) In transmission imaging X-ray microscopy, TIXM, the incident beam may be either monochromatic or not. The beam is focused by a condensor zone plate that in conjunction with a pinhole before the sample produces a monochromatic photon spot on the sample. For an incident polychromatic beam the energy resolution is determined by the zone plate and the pinhole and is typically not very high ($E/\Delta E \approx 200$). A microzone plate generates a magnified image of the illuminated sample area which can be viewed in real time by a X-ray sensitive CCD camera. The spatial resolution is determined by the width of the outermost zones in the microzone plate. (**c**) In X-ray photoemission electron microscopy, XPEEM, the X-rays are focused by a shaped mirror to match the field of view of an electron microscope (1–50 μm). Electrons emitted from the sample are imaged by an assembly of electrostatic or magnetic lenses with magnification onto a phosphor screen, and the image can be viewed in real time at video rates. The spatial resolution is determined by the electron optics within the microscope, the size of the aperture, and the operation voltage. In advanced designs an energy filter is employed to minimize chromatic abberation effects and such effects are further reduced by aberration correcting optics

common. In this approach the energy resolution is given by the monochromator in the beam line (not shown) and the spatial resolution is determined by the size of the X-ray spot.

Small X-ray spots can be obtained by using the reflected and focused beam from grazing incidence mirrors or the diffracted and focused beam from either a multilayer mirror or a zone plate. In practice, zone plate focussing, shown in Fig. 10.17a yields the smallest spot sizes. The focal spot size is determined by the width of the outermost zones of the zone plate and today the resolution is typically about 30 nm with resolutions down to 10 nm or less expected in the future [460]. Because the focal length of the zone plate lens changes with photon energy, for spectroscopic studies the sample position also needs to be scannable along the beam direction. X-ray transmission or fluorescence microscopies are well suited for studies in the presence of a magnetic field, contrary to electron based methods. They are "bulk" sensitive, in the sense that the transmitted intensity is determined by the entire thickness of the sample.

Transmission Imaging X-ray Microscopy – TIXM

From an instrumental point of view, transmission imaging X-ray microscopy or TIXM, shown in Fig. 10.17b is closely related to scanning X-ray microscopy since in both cases the spatial resolution is determined by zone plates and both are photon-in/photon-out methods. First generation microscopes used polychromatic beams which were focused and monochromatized by a combination of a condenser zone plate and a pinhole aperture (typically 10–20 μm diameter). In such an arrangement the energy resolution is determined by the zone plate dimensions and the pinhole size and is typically $\Delta E/E \simeq 1/250$. Modern microscopes use a monochromatic incident beam with $\Delta E/E \simeq 1/5{,}000$ which also allows spectroscopic studies of the detailed near-edge fine structure.

The beam is focused onto the sample by means of a condenser zone plate. The focal spot size then serves as the field of view of the imaging process, accomplished by a microzone plate that generates a magnified image of the illuminated area on the sample onto a phosphor screen or X-ray sensitive CCD camera. The spatial resolution is determined by the width of the outermost zones of the microzone plate [460] and a resolution of 15 nm has been obtained [461]. Spectroscopic studies require movement of both the condensor and microzone plates relative to the sample, and in practice, this has impeded spectroscopic studies with TIXM. Like STXM, TIXM is also well suited for studies in the presence of magnetic fields, and such studies have been performed by Fischer et al. [462, 463].

X-ray Photoemission Electron Microscopy – X-PEEM

The third imaging method is based on X-rays-in/electrons-out and was pioneered by Tonner [464]. It is illustrated in Fig. 10.17c. The sample is illuminated by a monochromatic X-ray beam that is only moderately focused, typically to tens of micrometers, so that it matches the maximum field of view

of a photoelectron microscope. The energy resolution is determined by the X-ray monochromator in the beam line and the spatial resolution is determined by the electron optics in the X-PEEM. It is limited by three quantities: spherical aberration, chromatic aberration, and diffraction. In practice, for X-ray excitation of electrons, chromatic aberrations dominate [464, 465]. They originate from errors in the focusing of electrons with different kinetic energies.

Most PEEM microscopes do not incorporate an energy analyzer or filter [466] and therefore, in principle, all photoelectrons are detected. In practice, the electron intensity is dominated, by orders of magnitude, by the secondary electron tail in the 0–20 eV kinetic energy range, where zero kinetic energy corresponds to the vacuum level of the sample [467]. The secondary electron intensity which closely follows the X-ray absorption spectrum of the sample [467], determines the X-PEEM intensity, and its large size provides a suitably large signal.

The energy spread of the inelastic tail (about 5 eV for most materials [468]) spoils the spatial resolution through chromatic aberrations. Fortunately, the effective width of the energy spread is reduced by a suitable aperture placed in the backfocal plane of the PEEM. The aperture acts as a filter for high energy electrons which are focused behind the aperture while the low energy portion of the inelastic tail is properly focused at the aperture position and is thus transmitted. Calculations show that a spatial resolution of about 20 nm can be obtained by X-PEEM because of the energy filtering effect of the aperture [469], and this is verified by experiments. Even better spatial resolutions are achieved when the energy spread of the emitted electrons is reduced. This situation is encountered when ultraviolet radiation is used with an energy slightly higher than the workfunction and a spatial resolution of 8 nm has been demonstrated [470]. In this case chromatic aberrations are strongly reduced by the narrow width of the secondary electron distribution. At X-ray energies, a resolution of 22 nm has been achieved by use of an energy filter to reduce the electron energy spread [471]. In the future lateral resolutions below 5 nm appear possible [472, 473].

Contrast Mechanisms

The intensity changes with photon energy or X-ray polarization discussed in the earlier spectroscopy section naturally lend themselves as contrast mechanisms for scanning and imaging X-ray microscopy. For example, if the photon energy is tuned to 707 eV, the L_3 resonance of Fe metal, the measured signal from the sample will emphasize Fe over other elements in the sample. If we change the polarization from linear to circular, Fe regions in the sample will be emphasized whose magnetization direction is parallel to the photon spin (see Figs. 9.12 and 10.1d). It is not necessary in many cases to change the photon spin in XMCD microscopy since the contrast is large and can be enhanced by combining images recorded at the L_3 and L_2 edges.

For antiferromagnets the photon energy of the linearly polarized light is tuned to a particular multiplet peak, e.g., one of the L_2-edge peaks in Fig. 10.1c. Domains with an orientation of the magnetic axis parallel to $\boldsymbol{E}$ will then show a different intensity than those with the axis perpendicular to $\boldsymbol{E}$. Again the contrast can be enhanced by combining images taken at different photon (multiplet) energies.

In addition to the spectroscopic contrast, other basic contrast mechanisms exist. In X-PEEM the electron yield from different sample areas is also determined by the local work function and topology. In transmission X-ray microscopy additional contrast arises from differences in the X-ray absorption coefficient at nonresonant photon energies caused by compositional changes or thickness variations of the sample.

10.4.2 Lensless Imaging by Coherent Scattering

We have seen that the resolution of real space X-ray microscopy techniques is determined by optics in the form of X-ray or electron lenses. Here we describe an alternative lensless imaging approach based on X-ray scattering, which in principle is resolution limited only by the X-ray wavelength.

It is well established that, in principle, X-rays may resolve structures down to the size of the X-ray wavelength, the so-called diffraction limit. Diffraction imaging, or crystallography, is a lensless approach where the real space structure is obtained by inversion of a reciprocal space diffraction pattern. This approach has been extensively used for decades to determine the structures of crystalline systems, consisting of repeated identical unit cells. The procedure relies on the remarkable fact that for typical experimental geometries X-ray beams are *coherent* over dimensions that are larger than the unit cell dimensions of the sample, despite the fact that all of today's X-ray sources, including undulators, are characterized by spontaneous emission and are therefore chaotic or incoherent by nature. A coherent beam can be created from the radiation emitted by an incoherent source by spectral and spatial filtering [109].[3] When a single crystal is inserted into an X-ray beam, its unit cell is typically so small that across its tiny volume the EM wave has a well defined phase relationship. Therefore the waves that are scattered off the individual atoms within each unit cell can interfere. Because all unit cells are identical, the unit cell interference patterns are identical and add up into intense diffraction spots.[4] The diffraction spot pattern can then be used to solve the crystal structure.

[3] More specifically, one distinguishes *temporal coherence*, which is determined by the bandwidth of the radiation and *lateral coherence* which is determined by the geometry perpendicular to the beam direction.

[4] When the EM field is quantized one finds that for today's X-ray sources all diffraction experiments are based on single photon interference effects because the coherence volume of the radiation contains less than one photon. This will change with the advent of X-ray free electron lasers.

The diffraction approach breaks down if the sample is nonperiodic since now the interference patterns from small areas in the sample are no longer identical and therefore intense diffraction spots will no longer exist. This situation is encountered in many systems that contain order on the nanoscale without long-range periodicity. A prominent example are magnetic domains which typically consist of irregular nanometer or micrometer sized areas in which the magnetization points in different directions. Despite their disordered arrangement it is still possible, however, to derive their real space arrangement from the scattered intensity as we shall discuss now.

In order to understand how this is possible we first consider the more familiar case of small angle X-ray scattering (SAXS), illustrated in the top half of Fig. 10.18. This well-established technique uses an X-ray beam which at the position of the sample is coherent only over a dimension, called the *coherence length*, of tens of nanometers. In Fig. 10.18 we have indicated the coherence length as the diameter of the red circles, which are assumed to be larger than the characteristic structures, assumed to be worm domains as shown in the inset. In general, the internal sample structure may correspond to regions of different electron density as in a polymer or areas of different magnetic orientations, i.e., domains, in magnetic materials. The SAXS pattern corresponds to the incoherent superposition of the coherent patterns from different sample regions of the size of the red circles. Owing to the different structural or orientational units in the different sample regions the scattering pattern is somewhat smeared out. For a sample with an average characteristic size d associated with the nanoregions, the scattering pattern consists of a ring-like intensity pattern as shown in Fig. 10.18, located at a momentum transfer $Q = 2\pi/d$.

By moving the sample away from the source, as shown in the bottom half of Fig. 10.18, one reduces the angular opening angle of the beam intercepted by the sample, and therefore the effective path length difference of the used X-rays. This increases the coherent fraction. The associated loss of intensity can be tolerated for modern high-brightness undulator X-ray sources. One may therefore coherently illuminate a sample that has a lateral size of the order of 50 µm. Then the scattered waves from all regions of the sample can interfere and the scattered intensity distribution, the "speckle pattern," recorded by an imaging detector contains the complete information on the real space structure of the sample.[5] The remaining challenge is to invert the reciprocal space pattern into a real space structure.

To obtain a real space image of the sample from the speckle pattern the phases of the scattering amplitudes have to be reconstructed. This is typically attempted by phase retrieval algorithms that rely on oversampling of the speckle pattern [474–477]. The development of such phase retrieval methods remains an active area of research.

[5] The SAXS pattern is an averaged speckle pattern. It contains only statistical information about the sample structure but offers the advantage of higher intensity.

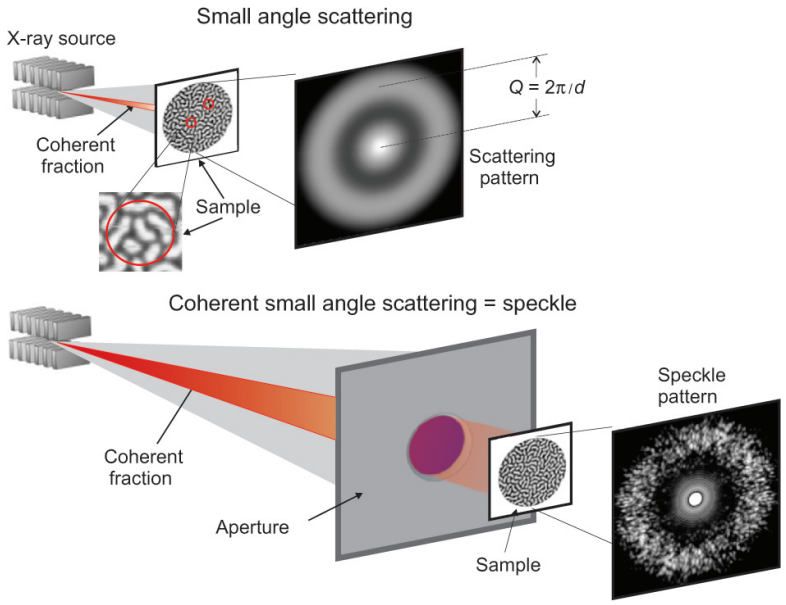

Fig. 10.18. Concepts of X-ray scattering from a sample containing worm domains of nanoscale dimensions. We have assumed a pseudomonochromatic undulator source and record the scattering pattern from the sample with a position sensitive detector. *Top*: The sample is located close to the undulator source and the beam on the sample is coherent (by geometry) only over areas that are of the size of the red circles. These coherently illuminated areas are assumed to be slightly larger than the average separation between the worm domains. The scattering pattern is the incoherent superposition of the coherent patterns from different sample regions of the size of the red circles. *Bottom*: The sample has been moved away from the source so that only a small fraction of the beam, which is coherent by geometry, illuminates the sample. At a great loss in intensity the entire sample is now coherently illuminated and the scattering pattern is a coherent superposition from all regions of the sample. The resulting scattering pattern, called a speckle pattern because of its appearance, now encodes the real space structure of the entire sample

A more robust approach is the real space image reconstruction afforded by holographic methods [478, 479]. One such method is Fourier transform holography [480], which has been successfully used to image magnetic domains with soft X-rays [481], as illustrated in Fig. 10.19.

The key component of the experiment is the introduction of a Au mask before the sample, shown enlarged in the lower left part of the figure. The Au mask contains two holes, a "sample hole" of 1.5 μm through which the sample is illuminated, and a "reference hole" of 100 nm diameters, which is drilled all

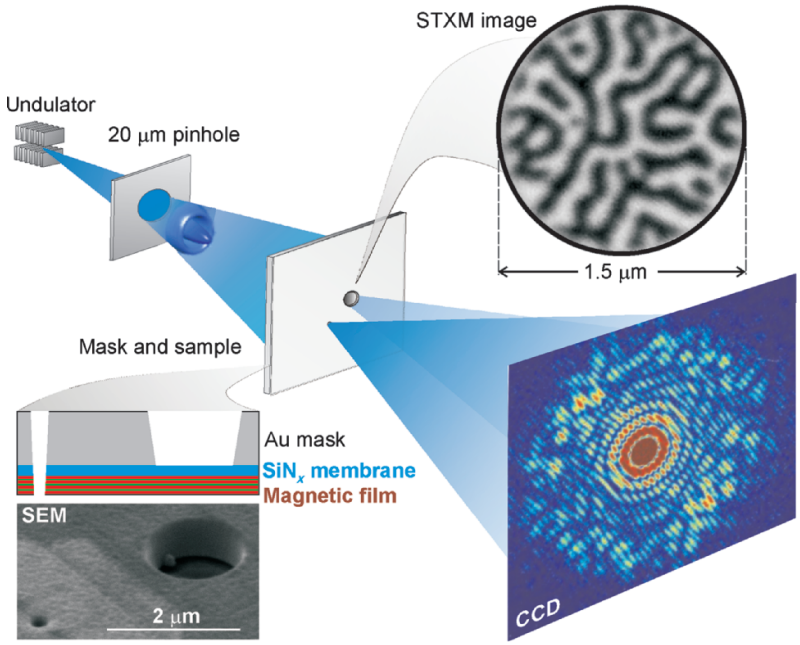

Fig. 10.19. Illustration of an X-ray Fourier transform holography experiment [481]. The X-ray beam from an undulator source with variable polarization is incident on a pinhole that redefines the source. The central part of the Fraunhofer pattern of the pinhole then illuminates a mask that consists of a "sample hole" and a "reference hole." The scanning electron microscopy (SEM) image on the *lower left* shows a close-up of the two holes which were drilled into a Au film by a focused ion beam. In the shown case the mask and sample are integrated, as shown above the SEM image. The magnetic domain structure within the pinhole opening, recorded by a scanning transmission X-ray microscope (STXM) is shown on the *right top*. The experimentally recorded hologram of the sample by a CCD detector is shown in false color on the *lower right*. For magnetic imaging one uses the resonant magnetic dichroism effect near an absorption edge, as illustrated for Fe in Fig. 9.29

the way through the mask/sample sandwich by a focused ion beam (FIB).In the experiment shown, the sample consists of a Co/Pt multilayer film with perpendicular anisotropy which exhibits a magnetic worm domain pattern, revealed in the real space XMCD STXM image on the top right. The two holes are coherently illuminated by circularly polarized photons, tuned to the Co L edge (780 eV) for optimum magnetic contrast. The beam through the larger

hole is scattered by the magnetic domains of the sample and interferes on the detector with the beam transmitted through the reference hole. The scattering pattern seen on the detector screen contains speckles like the image in Fig. 10.18 and also fine diagonal stripes which originate from the interference of the beams through the sample and the reference holes. One may think of the scattering pattern as a speckle pattern that has been phase encoded with the reference beam. The real space image of the magnetic domain structure is simply obtained by a single Fourier transformation of the recorded scattering intensities [481]. Its resolution is determined by the encoding reference beam and is therefore limited to the size of the reference hole. The reconstructed image looks identical to the STXM image shown in the top right corner of Fig. 10.18 [481].

In principle, coherent scattering experiments can be performed by means of either nonresonant X-rays or by tuning the photon energy to an absorption edge of the sample. For magnetic systems the contrast is greatly enhanced by using resonant X-rays, that is, taking advantage of the large dichroic effects near an absorption edge, as illustrated in Fig. 9.29 for Fe. In scattering experiments one may use the dichroic effect in either the real ($F'(E)$) or imaginary ($F''(E)$) part of the scattering factor as shown in Fig. 9.5. In certain cases it is advantageous to tune to the resonance in the real part $F'(E)$ which occurs below the onset of absorption, i.e., the maximum in the imaginary part $F''(E)$. For example, in experiments with intense free electron laser radiation this will greatly reduce deleterious energy transfer from the beam to the sample.

One of the unique properties of this imaging approach is that no focusing or alignment is required. While this is merely convenient for imaging at a synchrotron radiation storage ring, it is essential for the envisioned single X-ray pulse imaging with future X-ray lasers. It is important to keep in mind that lensless imaging by Fourier transform holography is a true imaging method. No iterative algorithm is required to obtain the real space structure.

The spatial resolution may be further increased by applying additional phase retrieval procedures. Since the recorded X-ray hologram can also be interpreted as a speckle pattern, one may in a second step apply an iterative algorithm to retrieve the scattering phases. This is aided by the fact that iterative phase retrieval algorithms are more effective the closer the initial input is to the real space structure [476]. One can therefore employ a two step analysis. In the first step the Fourier transform provides a resolution that is of the order of the reference hole. In the second analysis step, iterative phase retrieval algorithms are used to obtain higher resolution. The resolution in the second step is typically determined by the angular range (maximum momentum transfer) and signal-to-noise ratio of the measured scattered intensities, and is ultimately limited by the wavelength, which is about 1.5 nm at the transition metal L-edges.

10.4.3 Overview of Magnetic Imaging Results

Images of Ferromagnetic and Antiferromagnetic Thin Films

We start our discussion of X-ray magnetic imaging by presenting in Fig. 10.20 details about the typical image contrast utilized in imaging of ferromagnetic domains.

The figure shows PEEM images of ferromagnetic domains for a thin film of Co deposited on a cleaved crystal of NiO. We shall see later that the Co FM domain structure has the characteristic striped pattern of the AFM domains in the NiO crystal underneath. There are four Co domains consisting of two

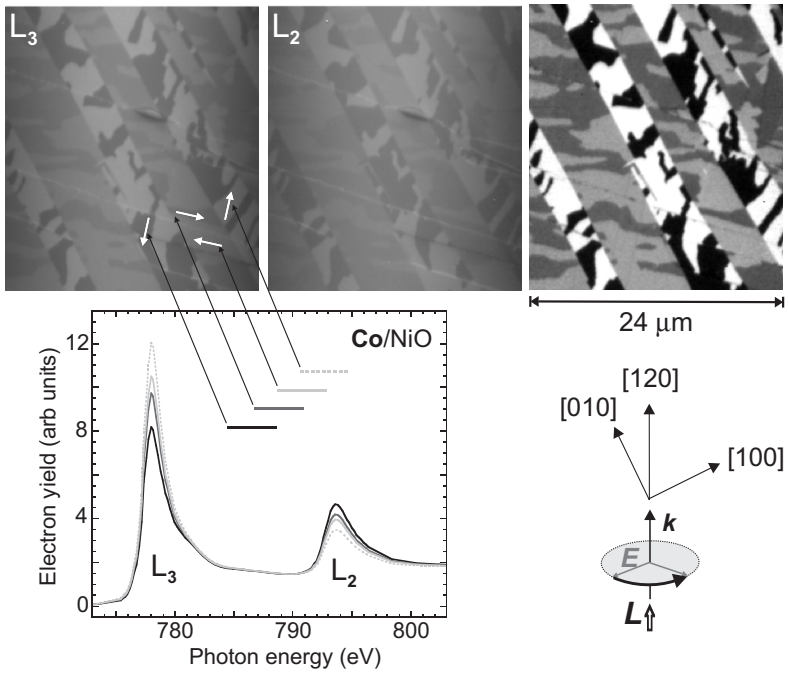

Fig. 10.20. PEEM images of the magnetic domains in a Co film deposited on single crystal NiO recorded with circularly polarized light of fixed photon spin and with the energy tuned to the L_3-edge (*left top*) and the L_2 edge (*middle top*). The XMCD spectra recorded for different domains whose orientation is indicated in the *left image* are shown underneath. The spectra are shown in different *gray shades* and the *arrows* indicate the correspondence to the domains. On the *right top* we show an image that was obtained by dividing the two images taken at the L_3 and L_2 edges. The orientation of the NiO crystal and the photon polarization is indicated on the *right bottom*

pairs of orthogonal domains, all with their magnetization in the plane of the film, as indicated by arrows in the left image. Of interest here is not the domain structure itself but how it is revealed in original images recorded with a *given circular polarization* and with the photon energy tuned to either the L_3 or L_2 edges. For this reason we show the raw images recorded at these energies and underneath the original dichroic spectra recorded from the four individual domains. This is accomplished by selecting areas on the sample by a soft-ware-set window and recording the intensity of the pixels in the window as a function of energy.

The figure illustrates the correspondence of the gray scale image contrast to the difference in spectral intensities, indicated by the shading of the spectra and by arrows. In direct analogy to the spectra the image contrast inverts at the L_3 or L_2 resonance energies, and this can be conveniently used to enhance the contrast (without change in X-ray polarization) by dividing the raw images obtained at the two edges. Another method would be to change the circular polarization at a given resonance energy. This is typically not done for microscopes located on bending magnet beam lines because by selecting radiation below and above the orbit plane (see Fig. 4.14) by movement of an aperture one changes the optical path through the beam line and this results in energy shifts. For undulator beam lines the change of polarization is straightforward and one may conveniently use opposite circular polarizations for contrast enhancement.

An example of the unique capabilities of X-rays for imaging ferromagnetic domains is given in Fig. 10.21. The figure shows FM domains in a thin film of magnetite, Fe_3O_4, grown on $SrTiO_3(110)$. As shown in the upper right of the figure, the Fe L-edge spectrum has a characteristic multiplet structure which leads to a complicated XMCD difference spectrum shown underneath. The spectra were recorded independently on an undulator beam line by fixing the circular polarization and saturating the sample into opposite magnetization states. The rich XMCD structure is a consequence of multiplet effects as well as the different Fe sites in magnetite [302] (see Fig. 7.30). The integrated negative and positive XMCD contributions at the L_3-edge have a ratio of about 2 to 1. Antronov et al. have attributed this intensity distribution with the moments on the three different Fe sites in Fig. 7.30, which also have a 2 to 1 spin-up to spin-down ratio. The XMCD domain image shown on the top left was recorded at the Fe L-edge by division of two images taken at energies with opposite dichroism effect.

The tunablility of X-rays also allows one to look for a magnetic effect at the site of the O atoms in magnetite. The dichroic O K-edge spectra and the XMCD difference are shown on the lower right of the figure. The O K-edge dichroism effect is about 2% of that at the Fe L-edge and has a characteristic XMCD structure with a negative intensity that is about a factor of 2 larger than the positive intensity, similar to the ratio seen at the Fe L-edge. As for this case, it is tempting to correlate the 2 to 1 intensity distribution with the moments on the three different Fe sites in Fig. 7.30. However, since

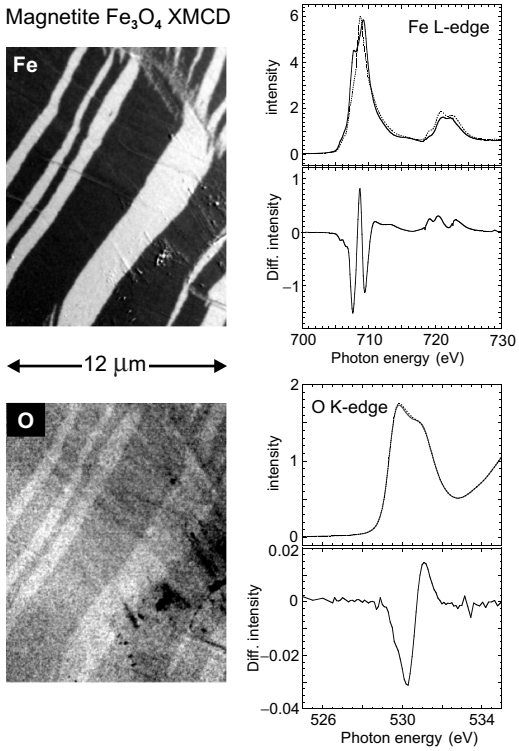

Fig. 10.21. Domain images and XMCD spectra for epitaxially grown magnetite, Fe_3O_4. On the *right* we show spectra recorded at the Fe L-edge and O K-edge with circular polarized light and magnetically saturated samples and their difference, the XMCD spectra. The O K-edge spectrum agrees with that shown in Fig. 7.32a. The images on the *left* were obtained by dividing two images recorded at two photon energies with opposite dichroism effects

all O atoms in Fe_3O_4 are equivalent, the situation is different, since the O K-shell transitions must reflect different valence orbitals on the same atom. The negative O K-edge XMCD peak would then correspond to transitions to O 2*p* orbitals involved in the bonding with Fe3*d* orbitals on the two *octahedral* Fe^{2+} and Fe^{3+} atoms, with moments coupled parallel by *double exchange*. The positive peak would correspond to O2*p* orbitals hybridized with Fe3*d* orbitals on the *tetrahedral* Fe^{3+} atoms. These Fe atoms have opposite moment orientations than the octahedral Fe atoms because of *superexchange*. We therefore have the interesting case where we can resolve the 2*p*-orbital-specific magnetic moments on the *same* O atom.

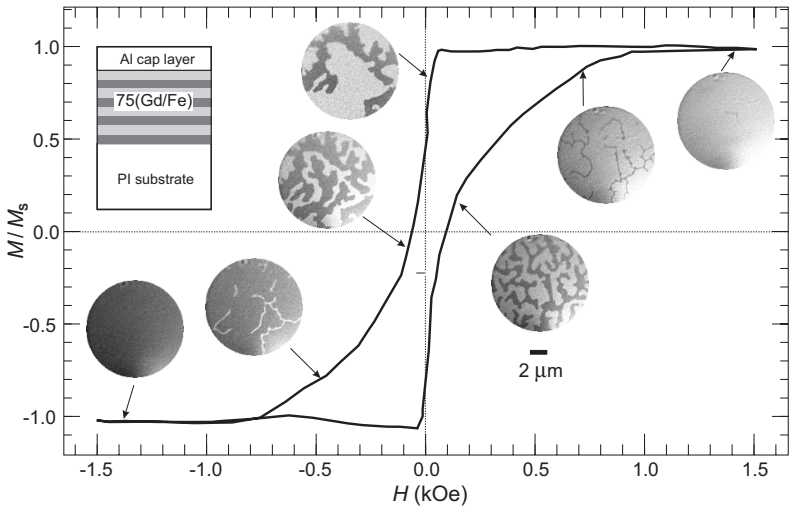

Fig. 10.22. TIXM images recorded at the FeL_3-edge as a function of applied field for a 75 × [Fe(4.1 Å)/Gd(4.5 Å)] multilayer deposited on polyimide and capped for protection with an Al layer [463, 482]

Within each magnetic domain, the dichroism spectrum has the same intensity distribution, and one can therefore use the positive and negative peaks for enhancement of the dichroic image contrast. Doing so yields the magnetic image shown in the lower left corner of Fig. 10.21. We see that it closely resembles the FM image taken at the Fe L-edge.

Our next example, shown in Fig. 10.22, demonstrates the ability of photon-in/photon out techniques to record magnetic images in the presence of a magnetic field [463, 482].

Shown here are TIXM images recorded at the FeL_3-edge for a Fe/Gd multilayer with perpendicular magnetic anisotropy at various points around the magnetization loop. The magnetic structure corresponds to domains with opposite magnetization directions along the surface normal.

As another interesting example, we show in Fig. 10.23 various images of a polycrystalline film of NiO. The 400-nm-thick polycrystalline NiO sample was deposited by sputter deposition onto oxidized Si and then annealed for 1 h at 1,100 °C in flowing oxygen at atmospheric pressure, followed by 1 h at 700 °C, and a gradual (4 h) cooldown to room temperature in flowing O_2. The procedure was applied to increase the crystallographic grain size of the film. In Fig. 10.23a we show an atomic force microscopy image of the surface after annealing, revealing an average grain size of about 180 nm, which was significantly larger than the 15–20 nm size before the annealing procedure. Inspection of the film under an optical microscope revealed that the film had

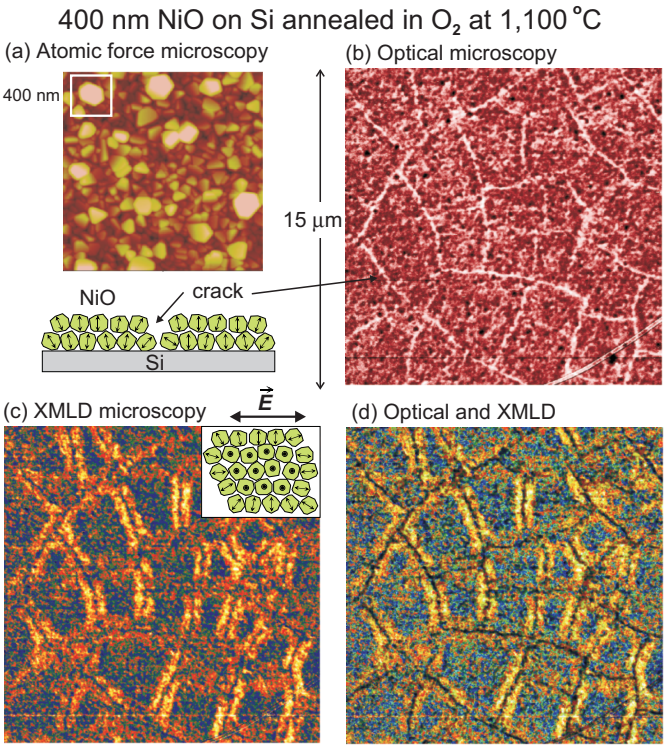

Fig. 10.23. Structure of a 400 nm thick NiO film sputter deposited on an oxidized Si substrate and annealed in an oxygen atmosphere to increase the grain size. (**a**) Atomic force microscopy image revealing the grain size, which increased from about 15–20 nm before to about 180 nm after annealing [284]. The schematic underneath illustrates that after annealing the film cracked as revealed by optical microscopy images shown in (**b**). (**c**) XMLD images obtained from difference images recorded with linearly polarized X-rays for the shown horizontal $\boldsymbol{E}$ orientation. We used two images recorded on the two L_2 multiplet peaks with opposite XMLD effects, as shown in Fig. 9.27 (also see Fig. 10.25). (**d**) Direct comparison of the optical image in (**b**) with the cracks shown in dark, superimposed on the XMLD image in (**c**)

cracked during the procedure, revealed by the web-like white crack lines in the topographical image in (b). The structure of the film deduced from these results is schematically illustrated at the bottom of Fig. 10.23a.

The sample was also studied by XMLD PEEM microscopy to investigate the antiferromagnetic domain structure. By use of linearly polarized light, images were recorded on the two L_2 NiO peaks shown in Fig. 9.27 (also see

Fig. 10.25) and divided for contrast enhancement. The resulting XMLD image in Fig. 10.23c consists of bright double lines which are predominantly oriented vertically. The widths of the bright lines are rather uniform and correspond to the grain size of the film. Direct comparison of the optical image in (b) with the XMLD image in (c), shown in (d), reveals that the crack lines, shown in dark, and the AFM double lines, shown in yellow, can be superimposed and follow the same web-like cracking pattern. However, no significant antiferromagnetic contrast exists along the horizontal or near-horizontal web lines.

The AFM contrast arises from preferential orientation of the AFM axis relative to the $\boldsymbol{E}$-vector which for the AFM image in (c) was oriented in the horizontal direction, as indicated. Bright contrast corresponds to regions with their AFM axis oriented parallel to the $\boldsymbol{E}$-vector. Hence, the bright double stripes in Fig. 10.23c correspond to grains adjacent to the cracks which have a preferred in-plane horizontal orientation of the AFM axis. Dark contrast corresponds to an AFM axis orientation perpendicular to the electric field vector. The image can thus be explained by a preferential orientation of the AFM axis as illustrated in the inset in (c). In the grains at the cracks, the AFM is oriented in-plane, perpendicular to the cracks. Within the islands the AFM is oriented perpendicular to the surface normal.

The results in Fig. 10.23 reveal a correlation between the topographical and AFM structure. The formation of cracks proves the existence of considerable stress and resulting strain in the cooling cycle. The cracking, however, does not fully relieve all film stress and the residual strain profile is expected to be inhomogeneous across the formed islands. We attribute the different orientations of the AFM axes to a magnetostrictive effect with perpendicular strain directions in the center of the island and at the cracked edges [284]. The present case is only one example for the strong correlation between crystallographic structure and strain and the orientation of the AFM axis, as discussed in Sect. 11.3.2.

Images of Coupled Magnetic Thin Films

We now look at another strength of X-rays, the investigations of coupled magnetic layers, where the elemental specificity can be used to investigate the magnetic structure in each layer separately. As an example we take a look at the exchange coupling between a ferromagnet and antiferromagnet, and in Fig. 10.24 we show the first images obtained for such systems [107].

Figure 10.24 shows images of the FM domain structure of a thin Co layer and the AFM domain structure in $LaFeO_3$ underneath, as schematically illustrated on top of the figure. The magnetic contrast in the right image arises from AFM domains in $LaFeO_3$ with an in-plane projection of the AFM axis oriented horizontally (light) and vertically (dark). The image was obtained with linear polarization by dividing two images recorded on the two L_2 peaks in Fig. 10.1c with opposite XMLD effects. The FM Co image shown on the left exhibits three distinct grey scales, corresponding to FM domains aligned

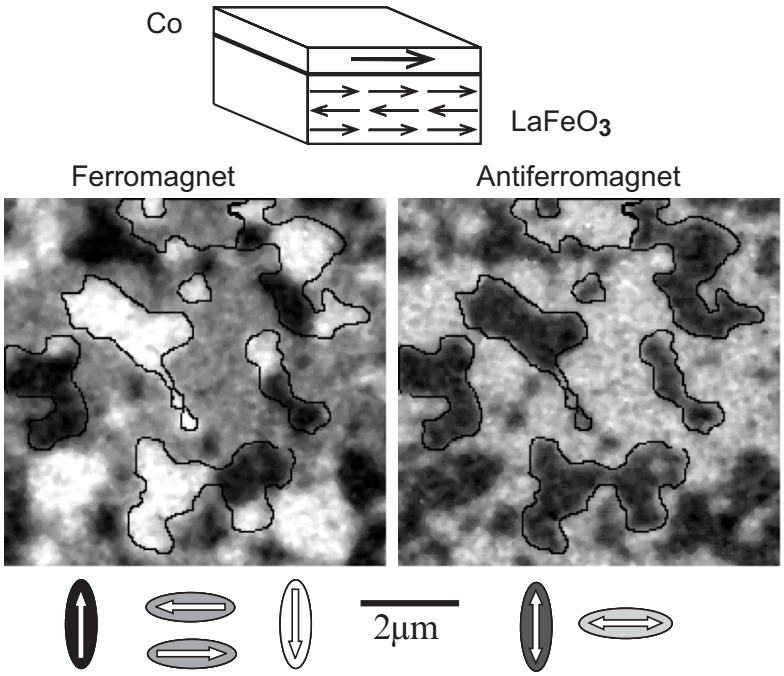

Fig. 10.24. Sample structure and PEEM images of domains in the antiferromagnetic and ferromagnetic layers for 1.2 nm Co on $LaFeO_3/SrTiO_3(001)$ [107]. *Left*: Co L-edge XMCD image of ferromagnetic domains. *Right*: Fe L-edge XMLD image of antiferromagnetic domains. The in-plane orientations of the antiferromagnetic axis and ferromagnetic spins are indicated by arrows below the images

vertically up (black) and down (white), and horizontally left or right (gray). For the experimental geometry used for the figure, corresponding to a vertical photon wave vector (angular momentum) direction, we cannot distinguish left from right horizontally oriented FM domains.

Comparison of the in-plane projections of the AFM axis and the FM spin directions, illustrated below the images, reveals that the FM Co spins are aligned parallel or antiparallel to the in-plane projection of the AFM axis. The magnetic alignment of the Co domains, which exhibit an in-plane easy axis, must therefore be caused by a coupling to uncompensated spins at the $LaFeO_3$ surface with an in-plane component parallel to the in-plane projection of the AFM axis.

Another example of FM–AFM exchange coupling is shown in Fig. 10.25. The right column of the figure shows the AFM domain pattern near the Ni(001) surface and the left column the FM domain patterns of eight mono-

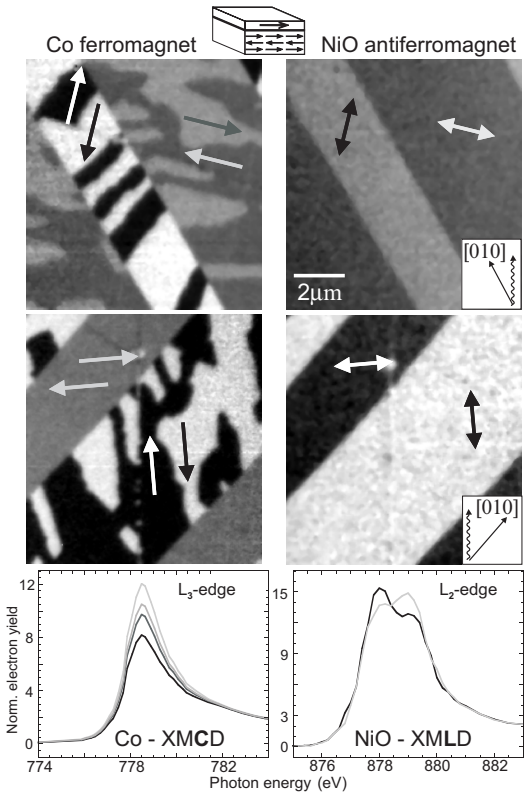

Fig. 10.25. Comparison of AFM (*right column*) and FM (*left column*) domain patterns for eight monolayers of Co on NiO(001) and two different azimuthal geometries, recorded by PEEM [404]. *Arrows* and *wavy lines* in the insets indicate the directions of the crystallographic axes and photon wave vectors, respectively. The directions of the magnetic moments in the domains are indicated by arrows. The AFM contrast in NiO was obtained by division of two XMLD images obtained with horizontally polarized light and photon energies corresponding to the two L_2-edge peaks shown in the spectrum on the bottom right. The FM image for Co was obtained by division of XMCD images recorded at the L_3 and L_2 energies. The magnetization direction of the Co film is found to be either parallel or antiparallel to the domains in the AFM, depending on which of the two AFM sublattices are present at the interface to Co. The spectra shown at the *bottom* show the XMCD and XMLD effects responsible for the contrast of the images

layers of Co deposited on top. The top and bottom rows correspond to 45° rotated azimuthal orientations, as indicated in the insets by the orientation of the photon wave vector (wavy lines) and the crystallographic axes. The

ferromagnetic domains in the Co layer split up into two subgroups with each subgroup spatially following the AFM domains. The observed spatial alignment of AFM and FM domains is caused by exchange coupling and it breaks up upon heating the system above the Néel temperature of NiO. The dichroism contrast of the other subgroup of ferromagnetic domains (black and white in lower left image) is about 30%, while the antiferromagnetic contrast in the lower right image is 14%. Within the near-interface region of NiO the AFM spin directions are found to be completely in plane, parallel to [±110] and parallel to those in Co [404].